UNIVERSITY OF CALIFORNIA
Los Angeles

Coherent Manipulation of Semiconductor Quantum Dot Qubits

A dissertation submitted in partial satisfaction
of the requirements for the degree
Doctor of Philosophy in Physics

by

John Dean Rooney

2023

ABSTRACT OF THE DISSERTATION

Coherent Manipulation of Semiconductor Quantum Dot Qubits

by

John Dean Rooney
Doctor of Philosophy in Physics
University of California, Los Angeles, 2023
Professor Hong-Wen Jiang, Chair

Quantum computing has received growing interest not only from the research community, but also in the general public. One reason for this focus is due to the ability of a quantum computer to solve problems that cannot be computed classically, creating a pathway for solutions to complex problems that would benefit numerous aspects of society. One of the popular proposals for a quantum computer harnesses semiconductor quantum dots to define qubits within electron or hole states. Due to the compatibility of this technology with existing nanoscale industrial fabrication facilities, it has a unique advantage of being able to scale to the millions of qubits required for a commercially practical quantum computer.

Within this work, I will describe two approaches to building a qubit using semiconductor quantum dots. One exploits the valley degree of freedom of conduction electrons in silicon. While these valley states are usually seen as obstacles to spin encoding schemes, we demonstrate the ability to encode a qubit within them. This valley qubit comes with the advantage of sub-nanosecond operation times and protection from charge noise during operation. We further characterize this qubit using quantum process tomography to find fidelities ranging from $79\% - 93\%$.

The second approach leverages the spin states of holes in a germanium double quantum dot. This area of research has grown rapidly over the past few years, partially because the strong spin-orbit coupling and site-dependent g-tensors of these holes allows

for all-electrical control of the qubit states without the need for micromagnets. I will characterize the evolution between singlet and triplet states and describe how the hole g-tensors can be modified, which are vital to qubit manipulation. By adjusting the voltage applied to the barrier separating the two quantum dots, we have found a g-factor that can be increased by approximately an order of magnitude, revealing a sensitivity and tunability these g-tensors have to the the local electrostatic environment.

The dissertation of John Dean Rooney is approved.

Karoly Holczer

Ni Ni

Stuart Brown

Hong-Wen Jiang, Committee Chair

University of California, Los Angeles

2023

To my mother and father . . .

who—among so many other things—

instilled in me the motivation

to pursue my curiosity

Table of Contents

1 Introduction **1**

1.1 Introduction to quantum computing 1

1.2 Quantum computing gate operations 3

1.3 Dephasing and relaxation in qubits 5

1.4 Leveraging semiconductor quantum dots for quantum computation . . . 7

1.5 Different approaches for qubit encodings within semiconductor quantum dots 11

1.5.1 Charge qubits 11

1.5.2 Singlet-triplet qubits 13

1.5.3 Hybrid qubits 16

2 The valley states of silicon **18**

2.1 Silicon band structure 18

2.2 Valley states 20

2.2.1 Valley states in bulk silicon 20

2.2.2 Lifting the degeneracy of valley states 20

2.2.3 Effects of interface disorder 23

2.3 Description of valley states within a double quantum dot 24

2.3.1 Interdot tunneling between valley states 25

2.3.2 Hamiltonian for valley states in a double quantum dot 25

3 The spin states of holes in germanium 28

3.1 Germanium band structure 28

3.1.1 Holes 29

3.2 Lifting the HH-LH degeneracy 31

3.3 Luttinger-Kohn model of the valence band 33

3.4 Including the Zeeman interaction 35

3.5 Strain 38

3.5.1 Including strain into the Luttinger-Kohn model 38

3.5.2 Strain generated from gate electrodes 40

3.6 Modeling holes in a double quantum dot 42

3.6.1 The two-site Hubbard model 42

3.6.2 Including Zeeman and spin-orbit interactions 44

3.6.3 $S - T_-$ subspace 47

4 Device Fabrication and Experimental Setup 49

4.1 Fabrication 49

4.1.1 Germanium wafer structure and characterization 50

4.1.2 Silicon wafer structure and characterization 51

4.1.3 Global alignment markers 52

4.1.4 Ohmic regions 53

4.1.5 Outer gates 53

4.1.6 Inner gates 54

4.1.7 Atomic layer deposition 55

4.1.8 Top gate 55

4.1.9 Etched contact windows . . . 55
4.1.10 Mounting and electrical contacts . . . 56
4.2 Cryogenic setup . . . 56
4.2.1 Device screening at 4 K . . . 57
4.2.2 Oxford Triton-200 dry dilution refrigerator . . . 58
4.2.3 Sample holder . . . 59
4.2.4 Electron temperature . . . 61
4.3 Electrical control . . . 61
4.3.1 Current measurements . . . 61
4.3.2 DC biases . . . 62
4.3.3 Arbitrary voltage waveforms . . . 63
4.3.4 Fast gate pulses . . . 63

5 Two-axis quantum control of a fast valley qubit in silicon . . . 65
5.1 Few electron regime . . . 66
5.2 Operation mechanism . . . 67
5.3 Readout mechanism . . . 69
5.4 Coherent valley oscillations . . . 69
5.5 Ramsey spectroscopy . . . 70
5.6 Two-axis control . . . 72
5.6.1 Control pulse . . . 72
5.6.2 Mapping the Bloch sphere . . . 73
5.6.3 Simulation of the two-axis control . . . 76
5.7 Benchmarking qubit performance . . . 77
5.7.1 Quantum state tomography . . . 78

5.7.2 Quantum process tomography . . . 80
5.7.3 Valley qubit fidelities . . . 82
5.8 Principle sources of error . . . 84
5.9 Conclusion . . . 86

6 Gate modulation of the hole singlet-triplet qubit frequency in germanium . . . 87
6.1 The few-hole regime . . . 88
6.2 Observation of coherent spin oscillations . . . 89
6.2.1 Readout mechanism . . . 91
6.2.2 Singlet-triplet splitting in (0,2) . . . 91
6.2.3 The $S - T_-$ Hamiltonian . . . 92
6.3 Dephasing and relaxation measurements . . . 93
6.3.1 T_2^* dephasing time . . . 94
6.3.2 T_1 relaxation time . . . 96
6.4 Gate modulation of the singlet-triplet frequency . . . 96
6.5 Conclusion . . . 101
6.6 Supplementary Material . . . 101
6.6.1 Simulating singlet-triplet oscillations . . . 101
6.6.2 Lever arm measurement . . . 104
6.6.3 Fast $S - T_-$ oscillations . . . 105
6.6.4 Estimation of Δ_{HL} from dot positions . . . 106

7 Future Directions . . . 108
7.1 Coupled valley qubits in silicon . . . 108
7.2 Magnetic field spectroscopy of the singlet-triplet states in germanium . . . 109

7.3 Two-axis control and characterization of the $S - T_-$ qubit 110

7.4 Conclusion 111

A Fabrication Recipe 113

References 119

List of Figures

1.1 Bloch spheres . . . 3
1.2 Dephasing and relaxation examples . . . 6
1.3 Quantum dot confinement . . . 8
1.4 Charge qubit diagrams . . . 13
1.5 Singlet-triplet diagrams . . . 15
1.6 Hybrid qubit diagrams . . . 17

2.1 Silicon band structure . . . 19
2.2 Valley splitting in silicon . . . 23
2.3 Valley state dispersion . . . 27

3.1 Germanium band structure . . . 32
3.2 Strained crystal lattice . . . 39
3.3 Metal electrode strain . . . 41
3.4 Singlet-triplet eigenergies . . . 46

4.1 Wafers and Hall bar measurements . . . 52
4.2 Beginning fabrication steps . . . 54
4.3 Final fabrication steps . . . 57
4.4 Triton dilution refrigerator . . . 59

4.5 Device carriers 60

5.1 Device structure and coherent valley oscillations 67
5.2 Ramsey spectroscopy of the (1,1)-(2,0) transition 72
5.3 Two-axis control pulse 74
5.4 Quantum control of the valley qubit 77
5.5 State tomography of Z rotations 80
5.6 Quantum process tomography for valley (Z) rotations 83
5.7 Rotation errors impact on the valley qubit 85

6.1 Ge device and the few-hole regime 89
6.2 Pauli spin blockade window 92
6.3 Coherent oscillations between spin states 94
6.4 T_2^* linecuts 95
6.5 Dephasing and relaxation measurements 97
6.6 Evolution of $S - T_-$ oscillations 98
6.7 $S - T_-$ frequencies vs. barrier voltage 100
6.8 Singlet-triplet simulation 103
6.9 Lever arm measurements 104
6.10 Fast singlet-triplet oscillations 105
6.11 Estimation of QD positions 107

7.1 Two-axis rotations 111

ACKNOWLEDGMENTS

I would like to first thank my advisor, Hong-Wen Jiang, for his careful guidance and constant support over these past few years. From his advice and supervision, I have not only overcome the numerous obstacles a graduate student typically encounters, but have also grown from my weaknesses. This improvement alone has made the journey worth it, and I consider myself fortunate to carry the experience with me for the remainder of my life.

I must also acknowledge the plethora of assistance and enjoyment from the students I have worked alongside with in the lab. Beginning with the help of Blake Freeman and Joshua Schoenfield with fabricating devices, their success opened the door for all future devices I made. In parallel, I am forever grateful for the friendship I developed with Nick Penthorn. His mentorship was invaluable and our conversations, both professional and casual, made working in the lab and attending conferences a delight. I hope to leave a similar impression on the recent additions to our lab, Tim Wilson and Stefano Roccasecca; their company and questions have been a breadth of fresh air for the lab. Will Wang, Zhentao Luo, and Rohin Verma's dedication and help has both bolstered my own research in this thesis and encouraged me to continue striving for improvement. Finally, I would like to extend my gratitude towards Niels Thompson, whose engineering prowess has kept our lab running and kindness has extended outside the lab to my own personal endeavors.

Apart from the lab, I want to thank my friends and family for their seemingly infinite patience and support: my wife, Nicole; my closest friends, Marcus and John; my sisters and brothers; and lastly my parents.

VITA

2015	B.S., Physics, University of Florida
2015	B.A., Astronomy, University of Florida
2017	M.S., Physics, University of California, Los Angeles
2016-2017	Teaching Assistant, Physics and Astronomy Department, University of California, Los Angeles
2017-2023	Graduate Student Researcher, Physics and Astronomy Department, University of California, Los Angeles

PUBLICATIONS

Nicholas E. Penthorn, Joshua S. Schoenfield, John D. Rooney, Hong Wen Jiang. "Reduction of charge impurities in a silicon metal-oxide-semiconductor quantum dot qubit device patterned with nano-imprint lithography." *Nanotechnology*, **30**, 465302, 2019

Nicholas E. Penthorn, Joshua S. Schoenfield, John D. Rooney, Lisa F. Edge, and Hong-Wen Jiang. "Two-axis quantum control of a fast valley qubit in silicon." *npj Quantum Information*, **5**, 12, 2019

Will Wang, John D. Rooney, Hong-Wen Jiang. "Automated Characterization of a Double Quantum Dot using the Hubbard Model." *arXiv:2309.03400*, 2023

John Rooney, Zhentao Luo, Lucas E. A. Stehouwer, Giordano Scappucci, Menno Veldhorst, Hong-Wen Jiang. "Gate modulation of the hole singlet-triplet qubit frequency in

germanium." *arXiv:2311.10188*, 2023

CHAPTER 1

Introduction

1.1 Introduction to quantum computing

Our world is fundamentally quantum. If we wish to accurately simulate the Physics of Nature, then we require the ability to emulate its quantum character. As introduced by Paul Beinoff in 1980 and popularized by Richard Feynman in a 1981 keynote speech, this desire necessitates a different kind of computation than the method used by classical computers prevalent today–a quantum computation [Ben80, Fey82]. With the power of quantum computers, the pathway opens to solving complex problems in quantum cryptography, accelerated drug discovery, machine learning, and the development of revolutionary materials [Int18]. Since Beinoff and Feynman's proposals and with this motivation in mind, quantum computers have grown from the theoretical and small-scale research settings to industrial giants fabricating chips with over 400 quantum bits [CN22]. However, these computers are best described as noisy intermediate-scale quantum (NISQ) devices, as they are able to perform calculations that surpass the abilities of any classical computer but are severely limited by noise to operate reliably [Pre18]. While this technology has achieved impressive feats in recent years, such as simulating the isomerization of N_2H_2 [QCA20], it remains distant from the goal of a computer composed of millions of quantum bits that can tackle the practical problems of today. This thesis will describe my contributions to moving this technology closer to that aspiration.

The feature that distinguishes a quantum computer from its classical counterpart

and provides its advantage is the quantum bit, more commonly referred to as the qubit. While both classical and quantum bits are generated from a two-level system ($|0\rangle$ and $|1\rangle$), the nature of a quantum system allows a qubit to exist in a superposition of these states. This property becomes more apparent when we look at the general form of a two-level quantum system:

$$|\Psi\rangle = \cos\left(\frac{\theta}{2}\right)|0\rangle + e^{i\phi}\sin\left(\frac{\theta}{2}\right)|1\rangle, \tag{1.1}$$

where $\theta \in \{0, \pi\}$ corresponds to the amplitude associated with the qubit being in either the $|0\rangle$ and $|1\rangle$ state, and $\phi \in \{0, 2\pi\}$ represents the phase between these two states. For example, with $\theta = \pi/2$ and $\phi = 0$, the state of the qubit becomes a quantity that cannot be encoded into a classical bit: $|\Psi\rangle = \frac{1}{\sqrt{2}}(|0\rangle + |1\rangle)$.

However, the power of quantum computers truly manifests when multiple qubits operate together. Consider the case of two qubits, where each qubit can be in a superposition of $|0\rangle$ and $|1\rangle$. Combining these qubits creates to a superposition of all four possible outcomes:

$$|\Psi\rangle = a|00\rangle + b|10\rangle + c|01\rangle + d|11\rangle. \tag{1.2}$$

where the left (right) digit denotes the state of the first (second) qubit. This entangled state can be exploited to perform computations on the individual outcomes *simultaneously*. In contrast, two classical bits can also represent each of these outcomes ($\{|00\rangle, |10\rangle, |01\rangle, |11\rangle\}$) but only one at a time, meaning a classical computer would need to perform four separate operations to match the quantum computer's one. This quantum speedup grows exponentially with the number of qubits (2^N), granting quantum computers the ability to efficiently solve specific complex problems where a large number of possible outcomes exist [Fey82, DiV95, EJ96, Sho97, NC10, CD10, Mon16, Jor].

1.2 Quantum computing gate operations

To better visualize these qubit operations, it is beneficial to map the state of the qubit in Eqn. 1.1 onto what is known as the Bloch sphere, where the coordinates of the state vector are defined by θ and ϕ. In this representation, the north ($\theta = 0$) and south ($\theta = \pi$) pole of the sphere symbolize the $|0\rangle$ and $|1\rangle$ states respectively. For example, Fig. 1.1a illustrates the specific state where $\theta = \pi/4$ and $\phi = 3\pi/4$. From Eqn. 1.1, one can see that any state that does not lie along the z-axis is a mixture of the two logical states, where the maximally mixed states are located along the equator.

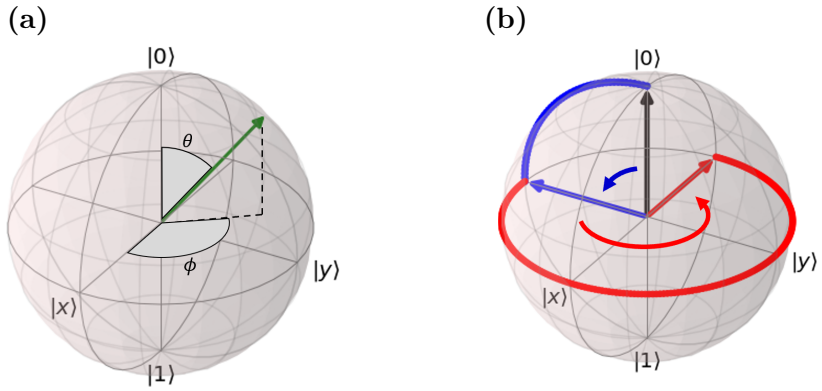

Figure 1.1: **(a)** Visualization of a qubit's state on the Bloch sphere. This particular state is defined with $\theta = \pi/4$ and $\phi = 3\pi/4$ according to Eqn. 1.1. The north and south pole of the Bloch sphere correspond to $|0\rangle$ and $|1\rangle$ respectively. Points along the equator represent equal superpositions of $|0\rangle$ and $|1\rangle$, where $|x\rangle = \frac{|0\rangle+|1\rangle}{\sqrt{2}}$ and $|y\rangle = \frac{|0\rangle+i|1\rangle}{\sqrt{2}}$. **(b)** A qubit is initialized in the state $|0\rangle$ (black arrow). An X($\pi/2$) rotation transforms this state to $|-y\rangle$ (blue arrow). Finally a Z($3\pi/2$) rotation brings this state to $|-x\rangle$ (red arrow).

With this tool in hand, we can begin to explore important operations applied to single qubits. For example, a basic requirement for controlling a qubit is the ability to move the qubit state to any point on the Bloch sphere. This manipulation is usually accomplished through establishing two rotation axes of control, where one qubit operation rotates the state around the x axis changing θ, while another results in Z rotations changing ϕ.

For example, Fig. 1.1b illustrates two operations on the initial state $|0\rangle$: The first is an X($\pi/2$) rotation that moves the the state to the equator ($|-y\rangle$). The second is a Z($3\pi/2$) operation that rotates $|-y\rangle$ around the z axis to $|-x\rangle$. As another example, a NOT gate would be a X(π) rotation, where $|0\rangle$ would flip to $|1\rangle$ and vice versa.

Once this control over the qubit has been established, the next milestone for quantum computation is entangling two qubits together. We define an entangled state as one where the state of a qubit cannot be described independently of its entangled partner's state [Per10]. One of the most straightforward ways to generate an entangled state is through what are known as controlled two-qubit gates. These gates are act on a pair of qubits, where the operation on one qubit is only performed if its partner is in a specific state.

As a concrete example, let us extend the NOT gate described above to the controlled-NOT (CNOT) gate acting on two qubits, which performs a NOT operation on the second qubit only when the first qubit is in the state $|1\rangle$. Let us assume the first qubit is already rotated to the state $|\Psi_1\rangle = \frac{1}{\sqrt{2}}(|0\rangle + |1\rangle)$ and the second qubit is initialized to $|\Psi_2\rangle = |0\rangle$. The complete state of the system can then be written as

$$\begin{aligned} |\Psi_1\rangle \otimes |\Psi_2\rangle &= \frac{1}{\sqrt{2}}(|0\rangle + |1\rangle) \otimes |0\rangle \\ &= \frac{1}{\sqrt{2}}(|0\rangle \otimes |0\rangle + |1\rangle \otimes |0\rangle) \\ &= \frac{1}{\sqrt{2}}(|00\rangle + |10\rangle). \end{aligned} \tag{1.3}$$

Now we apply the CNOT gate to this state:

$$\begin{aligned} \text{CNOT } |\Psi_1\rangle \otimes |\Psi_2\rangle &= \text{CNOT } \frac{1}{\sqrt{2}}(|00\rangle + |10\rangle) \\ &= \frac{1}{\sqrt{2}}(|00\rangle + |11\rangle), \end{aligned} \tag{1.4}$$

where the state of the target qubit (right) is only flipped when the control qubit (left) is 1. This final state happens to be one of the four Bell states, which form a basis of maximally entangled states for two qubits. As this state is entangled, it is not possible

to separate it back into a product state of two independent qubits. With the ability to perform arbitrary single qubit rotations and two-qubit entangling operations, a universal set of quantum gates are available. Universal refers to the requirement that any possible quantum gate can be reduced to a finite set of operations, and is one of the important requirements for a quantum computer [DiV00].

1.3 Dephasing and relaxation in qubits

As briefly mentioned in the opening paragraph of this thesis, state of the art quantum computers are best described as noisy intermediate-scale quantum (NISQ) devices. The term "noisy" refers to the issue that these large quantum computers cannot perform long computations without succumbing to noise [Sho96]. This deficiency is due to either a build-up of errors or the eventual decoherence of the superposition of states essential to the operation. All quantum computers strive to reach a fidelity threshold where error correction schemes can overcome this noise and generate useful computations. This goal is known as the fault-tolerant threshold and its maximum allowed error is on the order of 1% with current error mitigation techniques [FSG09].

In this section, I will introduce two important processes that contribute to the error of qubit operations, both of which result from a slight but significant coupling the environment outside the qubit subspace: dephasing and relaxation. Inhomogeneous dephasing originates from the qubit being poorly synchronized with itself or another qubit, resulting in a phase difference between successive operations [BLN21]. The longer an operation lasts, the greater the effect of this phase difference becomes. When averaging many final states that have accumulated variable amounts of phase over a long period of time from the same operation, the end result is an incoherent mixture of the $|0\rangle$ and $|1\rangle$ states (Fig. 1.2a). Fig. 1.2b illustrates the effect of dephasing on a qubit while it oscillates between its $|0\rangle$ and $|1\rangle$ states. The inhomogenous dephasing time can be extracted from the decay these oscillations clearly experience, and is defined as T_2^* in the literature. Fortunately, the effects of T_2^* can be mitigated at the cost of longer and more

complicated manipulation sequences [ZDR18].

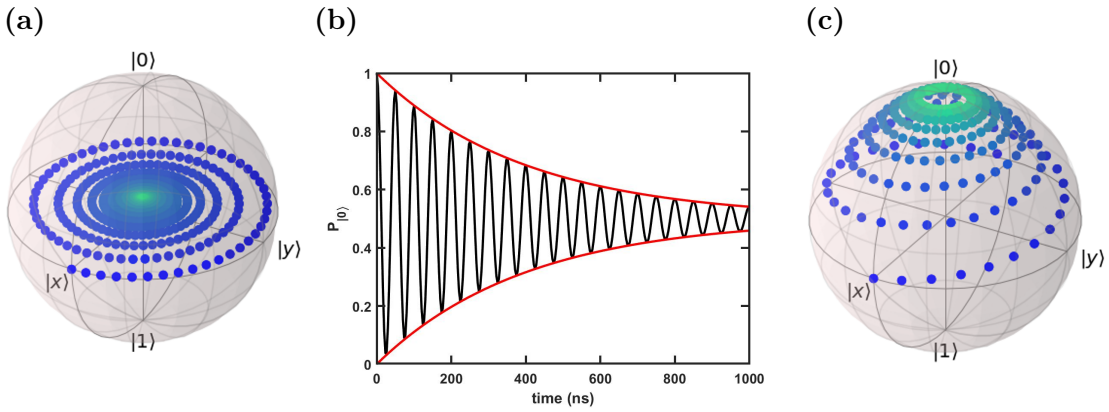

Figure 1.2: **(a)** Example of a qubit operation experiencing inhomogenous dephasing beginning at $|x\rangle$ and rotating around the Z axis. Eventually, an incoherent mixed state is reached (green dots). **(b)** With no coupling to outside environment, this qubit would oscillate between $|0\rangle$ and $|1\rangle$ indefinitely. With a dephasing time of $T_2^* = 400$ ns, these oscillations (black) quickly decay, limiting the qubit's operation time. The dephasing time defines the envelope (red) of the sinusoidal oscillations. **(c)** Example of relaxation affecting the Z rotations of a qubit beginning in the state $|x\rangle$. As time goes on (blue to green points), the excited state $|1\rangle$ relaxes to $|0\rangle$. If relaxation was absent, the state would rotate around the equator indefinitely.

Similar to dephasing, relaxation is another process that leads to the loss of quantum information. Whereas the dephasing time characterizes a phase error, relaxation entails a loss in energy for the qubit, leading to the relaxation of the excited state to the ground state [ZDM12]. Consequently, operation and readout times are also limited by the relaxation rate, defined as T_1^{-1}. Relation is typically described well in experiments by an exponential decay of the excited state down to the ground state. Fig. 1.2c demonstrates how the initial state $|x\rangle$ rotating around the z axis is affected by $|1\rangle$ relaxing to $|0\rangle$.

1.4 Leveraging semiconductor quantum dots for quantum computation

The requirements for a quantum computer are broad enough that the list of viable technologies for quantum computing continues to grow. Because no candidate has yet to advance far enough, companies, governments, and research groups also continue to pour money and effort into many of these qubit implementations. This thesis focuses on one such route towards realizing a large-scale, practical quantum computer, and that avenue is leveraging semiconductor quantum dots. In this section, I will briefly touch upon the basics of a quantum dot (QD) defined in a semiconductor heterostructure and outline why QDs are a promising candidate for advanced quantum computing.

A semiconductor heterostructure (with possible aid from a metal electrode) can generate a two-dimensional (2d) gas of charge carriers (e.g., electrons or holes) confined along the growth direction of the heterostructure (which I define as z). Voltages applied to additional electrodes fabricated on top of the heterostructure can further confine this 2d gas along the lateral direction into an island of charge with a radius of ~ 50 nm, which forms the quantum dot [ZDM12]. Fig. 1.3a shows a top-down view of a device where a 2d electron gas (2DEG) is depleted by local metal electrodes to from two QDs. Fig. 1.3b shows a side view of a Si/SiGe heterostructure, where electrons are confined to a Si quantum well sandwiched between two SiGe layers. The right of this figure illustrates how the confinement potential along the z direction creates a well within the Si layer. A voltage is applied to the global top gate to populate the welll, while local gates B_1 and B_2 deplete the 2DEG, forming an quantum dot between them.

There are two important properties that define the QD. The first originates from the Coulomb repulsion of charge already present on the QD, which prevents any additional charge from tunneling onto the dot unless this energy barrier is overcome. When cooled to millikelvin temperatures, this charging energy E_c is utilized to control the number of carriers on the dot. The second property is the confinement of the charge in all three

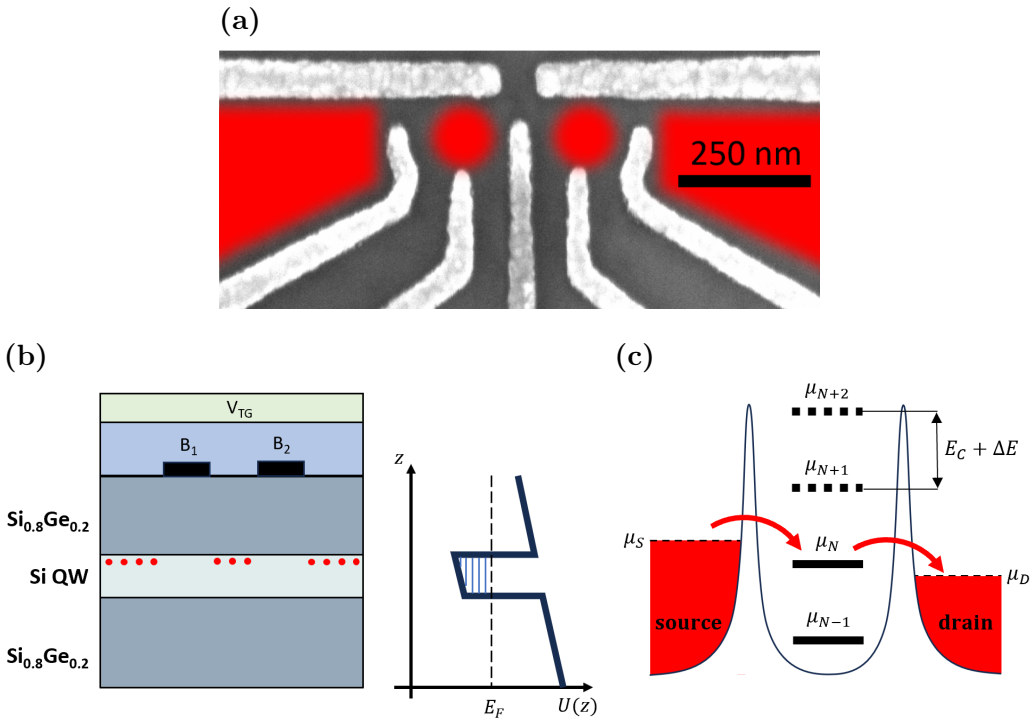

Figure 1.3: **(a)** Example of a 2d electron gas (red) confined along the x-y directions using metal electrodes fabricated above the heterostructure. Two islands of electrons are isolated. **(b)** A SiGe heterostructure depicting electrons (red dots) confined along the z direction in the quantum well. Gates B_1 and B_2 confine the electrons in the x-y plane to form a quantum dot in the center. The potential along the z direction is depicted to the right, where electron states are occupied up until the Fermi level E_F. **(c)** Diagram illustrating the chemical potential of a quantum dot. Charge can only tunnel onto the dot when its chemical potential lies below μ_S.

directions results in a discrete energy spectrum akin to atoms. With this energy spectrum and the ability to deterministically add or remove charge from the dot, it is fair to describe QDs as artificial atoms [WFE02]. The tunneling rate onto and off the dot and the number of charge carriers present is also controlled through these confinement electrodes. Fig. 1.3c demonstrates electrons can only tunnel onto the dot when its chemical potential μ_N lies below the that of the source and drain reservoirs. For an additional electron to be added to the dot, gate electrodes must lower the energy of μ_{N+1} by $E_c + \Delta E$, where ΔE accounts for the additional energy from the quantized states [WFE02, ZDM12]. In a similar manner, electrons can be removed from the dot by raising its chemical potential. When operating at millikelvin temperatures, it becomes possible to deplete the dot down to the final charge carrier.

With access to a regime where only a few electrons or holes are present on the dot, it was eventually proposed by Loss and DiVincenzo in 1998 to exploit of the spin states of these QDs for qubit manipulation [LD98]. The spin degree of freedom of an electron or hole naturally forms the two state system required for qubits. However, the physics of quantum dots, especially when multiple dots are coupled together, is rich enough that single spin states are not the only method of creating viable two-state systems for qubits. Various encodings will be introduced in the following section and a couple will be expanded upon in later chapters of this thesis.

Compared to other material platforms, semiconductor quantum dots are accompanied by the large space of tunable parameters in the solid-state environment. For example, the tunneling rate onto a dot can be easily tuned by the adjustment of one voltage. When multiple dots are fabricated alongside each other (Fig. 1.3a), the wave function overlap of the particles confined inside the QDs is sensitive to the electrode separating the QD pair. The size, shape, and proximity to other QDs can all be modified to suite the needs of the desired qubit encoding. While this is advantageous in many respects, it is followed by the downside that creating identical quantum dots is a difficult feat. For small numbers of qubits, their unique personalities can be overcome by time and effort; however, it is certainly not feasible to extend this procedure to the vast number of qubits

needed for practical quantum computers.

A second advantage that partially alleviates these concerns is the existence of an enormous semiconductor industry that has dedicated itself to the production of billions of metal electrodes on top of heterostructures with exceptionally high fidelity and density. It was through this technology that the early room-sized classical computers were scaled down to the size of our pockets. The fabrication of semiconductor quantum dots follows these same procedures, meaning the field already has access to the industrial-scale operations that would be used for large-scale computers. While these corporations have already entered the race to building a quantum computer [ZKW22], their entry has not solved every problem facing the community, and plenty of work remains to be done as larger qubit arrays are engineered and different encodings and materials are tested.

One such area of research is understanding the noise sources that govern qubit coherence. To varying degrees, the majority of qubit encodings are coupled to the electrical fluctuations in the environment. This noise can originate from unstable gate voltages, background charge fluctuators in the substrate, and phonons [HKP07, CNQ19]. In addition to this charge noise, all qubits encoded in the spins of electrons or holes suffer from magnetic noise, where the spins experience a varying magnetic field due to their hyperfine coupling to the surrounding nuclei in the substrate. One can think of the ensemble of nuclear spins generating an effective magnetic field, known as the Overhauser field. As the Overhauser field assumes a random orientation, the qubit spins will evolve accordingly in an unknown manner. Fortunately, this noise source can be heavily mitigated by using substrates whose nuclei have zero nuclear spin, such as isotropically purified ^{28}Si, or particles with weak hyperfine interactions (e.g., holes) [HKP07].

Both charge and magnetic noise directly lead to the dephasing and relaxation effects introduced in section 1.3. When exploiting spin states for qubit control, the dephasing time T_2^* is generally much shorter than the relaxation time T_1. Due to a strong dependence on the substrate and encoding technique, these T_2^* times range from several ns to tens of μs [PSR19, HFS20, XRS22, NTN22]. To increase qubit fidelities, the community has focused on either boosting qubit coherence times through improved substrates, device

design, and pulse techniques, or raising operation speeds.

Beginning in 2014, single qubit gates with fidelities exceeding the 99% fault-tolerant threshold were demonstrated in Si quantum dots [VHY14]. However, extending this accomplishment to two-qubit gates has only been recently achieved in the past two years [NTN22, XRS22, MGG22, WRJ23]. While delayed, this exciting accomplishment establishes that semiconductor quantum dots have the potential to be scaled up to practical quantum computers, as long as this success can continue as qubit arrays grow.

1.5 Different approaches for qubit encodings within semiconductor quantum dots

As I have alluded to several times already, there are numerous ways to encode a qubit using semiconductor quantum dots. In this section, I will briefly introduce three of these variants, two of which will be explored in later chapters.

1.5.1 Charge qubits

One of the simplest encodings one can make within quantum dots is utilizing the charge state of a double quantum dot (DQD). In this scheme, two quantum dots are fabricated next to each other and a single charge, such as an electron, is free to shuffle between the two dots. The logical qubit states are encoded in the left $|L\rangle \rightarrow |0\rangle$ and right $|R\rangle \rightarrow |1\rangle$ charge states of the DQD. This system can be described by the relative energy difference between the two dots, defined as the detuning ϵ, and the tunnel coupling t_c between them [GHW05]. The energy levels of each dot can be tuned by gate electrodes (typically called plungers) fabricated directly above the dots. Similarly, the tunneling barrier between the dots is adjusted through a third electrode (called a barrier) between the two plungers (see Fig 1.4a).

The Hamiltonian for this system in the basis $\{|L\rangle, |R\rangle\}$ is as follows:

$$H = \frac{\epsilon}{2}\sigma_z + \frac{t_c}{2}\sigma_x = \frac{1}{2}\begin{pmatrix} \epsilon & t_c \\ t_c & -\epsilon \end{pmatrix}, \tag{1.5}$$

where σ_x and σ_z are the Pauli matrices. Fig. 1.4b plots the eigenenergies for this H as a function of ϵ. Taking the difference between these two eigenenergies results in the frequency of the qubit rotations as a function of ϵ and t_c:

$$f = \sqrt{\epsilon^2 + t_c^2}/h. \tag{1.6}$$

For large detunings, the Hamiltonian simplifies to $H = \frac{\epsilon}{2}\sigma_z$, where the eigenstates are for the charge to be in either the left or right dot. When ϵ is large and negative (positive), the DQD potential is skewed so that finding the charge in the left (right) dot is the ground state. Fig. 1.4a illustrates the DQD for a negative detuning. Under this condition, the frequency of the qubit is $f = \epsilon/h$ and the qubit rotates around the z axis of the Bloch sphere (red arrow in Fig. 1.4c).

Directly at $\epsilon = 0$, where the energy levels of the dot are aligned, $H = \frac{tc}{2}\sigma_x$ and the eigenstates become admixtures of $|L\rangle$ and $|R\rangle$. Therefore, to perform X rotations around the Bloch sphere, one only needs to set the detuning to zero (blue arrow in Fig. 1.4c).

Although this qubit has the benefit of being simple with rotations that are completely controlled by the voltages applied to electrodes, it is highly susceptible to charge noise. Recall that charge noise leads to fluctuations in any parameters in the system that critically depend on the local electric field. Because the dot energy levels are directly tied to the field generated by the plunger gates, any charge noise present distorts the detuning ϵ. The charge qubit is protected to first order from this noise only at $\epsilon = 0$, where$E = hf = t_c$ and $\frac{\partial E}{\partial \epsilon} = 0$. However, when performing Z rotations, $E = \epsilon$, meaning the qubit frequency is directly influenced by fluctuations in ϵ from charge noise. Consequently, the coherence times for charge qubits are too short (~ 1 ns) relative to the gate

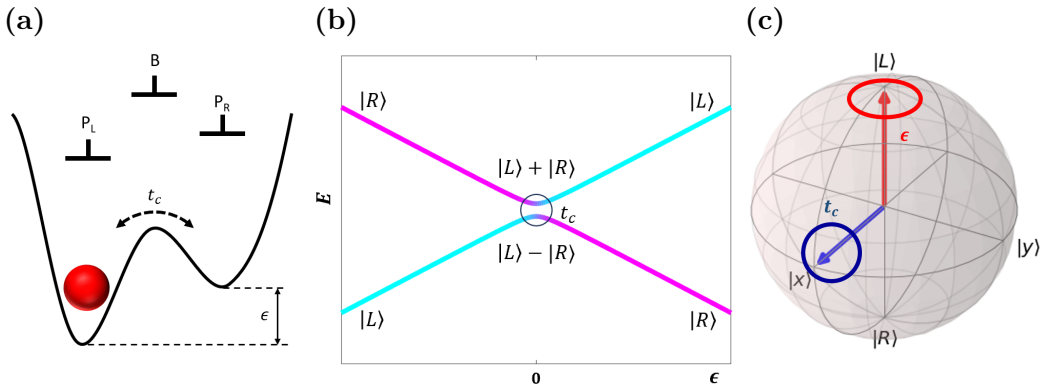

Figure 1.4: **(a)** Confinement potential along the x-y plane generated by voltages applied to the two plungers (P) and barrier (B) gates. These gates control the energy difference (ϵ) and tunnel coupling (t_c) between the two dots **(b)** Energy diagram for the charge qubit. Near $\epsilon = 0$, the eigenstates become superpositions of $|L\rangle$ and $|R\rangle$. **(c)** The evolution of the charge qubit around the Bloch sphere can be directly controlled by adjusting the detuning between the dots. Rotations around the z-axis (red) are performed with $\epsilon \gg t_c$, while X rotations (blue) occur at $\epsilon = 0$ and t_c dominates H.

operation speed (~ 0.5 ns) to achieve high fidelities for single qubit gates [HFC03].

1.5.2 Singlet-triplet qubits

In order to mitigate the effects of electrical noise, one can opt for a system whose energy levels are less sensitive to it. One such design is using the spin degree of freedom of the charge trapped in the quantum dot. In this section, I will introduce the specific case where two spin-1/2 particles are confined within the DQD, and each dot hosts one particle (Fig. 1.5a). The four possible spin states of this system are the singlet and three

triplet states [HKP07]:

$$|S\rangle = \frac{1}{\sqrt{2}}(|\uparrow\downarrow\rangle - |\downarrow\uparrow\rangle)$$
$$|T_-\rangle = |\downarrow\downarrow\rangle$$
$$|T_0\rangle = \frac{1}{\sqrt{2}}(|\uparrow\downarrow\rangle + |\downarrow\uparrow\rangle)$$
$$|T_+\rangle = |\uparrow\uparrow\rangle$$

Fig. 1.5b illustrates the energies of these spin states as a function of detuning. The energy difference between the singlet state and $|T_0\rangle$ equals the exchange term $J(\epsilon) = -\frac{\epsilon}{2} + \sqrt{\frac{\epsilon^2}{4} + 2t_c^2}$ for smaller detunings and plateaus to the difference in the two dot's Zeeman energies, ΔE_z, for large ϵ. The ϵ and t_c terms are the same as those discussed in previously in Section 1.5.1. In the presence of a magnetic field, the polarized triplet states split from $|T_0\rangle$ by the average Zeeman energy of the two dots, $\Sigma E_z/2$.

As Fig. 1.5b immediately shows, one must decide which pair of the four spins states to use as the logical basis for the qubit. The most studied subspace has been $\{|S\rangle, |T_0\rangle\}$, as these states are the most accessible for electrons in DQDs [BLP23]:

$$H_{ST_0} = J(\epsilon)\sigma_z + \frac{\mu_B \Delta(g^* B)}{2}\sigma_x \tag{1.7}$$

Here, $J(\epsilon)$ is the exchange coupling between the spin states and can be controlled with the DQD detuning ϵ. The X rotations are controlled by the difference in Zeeman energy between the two dots, where g^* is the effective g-factor and B is the magnetic field of each dot. This ΔE_z is generated from the Overhauser field, a micromagnet, or site-dependent g-factors. Typically, ΔE_z remains constant while ϵ controls the angle of rotation in the x-z plane $\theta = \arctan(\Delta E_z/J(\epsilon))$ (see Fig. 1.5c). It is worth mentioning that recent studies of holes in Ge substrates have taken advantage of its strong spin-orbit coupling and g-factor anisotropy to encode the qubit within the $S - T_-$ subspace [JMH22, BLN21]. Operating in this subspace is similar to that of $S - T_0$, and I will

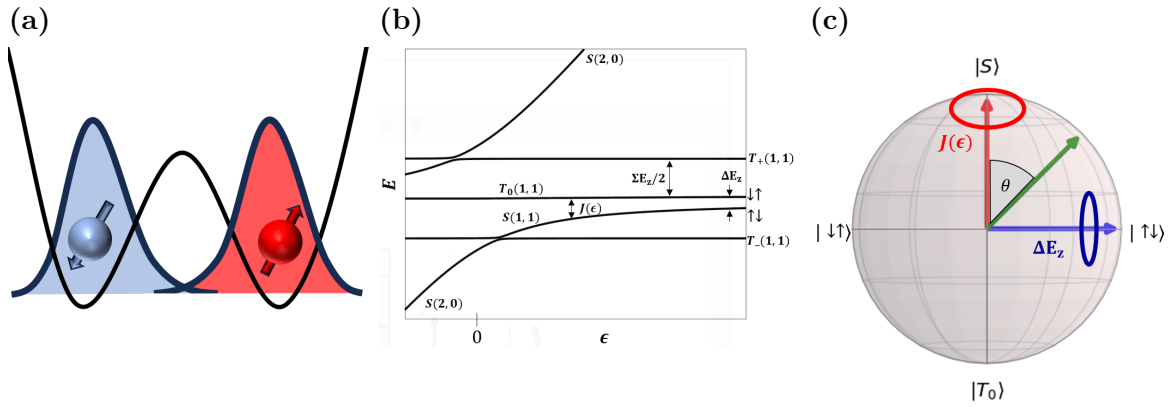

Figure 1.5: **(a)** Two spin-1/2 particles trapped in a double quantum well. The wave function overlap (blue and red) is controlled by the center gate electrode of the DQD. **(b)** Energy level diagram for the singlet and triplet states confined to a DQD. The $|\uparrow\downarrow\rangle$ and $|\downarrow\uparrow\rangle$ states denote mixtures of $|S\rangle$ and $|T_0\rangle$. **(c)** Bloch sphere depicting the two rotation axes for the $S - T_0$ qubit. The strength of $J(\epsilon)$ is controlled through the DQD detuning ϵ. For small ϵ, $J(\epsilon) \gg \Delta E_z$ and the qubit rotates around the z-axis (red). For large ϵ, $J(\epsilon) \to 0$ and X rotations are performed.

expand on this topic in detail in later chapters of this thesis.

Compared to charge qubits, singlet-triplet qubits have much longer coherence times ($T_2^* \sim 1$ μs) at the cost of slower operation speeds ($\sim 10 - 100$ MHz) [FCH18, JJH18, JHB21]. This enhancement in coherence originates from the environment needing to interact with the system's spin degree of freedom instead of only its charge. The case of harnessing two holes in a DQD for singlet-triplet encoding will be discussed in Chapters 3 and 6.

1.5.3 Hybrid qubits

A middle ground between charge and spin qubits exists where characteristics of both systems are harnessed. These so-called hybrid qubits borrow the the fast operation times of charge qubits and decoherence protection of spin qubits [KGF12, KSS14, CLY16, PSR19]. For example, one instance of this encoding utilizes the charge states $\{|R\rangle, |L\rangle\}$ of a double quantum dot along with the valley splitting $\{|L_{v1}\rangle, |L_{v2}\rangle\}$ of the ground state. The origin of this valley splitting and the conditions under which it can be utilized will be discussed in later chapters. A Hamiltonian governing the dynamics of this type of qubit in the $\{|R\rangle, |L_{v1}\rangle, |L_{v2}\rangle\}$ basis is the following:

$$H = \begin{pmatrix} \frac{\epsilon}{2} & \Delta_1 & \Delta_2 \\ \Delta_1 & -\frac{\epsilon}{2} & 0 \\ \Delta_2 & 0 & -\frac{\epsilon}{2} + E_{VS} \end{pmatrix}, \tag{1.8}$$

where Δ_1 is the coupling between the right dot charge state and the lower valley state of the left dot, Δ_2 is the right dot's coupling to the excited valley state of the left dot, and E_{VS} is the valley splitting of left dot.

The energy levels of this system are depicted in Fig. 1.6a, where the weight of the left dot's lower and excited valley states are colored red and blue respectively. Rotations around the x axis of the Bloch sphere are performed near the anticrossing of the $|L\rangle$ and $|R\rangle$ charge states (ϵ_x in Fig 1.6a). Just like in the charge qubit case, this detuning is favorable for qubit operations because it is insensitive to fluctuations in detuning (i.e., charge noise) to first order. On the other hand, Z rotations are executed in the large detuning regime (ϵ_z in Fig 1.6a). At this point, the qubit rotates around the axis defined by the valley states of the left dot. Due to the energy levels being parallel in this region, the qubit is also insensitive to charge noise resulting in longer coherence times.

Hybrid qubits exhibit dephasing times on the order of 1-10 ns with operation times $\sim$ 200 ps [KWS15, SFJ17, PSR19], making them one of the fastest qubits available. The details of encoding a qubit into the valley states of Si will be discussed in Chapters 2 and

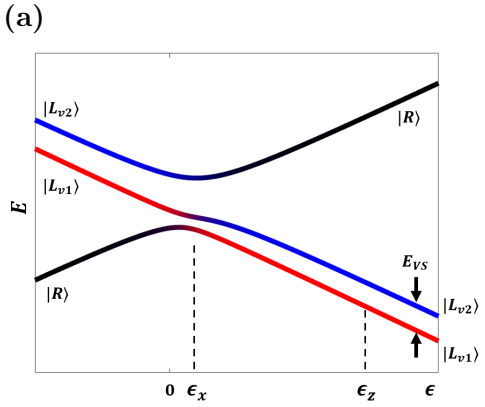

Figure 1.6: **(a)** Energy level diagram for the hybrid qubit using the valley states of Si. X rotations are performed near the anticrossing between the $|L\rangle$ and $|R\rangle$ states at ϵ_x, while Z rotations are performed in the large detuning regime at ϵ_z. The red (blue) coloring signifies the weight of the state $|L_{v1}\rangle(|L_{v2}\rangle)$.

5.

CHAPTER 2

The valley states of silicon

As introduced in Chapter 1, there are many ways a qubit can be encoded into the energy states of electrons in silicon. To understand the limits and conditions of using these qubit basis states, it is pertinent to first comprehend their origin in this physical system. This chapter will focus on the source of the valley states in silicon, which define the two logical qubit states demonstrated in Chapter 5.

2.1 Silicon band structure

The silicon lattice shares the form of the diamond lattice that can be described as two inter-penetrating face centered cubic (fcc) lattices. The fcc lattice hosts atoms at the eight corners of a cube (black circles in Fig. 2.1a) and an additional six at the centers of each cube face (gray circles in Fig. 2.1a). A second lattice is offset from the first by $\left(\frac{1}{4}, \frac{1}{4}, \frac{1}{4}\right)$ the length of the cubic cell $a = 5.43$ Å (blue circles in Fig. 2.1a) [AM76].

Due to the periodicity of this lattice, an electron travelling through it experiences a periodic potential that is invariant under a translation $\mathbf{R}$: $U(\mathbf{r} + \mathbf{R}) = U(\mathbf{r})$, resulting in the electron's eigenstates to reflect this periodicity. Bloch's theorem states that under these conditions, the form of the electron's eigenstates can be chosen as a plane wave times a function $u(\mathbf{r})$ periodic with the crystal lattice [AM76]:

$$\psi_{n\mathbf{k}}(\mathbf{r}) = e^{i\mathbf{k}\cdot\mathbf{r}} u_{n\mathbf{k}}(\mathbf{r}), \tag{2.1}$$

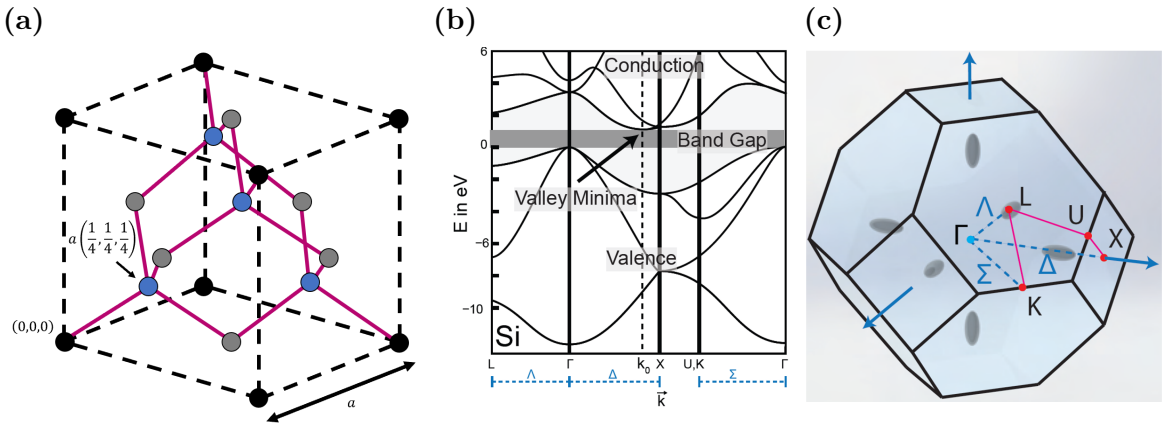

Figure 2.1: **(a)** Diamond lattice structure consisting of two fcc lattices offset from each other. **(b)** Energy band diagram for silicon adapted from [Sch17]. **(c)** First Brillouin zone for silicon adapted from [Sch17].

where $u_{n\mathbf{k}}(\mathbf{r})$ satisfies the periodic condition $u_{n\mathbf{k}}(\mathbf{r}+\mathbf{R}) = u_{n\mathbf{k}}(\mathbf{r})$. The index n reflects the fact that for a fixed $\mathbf{k}$, a family of solutions to the Schrödinger equation with discretely spaced eigenvalues $E_{n\mathbf{k}}$ exist for a given crystal potential, where each $E_{n\mathbf{k}}$ varies continuously with $\mathbf{k}$ and is known as an energy band. By mapping out the energy bands versus $\mathbf{k}$, one generates silicon's energy band diagram (Fig. 2.1b).

Band diagrams are useful as they help illustrate several important electronic properties of the crystal. These characteristics for electrons in silicon are almost exclusively determined by the relatively small number of electrons that are excited to the conduction band minimum [AM76]. As illustrated in Figs. 2.1b and 2.1c, the minima of the conduction band are located along the [100], [010], and [001] directions at k_0, which is $\sim 85\%$ of the distance to Brillouin zone boundary's square face ($k_0 = 0.85\frac{2\pi}{a}$) [ZDM12]. Fig. 2.1c illustrates this six-fold degeneracy as ellipsoids plotted within the Brillouin zone. These six degenerate minimums are known as the the six valleys of silicon's conduction band.

2.2 Valley states

2.2.1 Valley states in bulk silicon

To understand the behavior of the conduction electrons around these valley minima, we can rely on an effective mass approximation (EMA) to estimate the form of the conduction band energies $E_{c\mathbf{k}}$ as quadratic and centered at $\mathbf{k_0}$ [AM76]. For the valley located at $\mathbf{k_0} = k_0\hat{x}$, $E(\mathbf{k})$ has the form

$$E_{+x}(\mathbf{k}) \approx E_c + \frac{\hbar^2}{2}\left(\frac{(k_x - k_0)^2}{m_x} + \frac{k_y^2}{m_y} + \frac{k_z^2}{m_z}\right), \tag{2.2}$$

where m_i is the electron's effective masses along the direction of k_i [AM76]. For the valley minima in Si, the effective mass along the $\mathbf{k_0}$ axis is $m_l = 0.92m$, while the mass perpendicular to the axis is $m_t = 0.19m$, where m is the mass of the free electron [Gre90]. Arranging the like masses together in Eqn. 2.2 gives the local band shape around the $+x$ valley:

$$E_{+x}(\mathbf{k}) = E_c + \frac{\hbar^2}{2}\left(\frac{(k_x - k_0)^2}{m_l} + \frac{k_y^2 + k_z^2}{m_t}\right), \tag{2.3}$$

which is the equation of an ellipse and the reason for the ellipsoids shown in Fig. 2.1c. As will be explained in the following section, the electrons comprising the 2DEG in our device are confined to move along the transverse direction with effective mass $m_t = 0.19m$.

2.2.2 Lifting the degeneracy of valley states

Up until this point, I have only considered silicon's band structure and electrons in bulk silicon. This description is insufficient for the electrons trapped in quantum dots for a number of reasons that cannot be ignored. The two most important modifications to the valley states are the effects of the Si/SiGe heterostructure and gate confinement potentials.

When the Si quantum well is grown between two layers of SiGe, the lattice mismatch

between the Si well and SiGe buffer generates in-plane tensile strain. Silicon's lattice constant is $a = 5.431$ Å, while the average lattice constant for $Si_{0.7}Ge_{0.3}$ is 5.4928 Å [DEP64], leading to a 1% mismatch and the source of this strain. The resulting in-plane strain generated in the quantum well lifts the energies of the in-plane valleys by 200 meV above their out-of-plane counterparts [Sch97]. Because the SiGe layers are grown along the [001] direction, the in-plane valleys are those along k_x and k_y, leaving the ground state of the conduction band to consist of the two-fold degenerate z-valleys (see red lines Fig. 2.2a).

The remaining two-fold degeneracy of the z valleys is lifted by the quantum well confinement and electrical field applied along the z direction (blue lines in Fig. 2.2a) [BKE03, SCH09]. These two z valleys then become the basis states for the ground and first excited states of the quantum dot. Focusing on these two valleys, one can extend the effective mass approximation used in the preceding section to calculate the ground and excited eigenstates. Beginning with the unperturbed Bloch wave functions $\psi_{\mathbf{k}} = u_{\mathbf{k}}(\mathbf{r})e^{i\mathbf{k}\cdot\mathbf{r}}$ and energies $E(\mathbf{k})$ (Eqn. 2.3), one can look for solutions to the perturbed Schrödinger equation

$$[H_0 + U(\mathbf{r})]\,\psi(\mathbf{r}) = E\psi(\mathbf{r}), \tag{2.4}$$

where H_0 is the unperturbed Hamiltonian of bulk Si and $U(\mathbf{r})$ is the perturbing potential due to the electron's confinement inside the heterostructure. In this approximation, if one assumes the perturbing potential varies slowly on the scale of the lattice constant a and is small compared to the separation of energy bands, solutions to Eqn. 2.4 can take the form of a summation over the basis of the z valley Bloch states [FCT07, Ihn10, ZDM12, YRR13]:

$$\psi(\mathbf{r}) = \sum_{i=\pm z} \alpha_i u_{k_i}(\mathbf{r})e^{ik_i z}F_i(\mathbf{r}). \tag{2.5}$$

The constants α_i both satisfy $|\alpha_i| = \frac{1}{\sqrt{2}}$ and describe the relative phase between the two valleys, $u_{k_i}(\mathbf{r})e^{ik_i z}$ are the Bloch functions that describe the wave forms for atomic length scales, and $F_i(\mathbf{r})$ are the slowly varying envelope functions that describe long

wavelength modulations due to confinement in the quantum well. Because the effective masses for both z valleys are equal, their envelope functions are equivalent: $F_i(\mathbf{r}) = F(\mathbf{r})$ [FCT07].

The two valley states are coupled due to the abrupt change at the Si/SiGe interface; however, this is difficult to capture within the effective mass approximation because the sharp change in confining potential at the interface violates the assumption of a slowly varying potential with respect to a. To alleviate this issue, one can express the valley interaction through an effective coupling potential $\mathcal{V}_v(z)$, which can be treated as a delta function over the long length scale where EMA is valid [FCT07]:

$$\mathcal{V}_v(z) = v_v \delta(z - z_i), \tag{2.6}$$

where v_v is the strength of the valley coupling and z_i is the location of the smooth interface. This valley coupling is incorporated into the EMA framework through perturbation theory, resulting in a valley-orbit coupling that lifts the degeneracy of the z valleys:

$$\Delta_{VO} = 2v_v e^{2ik_0 z_i} {F^{(0)}}^2(z_i) = |\Delta_{VO}| e^{i\phi}, \tag{2.7}$$

where the zeroth order envelope function is defined as $F^{(0)}(z)$ and the valley splitting is $E_{VS} = 2|\Delta_{VO}|$. This result is illuminating, because it shows the importance the interface has on the valley splitting, in particular, the magnitude of the envelope function evaluated at the interface (I will further discuss the significance of this relationship shortly). The ground and excited eigenstates become symmetric and antisymmetric valley doublets:

$$\psi_{\pm}(z) = \frac{1}{\sqrt{2}} \left[u_{-k_0}(z) e^{-ik_0 z + i\phi} \pm u_{k_0}(z) e^{ik_0 z} \right] F(z). \tag{2.8}$$

The additional term ϕ describes the phase difference between the valleys due to the valley orbit interaction. Fig. 2.2b illustrates the amplitudes of these two states within the quantum well. Fast oscillations have a wavelength of $\sim 2\pi k_0^{-1} = 0.65$ nm and

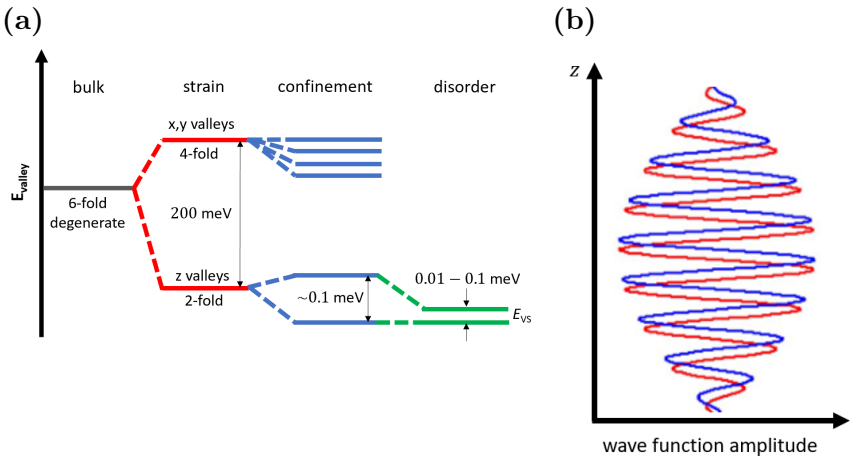

Figure 2.2: **(a)** Effects of strain, confinement, and disorder on the valley splitting in Si. **(b)** Ground and excited eigenstates. The slowly varying envelope spans the quantum well, while the fast oscillations are on the order of the atomic spacing. The difference in phase between the eigenstates is adjusted by specifics of the interface. Image is adapted from [ZDM12].

originate from the Bloch functions in Eqn. 2.8, while the slowly varying envelope $F(z)$ modulates these rapid oscillations within the quantum well.

2.2.3 Effects of interface disorder

One of the assumptions made in Eqn. 2.6 was a smooth Si/SiGe interface that does not change with respect to x or y. In reality, interface disorder is present in every system, ruining this assumption, and leads to an important modification of the valley splitting. There are two important types of disorder that can occur at the interface: alloy disorder in the $Si_{1-x}Ge_x$ buffer and step disorder, both of which are discussed in [ZDM12] and I will briefly summarize in the following.

Alloy disorder encompasses the various situations that the $Si_{1-x}Ge_x$ buffer has in-plane spatial dependence. Because SiGe is a random alloy, the order of the Si or Ge atoms on the lattice is not regular but random. This randomness also contributes to a variable lattice spacing, as Si atoms want to pull neighboring Si atoms closer and push

Ge atoms away. Finally, the concentration of Si to Ge can vary due to fluctuations in the growth conditions, increasing the alloy disorder. In addition to alloy disorder, misalignment between the wafer growth and z direction results in steps so the interface is no longer flat. In addition to the steps changing the interface coordinate z_i by their very nature, the steps are not perfect lines, causing additional disarray.

When the wave function spanning this disorder no longer experiences a uniform interaction with the interface, the integrated valley-orbit coupling $|\Delta_{VO}|e^{i\phi}$ becomes suppressed due to interference among the differing phase contributions [ZDM12, FCT07, TH19]. As $|\Delta_{VO}|$ decreases, so too does the valley splitting of the two lowest eigenstates (see green lines in Fig. 2.2a). This reduced E_{VS} is often small enough that it becomes the energy spacing defining the two lowest states of a quantum dot, meaning the valley physics cannot be ignored. Moreover, an additional consequence of disorder is the adjustment of ϕ. While ϕ is global phase that is not too important for single dot physics, it will play a major role in the coupling of two dots, which I discuss in the next section. The dependence of the valley splitting on interface disorder has been a challenging problem for the quantum dot qubit community. Because this disorder is difficult to control when growing wafers, the valley splitting for a quantum dot not only varies from device to device, but also dot to dot. This issue is compounded by the fact that one cannot determine the valley splitting until the device is fabricated and tested, which greatly harms yield when one desires identical qubits.

2.3 Description of valley states within a double quantum dot

For the experiments described in Chapter 5, we encoded a qubit using the valley states within double quantum dot. Building on Section 2.2, a complete description of the system will include not only the two valley states for the left and right dots, but also the interactions between these four valley states. Specifically, the following subsections will describe the role valley states play regarding an electron tunneling between quantum dots.

2.3.1 Interdot tunneling between valley states

Consider the two localized eigenstates on the left quantum dot to be symmetric and antisymmetric valley doublets in Eqn. 2.8 and labeled as $|L, v_{\pm}\rangle$ and similarly for the right dot with label R. In the absence of interface disorder, the symmetric eigenstates in the left and right dots ($|L(R), v_{+}\rangle$) have the same phase, while they are 90° out of phase with respect to the antisymmetric eigenstates ($|L(R), v_{-}\rangle$). Consequently, the wave functions of $|L, v_{+}\rangle$ and $|R, v_{+}\rangle$ overlap, and an electron can tunnel between these two states, while it cannot tunnel between $|L, v_{+}\rangle$ and $|R, v_{-}\rangle$ [SCJ07]. In other words, the valley index is preserved when tunneling between dots.

Now consider the same case with disorder present. As was shown in the previous section, disorder adjusts not only the magnitude of the valley splitting, but also the phase ϕ between z valleys. When accounting for two different dots under a disordered interface, it is generally the case that $\phi_L \neq \phi_R$. In the presence of this phase difference, $|L, v_{+}\rangle$ is no longer necessarily out of phase with $|R, v_{-}\rangle$, lifting the tunneling restriction between states with different valley indices [GEC13, SCJ07, ZHC17].

2.3.2 Hamiltonian for valley states in a double quantum dot

Before compiling this information into a Hamiltonian that describes all four valley states and their interactions, let me return to the simple charge qubit case introduced in Section 1.5.1. Consider an electron that can tunnel between two dots with tunnel coupling Δ, where its position is controlled through the detuning of the dot energy levels ϵ. In the basis $\{|R\rangle, |L\rangle\}$, the Hamiltonian describing this system is

$$H = \begin{pmatrix} \epsilon/2 & \Delta \\ \Delta & -\epsilon/2 \end{pmatrix}. \tag{2.9}$$

The eigenenergies of this Hamiltonian are shown in Fig. 2.3a. For negative detunings, the charge is likely to be found in the right dot. For positive detunings, this probability

switches to the left dot. At zero detuning, the eigenstates are mixtures of the two charge states: $|L\rangle \pm |R\rangle$.

Now I will return to the case for an electron in Si where the valley states are included for the left and right dots. Because there are two valley eigenstates for each dot, the charge state splits into two: $|L\rangle \rightarrow |L, v_-\rangle, |L, v_+\rangle$ and similarly for $|R\rangle$, where the valley splitting E_{VS} separates the valleys of each dot. Note that the valley splitting for the left and right dots are often not equal, as each dot sees a different interface due to disorder.

While tunneling between valley states on the same dot is assumed to be forbidden (e.g., $|L, v_-\rangle$ and $|L, v_+\rangle$ do not overlap), the previous section outlined how intervalley tunneling is allowed when an electron tunnels to a neighboring dot. If one assumes the dot positions are constant over the relevant range of detuning, the coupling elements that describe the tunneling between valley states of different dots can be estimated as fixed terms. Accounting for the valley splitting in each dot and the tunneling between them, the final Hamiltonian takes the following form in the basis $\{|R, v_-\rangle, |R, v_+\rangle, |L, v_-\rangle, |L, v_+\rangle\}$:

$$H = \begin{pmatrix} \epsilon/2 & 0 & \Delta_1 & -\Delta_2 \\ 0 & \epsilon/2 + E_{VS,R} & -\Delta_3 & \Delta_4 \\ \Delta_1 & -\Delta_3 & -\epsilon/2 & 0 \\ -\Delta_2 & \Delta_4 & 0 & -\epsilon/2 + E_{VS,L} \end{pmatrix}, \tag{2.10}$$

where the Δ terms represent the interdot valley coupling. The simple charge qubit energy diagram transforms to that in Fig. 2.3b. Although the presence of small valley splittings complicates spin-based qubits, one can utilize the valley states in a single dot as a two-level system to encode quantum information. This manipulation of the valley states is explored in Chapter 5.

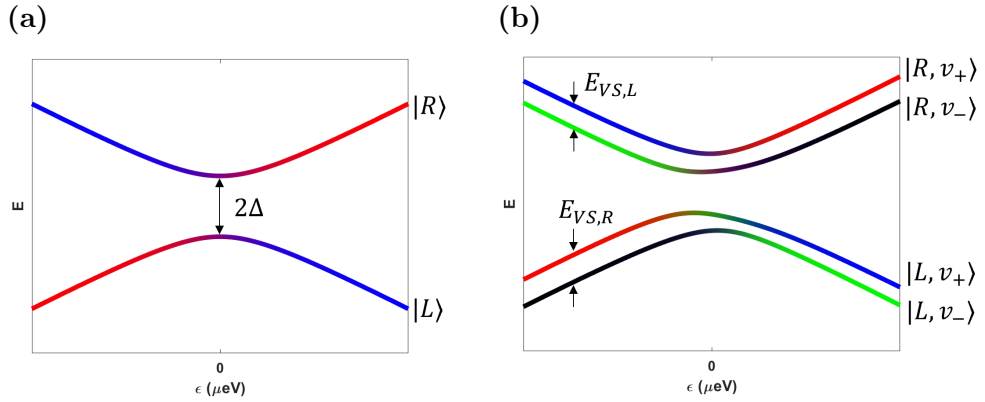

Figure 2.3: **(a)** Energy diagram for an electron shared between two quantum dots. Red signifies the weight of the $|R\rangle$ charge state, while blue corresponds to $|L\rangle$. **(b)** Energy diagram for an electron in a double quantum dot with the two valley states per dot included.

CHAPTER 3

The spin states of holes in germanium

Arguably the most successful type of qubit encoding in semiconductor quantum dots utilizes the spin degree of freedom. Not only does the spin of an electron or hole naturally form a two-state system, but its weak coupling to the environment results in long coherence times that can exceed seconds [BLN21, TTM12]. While the majority of the spin qubit community's focus has been on exploiting electrons in silicon, rapid progress has been made with holes in germanium (Ge) in recent years. From the demonstration of quantum dots in 2018 [HFS18] to a four-qubit quantum processor in 2021 [HLR21], the hole spin states of Ge have shown to be a promising platform for quantum computation. Chapter 6 showcases one such qubit encoded in the singlet-triplet states of two holes. This chapter will delve into the origin of these spin states and the theoretical foundation for their use as qubits.

3.1 Germanium band structure

Germanium shares the diamond lattice structure (Fig 2.1a) and same Brillouin zone as silicon. In contrast to silicon, the conduction band minima are located at the edge of the Brillouin zone along the [111] directions, creating four degenerate ellipsoidal pockets (see Fig. 3.1). The highest valence bands are similarly located at the $\mathbf{k} = 0$ Γ-point [AM76]. I will focus my attention on these valence bands, as they form the ground state for the system I am interested in.

Unlike electrons in the conduction band, the valance band states are p-like with angular momentum $l = 1$, subjecting the charge carriers to a strong spin-orbit interaction (Δ_{so}) proportional to $l{\cdot}s$. Because $l{\cdot}s = \frac{1}{2}(J^2{-}l^2{-}s^2)$, Δ_{so} splits the six-fold degeneracy of the valence band states, where the states with total angular momentum $J = 1/2$, known as the split-off band, are shifted down by Δ_{so} from the states with $J = 3/2$ (Fig. 3.1a) [HDK08]. In a crystal, the spin-orbit interaction is a relativistic effect that originates from the hole moving in the electric field of its confining potential. In the rest frame of the charge, the Lorentz transformation of this electric field has both an electric and magnetic field component. The magnetic field interacts with the spin of the charge, resulting in the energy splitting of different spin states [GA20]. The two topmost valence bands are distinguished by their projection of the total angular momentum: $j_z = \pm 3/2$ and $j_z = \pm 1/2$. Because the spin-orbit coupling is much larger than other energy scales in the system, the SO band is usually neglected or incorporated via perturbation theory.

Borrowing from the effective mass theory discussed in Section 2.2.1, the effective mass of the charge carriers in these energy bands is related to the band's curvature:

$$(m^*)^{-1} = \frac{1}{\hbar^2}\frac{d^2E(k)}{dk^2}. \tag{3.1}$$

From Fig. 3.1a, it is evident that the $j_z = 3/2$ band (red) does not bend as sharply as the $j_z = 1/2$ band (green), and therefore has lower curvature. From Eqn. 3.1, we can see this translates to a larger effective mass m^* for the $j_z = 3/2$ band, which is the basis for why it is named the heavy-hole (HH) band. Similarly, the $j_z = 1/2$ band (green) is labeled the light-hole (LH) band in comparison.

3.1.1 Holes

Before continuing, it is beneficial to introduce the concept of holes as charge carriers, as the term hole has already appeared in this discussion of valence bands. Consider the

current contributed by all electrons occupying states in a given band [AM76]:

$$\mathbf{j} = (-e) \int_{\text{occupied}} \frac{d\mathbf{k}}{4\pi^3} \mathbf{v}(\mathbf{k}). \tag{3.2}$$

Using the fact that a completely filled band carries no current,

$$0 = \int_{\text{zone}} \frac{d\mathbf{k}}{4\pi^3} \mathbf{v}(\mathbf{k}) = \int_{\text{occupied}} \frac{d\mathbf{k}}{4\pi^3} \mathbf{v}(\mathbf{k}) + \int_{\text{unoccupied}} \frac{d\mathbf{k}}{4\pi^3} \mathbf{v}(\mathbf{k}), \tag{3.3}$$

Eqn. 3.2 can be rewritten as

$$\mathbf{j} = (+e) \int_{\text{unoccupied}} \frac{d\mathbf{k}}{4\pi^3} \mathbf{v}(\mathbf{k}). \tag{3.4}$$

Therefore, the current generated by electrons occupying energy states in a band becomes equivalent to the situation where those states are unoccupied and all other levels in the band were occupied by particles with charge $+e$ [AM76]. This flipped approach is convenient and efficient when dealing with an energy band that is almost completely filled with electrons. For example, consider a band that has 99/100 states occupied by electrons. One can either track all 99 electrons and determine $\mathbf{j}$ using Eqn. 3.2 or solve the problem of 1 fictitious particle with charge $+e$ occupying the band and all other states unoccupied. The latter method is of course much easier. Because this picture utilizes the absence of electrons, these positively charged particles are called *holes*. Because the valence bands in a semiconductor are almost always mostly full, it is convenient to use the this hole picture for the valence band.

A second benefit of using this hole picture emerges from the motion of electrons at the top of the valence band under applied fields. Similar to Eqn. 2.3, we can approximate the energy E of an electron at $\mathbf{k_0} = 0$ in the valance band by expanding E around $\mathbf{k_0}$:

$$E(\mathbf{k}) \approx E(\mathbf{k_0}) - \frac{\hbar^2}{2m^*}(\mathbf{k} - \mathbf{k_0})^2, \tag{3.5}$$

where m^* is a positive quantity because E is maximum at $\mathbf{k_0}$ [AM76]. Looking at the

group velocity of an electron near this $\mathbf{k_0}$,

$$\mathbf{v} = \frac{1}{\hbar}\frac{\partial E}{\partial \mathbf{k}} = -\frac{\hbar}{m^*}(\mathbf{k} - \mathbf{k_0}), \tag{3.6}$$

leads to an acceleration in the opposite direction of $\dot{\mathbf{k}}$:

$$\mathbf{a} = \frac{dv}{dt} = -\frac{\hbar}{m^*}\dot{\mathbf{k}}. \tag{3.7}$$

Electrons near the top of the valence band therefore *look* like they have negative mass, as they move in the opposite direction of an applied force from what one would expect [AM76]. Consider the case of an electron at $\mathbf{k_0}$ in an applied electric field $\mathbf{E}$, where we make use of the relation in Eqn. 3.7:

$$\hbar\dot{\mathbf{k}} = (-e)\mathbf{E} \tag{3.8}$$

$$(-m^*)\mathbf{a} = (-e)\mathbf{E} \longleftrightarrow (+m^*)\mathbf{a} = (+e)\mathbf{E}. \tag{3.9}$$

The motion of the electron with apparent negative mass behaves the same as a positively charged particle (hole) with positive mass, which is much more intuitive.

3.2 Lifting the HH-LH degeneracy

Let us return to the two topmost valence bands in Fig. 3.1a. These bands are degenerate in bulk Ge, but separated due to strain in the heterostructure and 2D confinement within the quantum well. Just like in the case in Chapter 2 with silicon sandwiched between two SiGe buffers, a germanium well placed between two SiGe buffers will experience strain due to the lattice mismatch between the layers. The lattice constants of Ge and Si at room temperature are 5.64 and 5.43 Å respectively [Dav98]; therefore, the Ge well will compress to match the smaller lattice spacing of the $Si_{1-x}Ge_x$ substrate. This compressive strain gives rise to a splitting between the HH and LH bands Δ_{HL} [TMW21, Dav98], where the mechanism responsible for splitting will be discussed more in Section 3.5.

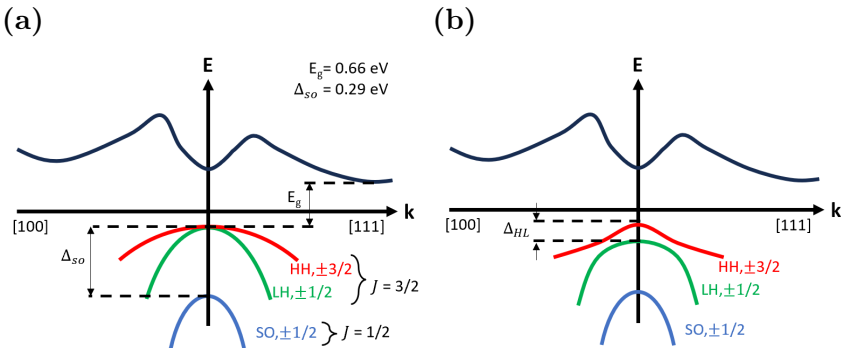

Figure 3.1: **(a)** Ge band structure adapted from [NSM] and [HDK08]. **(b)** Ge band structure when quantum confinement and strain are included. Image adapted from [HDK08].

The 2D confinement of the valence band states in the quantum well works with strain to further increase Δ_{HL}. As was mentioned in Section 3.1, wave functions in the HH and LH bands have the symmetry of p orbitals, and it turns out these p orbitals are oriented along different crystal axes that is dependent on the band. HH states are comprised of p orbitals pointed in the x-y plane, making it difficult for holes to travel through the crystal in the z direction (along the growth axis) and, therefore, HH states have a large effective mass along z. In contrast, LH orbital states are made up mostly of p orbitals pointed in the z direction, where travel is easier along z. The heavier effective mass along z for the HH states translates to a bound state that is deeper in the quantum well compared to LH states, lowering the LH band's energy [Dav98].

The combined effects of strain and confinement result in HH-LH splittings on the order of $\sim$ 100 meV [TMW21, CRZ23], and the final band structure for quantum dots appears as that of Fig. 3.1b. The ground state of the quantum dot is then predominantly HH character, where various factors lead to a small mixture of LH states. Although the magnitude of this mixture is quite small, it will be shown that even minimal mixing between the HH and LH bands results in immense changes for the hole system.

3.3 Luttinger-Kohn model of the valence band

Recall the Bloch wave functions introduced in Section 2.1: $\psi_{n\mathbf{k}}(\mathbf{r}) = e^{i\mathbf{k}\cdot\mathbf{r}}u_{n\mathbf{k}}(\mathbf{r})$. If we input this function into the Schrödinger equation, we can isolate the periodic portion of the Bloch function letting H act on the exponential term:

$$\left[\frac{\hat{\mathbf{p}}^2}{2m_0} + V(\mathbf{r})\right] e^{i\mathbf{k}\cdot\mathbf{r}}u_{n\mathbf{k}}(\mathbf{r}) = E_{n\mathbf{k}}e^{i\mathbf{k}\cdot\mathbf{r}}u_{n\mathbf{k}}(\mathbf{r}), \tag{3.10}$$

where $\hat{\mathbf{p}} = -i\hbar\nabla$ acting on $e^{i\mathbf{k}\cdot\mathbf{r}}$ gives $\hbar\mathbf{k}$, and the final equation reads

$$\left\{\left[\frac{\hat{\mathbf{p}}^2}{2m_0} + V(\mathbf{r})\right] + \left[\frac{\hbar}{m_0}\mathbf{k}\cdot\hat{\mathbf{p}} + \frac{\hbar^2k^2}{2m_0}\right]\right\} u_{n\mathbf{k}}(\mathbf{r}) = E_{n\mathbf{k}}u_{n\mathbf{k}}(\mathbf{r}). \tag{3.11}$$

The leftmost terms describe a free electron (or hole), while the second boxed terms include an adjustment to the free particle's energy and a $\mathbf{k}\cdot\hat{\mathbf{p}}$ term that gives this approach its name: the $\mathbf{k}\cdot\hat{\mathbf{p}}$ model. Using a complete set of basis functions, such as the set of eigenfunctions at $\mathbf{k} = 0$, $\{u_{n\mathbf{0}}(\mathbf{r})\}$, one can transform this equation into a matrix equation and solve for the Bloch functions exactly. Approximations can be made by considering a subset of this basis. For example, the Kane model without spin incorporates the s-like wave function of the conduction band ($|S\rangle$) and the three topmost valance bands, which have p_x, p_y, and p_z orbital symmetry ($|X\rangle$, $|Y\rangle$, $|Z\rangle$) [Kan56, Dav98].

For a hole system where only the topmost valance bands are occupied, a natural choice of basis states are the four states defined by the projection of angular momentum: $|j_z = \pm 3/2\rangle$ and $|j_z = \pm 1/2\rangle$. These four states are related to the above p orbital states

in the following manner [Dav98]:

$$\left|\frac{3}{2},+\frac{3}{2}\right\rangle = |+1\uparrow\rangle, \tag{3.12}$$

$$\left|\frac{3}{2},+\frac{1}{2}\right\rangle = +\sqrt{\frac{1}{3}}|+1\downarrow\rangle - \sqrt{\frac{2}{3}}|0\uparrow\rangle, \tag{3.13}$$

$$\left|\frac{3}{2},-\frac{1}{2}\right\rangle = -\sqrt{\frac{1}{3}}|-1\uparrow\rangle - \sqrt{\frac{2}{3}}|0\downarrow\rangle, \tag{3.14}$$

$$\left|\frac{3}{2},-\frac{3}{2}\right\rangle = |-1\downarrow\rangle, \tag{3.15}$$

where $|0\rangle = |Z\rangle$ and $|\pm 1\rangle = \sqrt{\frac{1}{2}}(|X\rangle + i|Y\rangle)$. From these basis states, we can deduce the character of the HH and LH states touched upon in the previous section. The HH states (composed of $|X\rangle$ and $|Y\rangle$) have p orbital symmetries along the x and y directions, while the LH states are predominately have p_z symmetry. Focusing on these states is the idea behind the 4x4 Luttinger-Kohn Hamiltonian [WCP08, SKZ21] (presented in the spherical approximation):

$$H_{LK} = -\frac{\hbar^2}{2m_0}\left[\left(\gamma_1 + \frac{5}{2}\gamma_s\right)k^2 - 2\gamma_s(\mathbf{k}\cdot\mathbf{J})^2\right], \tag{3.16}$$

where $\gamma_1 \approx 13$ and $\gamma_s \approx 5$ for Ge [WCP08, SKZ21]. The first term in Eqn. 3.16 can be thought of as the kinetic energy term, while the second term originates from the spin-orbit coupling that cannot be ignored in this system. The matrix representation of this Hamiltonian in the basis $\{|\,\frac{3}{2},\frac{3}{2}\,\rangle, |\,\frac{3}{2},\frac{1}{2}\,\rangle, |\,\frac{3}{2},-\frac{1}{2}\,\rangle, |\,\frac{3}{2},-\frac{3}{2}\,\rangle\}$ is as follows [WCP08, WSV22a]:

$$H_{LK} = \begin{pmatrix} P+Q & L & M & 0 \\ L^* & P-Q & 0 & M \\ M^* & 0 & P-Q & -L \\ 0 & M^* & -L^* & P+Q \end{pmatrix}, \tag{3.17}$$

where

$$P = -\frac{\hbar^2}{2m_0}\gamma_1 k^2, \tag{3.18}$$

$$Q = \frac{\hbar^2}{2m_0}\gamma_s(2k_z^2 - k_x^2 - k_y^2), \tag{3.19}$$

$$L = \frac{\hbar^2}{2m_0}2\sqrt{3}\gamma_s k_- k_z, \tag{3.20}$$

$$M = \frac{\hbar^2}{2m_0}\sqrt{3}\gamma_s k_-^2, \tag{3.21}$$

and $k_- = k_x - ik_y$. By examining the diagonal elements of Eqn. 3.17 and grouping k_x and k_y terms, we can approximate the effective masses for the heavy and light holes for the in-plane motion in the quantum dot:

$$m^*_{HH,LH} \approx \frac{m_0}{\gamma_1 \pm \gamma_s} = (0.05, 0.13)m_0. \tag{3.22}$$

From Eqn. 3.22, it is apparent the heavy hole mass is actually less than light hole mass for motion in the x-y plane. This is reversed from the case in bulk Ge, and it is customary to continue using the same naming convention for the HH and LH bands (i.e., the HH band corresponds to lighter $j_z = \pm 3/2$ states). Because the ground state has a predominantly HH character, holes in Ge quantum dots are are quite light compared to the bare electron, leading to large orbital-level spacings that are useful when encoding a qubit in the two lowest energy levels of the dot [SKZ21].

3.4 Including the Zeeman interaction

Absent from Eqn. 3.16 are the effects of an external magnetic field $\mathbf{B}$. The simplest way to incorporate $\mathbf{B}$ into the Hamiltonian is through the Zeeman interaction, where there are two terms linear in $\mathbf{B}$ that come into play for this hole system [Win03]:

$$H_z = -2\kappa\mu_B \mathbf{J}\cdot\mathbf{B} - 2q\mu_B(J_x^3 B_x + J_y^3 B_y + J_z^3 B_z), \tag{3.23}$$

where $\kappa = 3.41$ is the bulk (isotropic) g-factor, $q = 0.07$ is the anisotropic Zeeman term, and μ_B is the Bohr magneton (cited values are for Ge) [WKV16]. Because $\kappa \gg q$ in Ge, the second term can be neglected for most analyses and I will continue to do so here unless noted otherwise. Once again, it is useful to show the explicit matrix form of H_z [WCP08]:

$$H_z = -2\kappa\mu_B \begin{pmatrix} \frac{3}{2}B_z & \frac{\sqrt{3}}{2}B_- & 0 & 0 \\ \frac{\sqrt{3}}{2}B_+ & \frac{1}{2}B_z & B_- & 0 \\ 0 & B_+ & -\frac{1}{2}B_z & \frac{\sqrt{3}}{2}B_- \\ 0 & 0 & \frac{\sqrt{3}}{2}B_- & -\frac{3}{2}B_z \end{pmatrix}, \tag{3.24}$$

where $B_\pm = B_x \pm iB_y$. Consider the case when $\mathbf{B} = B\hat{z}$ is oriented along the growth direction. From the diagonal elements of this matrix, we can read off the Zeeman energy splitting for the HH states is $\Delta E_{HH} = 6\kappa\mu_B B_z$, while the LH state are separated by $\Delta E_{LH} = 2\kappa\mu_B B_z$. However, for the case of an in-plane magnetic field, the situation is quite different: $\Delta E_{HH} = 0$ and $\Delta E_{LH} = 4\kappa\mu_B B_\parallel$.

I would like to emphasize this dependence of the Zeeman splitting on the orientation of the magnetic field is quite remarkable and be a useful tuning knob for qubits. The anisotropy for the HH states originates from the rigid quantization axis induced by the HH-LH splitting that points along the growth direction [Win03, WCP08]. For an out-of-plane magnetic field, the Zeeman term does not compete with the $B = 0$ spin orientation and a large Zeeman splitting can be observed. For in-plane fields, the Zeeman term competes with the out-of-plane spin orientation and is thus suppressed [Win03, WCP08]. For typical magnetic fields used in experiment, the in-plane magnetic field is never large enough ($\sim \Delta_{HL}$) to overcome the forced quantization axis. It is interesting to note this competition between the Zeeman terms and quantization axis along $\hat{z}$ is only present for the HH ($j_z = \pm 3/2$) states. The two LH states ($j_z = \pm 1/2$) can always be combined to form an eigenstate of angular momentum for any orientation of the quantization axis [Win03].

The Zeeman effect is typically observed by analyzing the linear separation of energy levels as a function of B. For convenience, the system's linear response is usually written

with an effective g-tensor:

$$H_z = \frac{\mu_B}{2}\mathbf{g}\cdot\sigma\cdot\mathbf{B}, \tag{3.25}$$

where $\mathbf{g}$ is a tensor and σ are the Pauli spin matrices. For equation 3.24, the g-tensors for the HH and LH cases in the basis defined by the crystal axes read as follows (where I include the anisotropic Zeeman term q):

$$\mathbf{g}_{HH} = \begin{pmatrix} 3q & 0 & 0 \\ 0 & 3q & 0 \\ 0 & 0 & 6\kappa + \frac{27}{2}q \end{pmatrix} = \begin{pmatrix} 0.21 & 0 & 0 \\ 0 & 0.21 & 0 \\ 0 & 0 & 21.4 \end{pmatrix} \tag{3.26}$$

$$\mathbf{g}_{LH} = \begin{pmatrix} 4\kappa + 10q & 0 & 0 \\ 0 & 4\kappa + 10q & 0 \\ 0 & 0 & 2\kappa + \frac{1}{2}q \end{pmatrix} = \begin{pmatrix} 14.3 & 0 & 0 \\ 0 & 14.3 & 0 \\ 0 & 0 & 7.3 \end{pmatrix} \tag{3.27}$$

As I have already established, the ground state for holes in quantum dots is primarily composed of HH states. From the above matrices, we can expect a large Zeeman splitting for magnetic fields in the out-of-plane direction compared to the in-plane one due to $g_\perp \gg g_\parallel$. Moreover, by comparing the g-factors in these two directions, increasing the weight of the LH states in the ground state of the quantum dot results in a decrease in $g_\perp$ and increase in $g_\parallel$. I have not yet reviewed any mechanisms responsible for mixing the HH and LH states, but this point will be crucial for interpreting the experimental results of Chapter 6.

It should be noted other sources separate from H_z also contribute to the g-tensor. These sources include the spin-orbit term in Eqn. 3.16, structure inversion asymmetry of the confining potential (Rashba spin-orbit coupling), and bulk inversion asymmetry (Dresselhaus spin-orbit coupling) [WCP08, WFE]. As stated above, any mixing between HH and LH states will also alter the g-tensor. Because of these mechanisms, the out-of-plane g-factor is often much smaller than $6\kappa + \frac{27}{2}q$ [WKV16, AGK13, MS17, DMS14, NDZ03].

3.5 Strain

3.5.1 Including strain into the Luttinger-Kohn model

Section 3.2 touched on the importance of strain in the quantum well lifting the degeneracy of the HH and LH states. The consequences of strain can be discussed in more quantitative detail by including strain directly into the Luttinger-Kohn Hamiltonian.

When a crystal is under the effects of a uniform deformation, it may retain its periodicity such that the Bloch theorem can be applied, with a modified period equal to the new lattice spacing [Chu95]. A simple example showing the effects of a deformation on the crystal lattice is shown in Fig. 3.2. When no stress is applied (the unstrained case), atom A is at position $\mathbf{r} = (x, y, z)$. When stress is applied to the crystal, such as when the Ge lattice spacing is forced to match that of SiGe, the lattice becomes strained (3.2b). The same atom A is now found at $\mathbf{r} = (x', y', z')$, where the strained and unstrained coordinate systems are related by [Chu95]

$$\mathbf{x}' = (1 - \varepsilon_{xx})\hat{\mathbf{x}} + \varepsilon_{xy}\hat{\mathbf{y}} + \varepsilon_{xz}\hat{\mathbf{z}}, \tag{3.28}$$

$$\mathbf{y}' = \varepsilon_{yx}\hat{\mathbf{x}} + (1 - \varepsilon_{yy})\hat{\mathbf{y}} + \varepsilon_{yz}\hat{\mathbf{z}}, \tag{3.29}$$

$$\mathbf{x}' = \varepsilon_{zx}\hat{\mathbf{x}} + \varepsilon_{zy}\hat{\mathbf{y}} + (1 - \varepsilon_{zz})\hat{\mathbf{z}}. \tag{3.30}$$

These ε_{ij} are the strain components and are often expressed as a tensor:

$$\varepsilon = \begin{pmatrix} \varepsilon_{xx} & \varepsilon_{xy} & \varepsilon_{xz} \\ \varepsilon_{yx} & \varepsilon_{yy} & \varepsilon_{yz} \\ \varepsilon_{zx} & \varepsilon_{zy} & \varepsilon_{zz} \end{pmatrix}. \tag{3.31}$$

Typically, homogeneous strain is assumed, where $\varepsilon_{ij} = \varepsilon_{ji}$. The diagonal elements represent normal strain, where a force along an axis deforms the crystal along that *same* axis. The off-diagonal elements represent shear strain, where a force along one axis deforms the crystal along a *different* axis.

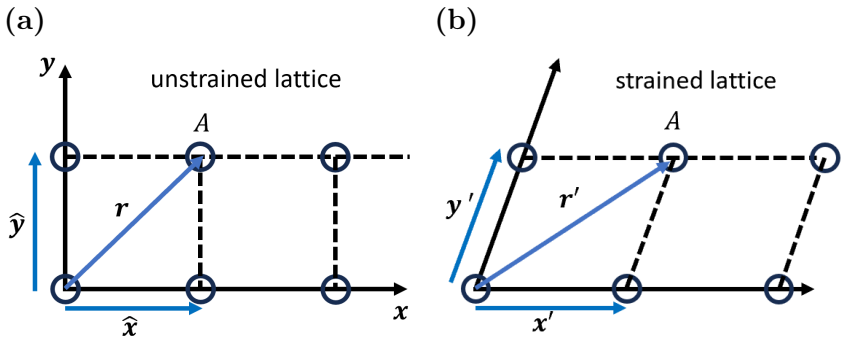

Figure 3.2: **(a)** Unstrained crystal lattice **(b)** Strained crystal lattice. Both images adapted from [Chu95].

Pikus and Bir incorporated the effect of strain on the valence bands using deformation potential theory in their work [BP74]. By including strain, each nonzero matrix element in Eqn. 3.17 is modified by an additional term:

$$P \to P + P_\varepsilon, \qquad Q \to Q + Q_\varepsilon, \tag{3.32}$$

$$L \to L + L_\varepsilon, \qquad M \to M + M_\varepsilon, \tag{3.33}$$

where the strain elements are given as

$$\begin{aligned} P_\varepsilon &= -a_v(\varepsilon_{xx} + \varepsilon_{yy} + \varepsilon_{zz}) \\ Q_\varepsilon &= -\frac{b}{2}(\varepsilon_{xx} + \varepsilon_{yy} - 2\varepsilon_{zz}) \\ L_\varepsilon &= -d(\varepsilon_{xz} - i\varepsilon_{yz}) \\ M_\varepsilon &= \frac{\sqrt{3}}{2}b(\varepsilon_{xx} - \varepsilon_{yy}) - id\varepsilon_{xy}, \end{aligned} \tag{3.34}$$

where $a_v = 2, b = -2.16$, and $d = -6.06$ eV are deformation potentials for the case of Ge [FL96, TMW21]. Not only does the introduction of strain alter the HH-LH splitting, but also contributes to the mixing of the two bands. For example, consider the case of biaxial strain where $\varepsilon_{xx} = \varepsilon_{yy} \neq \varepsilon_{zz}$, $\varepsilon_{zz} = -C\varepsilon_{xx}$, and all shear strain elements are zero. The constant C is related to the elastic stiffness constants of the material. At $\mathbf{k} = 0$,

the modified Luttinger-Kohn Hamiltonian only contains the Pikus-Bir terms, and the splitting between the HH and LH bands is given by

$$\Delta_{HL}(\mathbf{k}=0) = |2Q_\varepsilon| = 2b(\varepsilon_{xx} - \varepsilon_{zz}) = 2bC\varepsilon_{xx}. \tag{3.35}$$

As mentioned in Section 3.2, this simple example demonstrates the important role strain plays in lifting the degeneracy of the HH and LH bands.

3.5.2 Strain generated from gate electrodes

Up until this point, I have only considered the strain induced by the lattice mismatch between the Ge quantum well and SiGe substrate. However, strain also originates from the difference in thermal contraction between the metal gate electrodes and SiGe substrate (see Fig. 3.3). This contribution creates a variable strain profile that varies on the length scale of the gate width [CRZ23, LMM21]. Consequently, one should also expect the strain's influence on the HH/LH states to vary across this length scale. As Fig. 3.3b illustrates, the further away the quantum well is from the metal-substrate interface, the less of an impact this additional strain will have on the hole wave functions. Moreover, one can reduce this strain by electing to use a material with a thermal expansion coefficient closer to that of the substrate (e.g., palladium's coefficient is closer to that of SiGe when compared to gold).

However, it is often the case that as the crystal is deformed, both normal and shear strain have an effect on the bands. Generally, when the lattice is compressed along the in-plane directions, it also stretches in the out-of-plane direction [CRZ23]. When the shear effects can no longer be ignored, we can see from Eqns. 3.17 and 3.34 that the shear components (L_ε and M_ε) directly induce mixing between the HH and LH bands. While the shear components have been measured to be one to two orders of magnitude smaller than the diagonal strain terms, both can undergo similar *changes* around the electrodes [CRZ23]. Accordingly, a hole trapped in the quantum well of a heterostructure can experience different magnitudes of strain as its position shifts underneath the

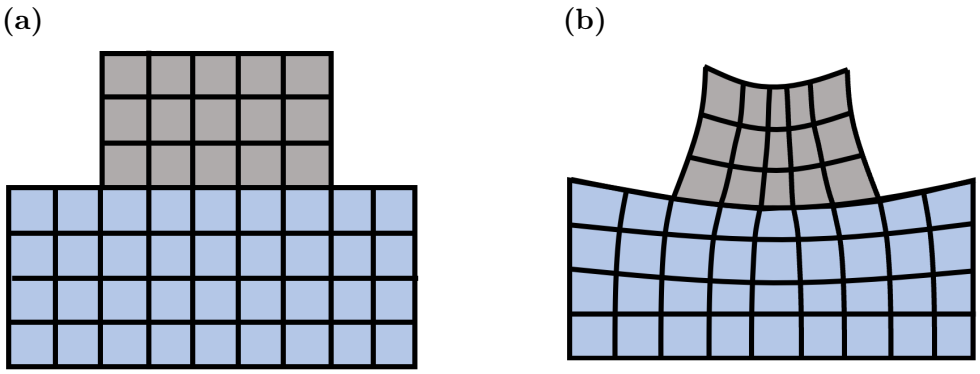

Figure 3.3: Metal gate (grey) on top of a SiGe substrate (blue) at **(a)** room temperature and **(b)** mK temperatures. Image adapted from [TZ15].

gate electrodes. The hole will generally experience greater biaxial strain when directly underneath the metal gates and increased shear strain when underneath the edges of the gates [LMM21, CRZ23].

Through Eqns. 3.34, a variable strain profile due to the gate electrodes becomes an avenue to influence the HH-LH mixing by adjusting the quantum dot's position along the in-plane direction inside the quantum well. When underneath a gate where the biaxial compression increases the diagonal elements of the strain tensor (Eqn. 3.31), the diagonal terms in the Luttinger-Kohn-Pikus-Bir Hamiltonian (P and Q) also increase. This pushes the LH band further away from the HH band, reducing the the admixture of the LH band in the ground state of the quantum dot. For a quantum dot that is near the edge of a gate, the shear (off-diagonal) terms of ε are greatest and the normal strain terms are relatively smaller. Both of these changes result in an increased admixture of LH states in the ground state. Returning to the discussion of Section 3.4, the greater influence of the LH bands will decrease $g_\perp$ and increase $g_\parallel$. I will rely on this argument in Chapter 6 to explain the variation of measured g-factors.

3.6 Modeling holes in a double quantum dot

The Luttinger-Kohn-Pikus-Bir Hamiltonian provides a great deal of insight into the ground state of a quantum dot for holes in germanium. With it, we can understand many physical characteristics of the hole states in a quantum dot from the properties of the uppermost valence bands. However, using this model becomes significantly more complicated when we begin to add multiple quantum dots, additional holes, and the requirement of the detailed knowledge of the potential landscape of each dot. A more practical approach approximates the problem by parameterizing the interactions between the various dot and hole states, generating a much simpler Hamiltonian. This is the motivation for using the Hubbard model to describe the system in Chapter 6 where two holes are trapped in two quantum dots.

3.6.1 The two-site Hubbard model

Consider the case of two quantum dots electrostatically defined in a Ge quantum well sandwiched between two SiGe layers. The hole occupations of both quantum dots are depleted down to the point where only two holes remain. Each hole can occupy the left (L) or right (R) dot, and the wave function overlap between these two states allows each hole to tunnel between dots. Furthermore, placing two holes on the same dot is associated with an energy cost due to the Coulomb interaction between these holes. Taking these factors into account, we can write down the Hubbard Hamiltonian as follows [WEC15]:

$$H_{\text{hub}} = t_c(c_L^\dagger c_R + c_R^\dagger c_L) - \sum_{i=L,R} \mu_i(n_{i\uparrow} + n_{i\downarrow}) + U n_{i\uparrow} n_{i\downarrow}. \tag{3.36}$$

Here, c_i is the two component spinor annihilation operator for holes on dot i, t_c is the tunnel coupling between each dot, μ_i is the chemical potential of dot i, $n_{i\sigma}$ is the number operator for spin σ on dot i, and U is repulsive intradot Coulomb interaction. The detuning ϵ is defined as the energy difference between the two dots, $\epsilon = \mu_R - \mu_L - U$, so that $\epsilon = 0$ corresponds to the charge transition $(0,2) \rightarrow (1,1)$, where (n,m) denotes the

number of holes in the left and right dots.

For the experiments I am interested in, the energy levels of the dots are adjusted from a small, negative detuning, where both hole are in the right dot (0,2), to small positive detunings, where each dot hosts one hole (1,1). At these detunings, there are five accessible spin states the system can be in. One is the singlet (0,2) state $|S_{02}\rangle$ and the other four are a part of the (1,1) charge configuration introduced in Section 1.5.2:

$$
\begin{aligned}
|S\rangle &= \frac{1}{\sqrt{2}}(|\uparrow\downarrow\rangle - |\downarrow\uparrow\rangle) \\
|T_-\rangle &= |\downarrow\downarrow\rangle \\
|T_0\rangle &= \frac{1}{\sqrt{2}}(|\uparrow\downarrow\rangle + |\downarrow\uparrow\rangle) \\
|T_+\rangle &= |\uparrow\uparrow\rangle
\end{aligned}
$$

The triplet states in the (0,2) charge configuration are neglected because they lie much higher in energy due to the strong exchange interaction between two holes occupying the same dot [JN06]. In this regime, the spin-conserving tunnel coupling t_c between the dots is typically the largest energy scale in the model [WEC15, MB21a], resulting in the hybridization between the two singlet states. This subspace of Eqn. 3.36 is [WEC15, MB21a, JMH22]

$$
H_S = \sqrt{2}t_c(|S_{11}\rangle\langle S_{02}| + |S_{02}\rangle\langle S_{11}|) + \epsilon|S_{02}\rangle\langle S_{02}|, \tag{3.37}
$$

which has the following hybridized eigenstates:

$$
|S_g\rangle = \cos\left(\frac{\Omega}{2}\right)|S_{11}\rangle - \sin\left(\frac{\Omega}{2}\right)|S_{02}\rangle \tag{3.38}
$$

$$
|S_e\rangle = \sin\left(\frac{\Omega}{2}\right)|S_{11}\rangle + \cos\left(\frac{\Omega}{2}\right)|S_{02}\rangle \tag{3.39}
$$

with ground and excited energies $E_{g,e} = \epsilon/2 \mp \sqrt{\epsilon^2/4 + 2t_c^2}$. The mixing angle between the charge states is equal to $\Omega = \arctan(2\sqrt{2}t_c/\epsilon)$. Transforming Eqn. 3.37 to the

hybridized $\{|S_e\rangle, |S_g\rangle\}$ basis gives

$$H_S = E_e|S_e\rangle\langle S_e| + E_g|S_g\rangle\langle S_g|. \tag{3.40}$$

3.6.2 Including Zeeman and spin-orbit interactions

To properly characterize the two hole system, we must supplement H_{hub} with two additional terms: one that includes the Zeeman interaction with an external magnetic field (H_z) and another to describe the spin-orbit interaction between spin states (H_{so}). The Zeeman Hamiltonian is given by the sum of the Zeeman contributions for the two dots [MB21a, JMH22]:

$$\begin{aligned} H_z &= \frac{\mu_B}{2}\left(\mathbf{g}^L \cdot \sigma^L \cdot \mathbf{B}^L + \mathbf{g}^R \cdot \sigma^R \cdot \mathbf{B}^R\right) \\ &= \frac{\mu_B}{2}\{B\cos\theta\left(g_\parallel^L \sigma_x^L + g_\parallel^R \sigma_x^R\right) + B\sin\theta\left(g_\perp^L \sigma_z^L + g_\perp^R \sigma_z^R\right)\} \\ &= \frac{\mu_B}{2}\left\{\frac{B\cos\theta}{2}\left(g_\parallel^+ \sigma_x^+ + g_\parallel^- \sigma_x^-\right) + \frac{B\sin\theta}{2}\left(g_\perp^+ \sigma_z^+ + g_\perp^- \sigma_z^-\right)\right\}, \end{aligned} \tag{3.41}$$

where I have assumed a global magnetic field in the x-z plane and a g-tensor where the in-plane components are equal, $\mathbf{g} = \text{diag}\{g_\parallel, g_\parallel, g_\perp\}$. Here, θ represents the angle of $\mathbf{B}$ from the x-y plane (i.e., $\theta = 90°$ is perpendicular to the substrate). For convenience, the final step shows the Zeeman Hamiltonian expressed in terms of the sum and difference between the left and right dot spins ($\sigma_i^\pm = \sigma_i^L \pm \sigma_i^R$) and g-factors ($g_i^\pm = g_i^L \pm g_i^R$):

As remarked on in Section 3.1, the spin-orbit interaction is a relativistic effect originating from the effective magnetic field a hole experiences when moving through the electric field of its confining potential. Consider the simple case of an electric field oriented along the z axis that presses the hole wave function against the upper surface of the Ge quantum well, $\mathbf{E} = E_0\hat{z}$. The hole moving with velocity $\mathbf{v}$ will experience an effective magnetic field equal to $\mathbf{B}_{\text{eff}} = -(\mathbf{v} \times \mathbf{E})/c^2$. Including this into the Zeeman interaction

leads to a spin-orbit contribution to the Hamiltonian:

$$H_{so} = \frac{\mu_B}{2} g\sigma \cdot \mathbf{B}_{\text{eff}} = -\frac{g\mu_B}{2c^2}\sigma \cdot (\mathbf{v} \times \mathbf{E}). \tag{3.42}$$

This interaction of the charge carrier with $E_0\hat{z}$ at the interface of the quantum well is known as Rashba spin-orbit coupling. For the HH bands in Ge, this term is proportional to the cube of the in-plane wave vectors [WCP08, NKK12, MSH14, MB21b, Win03]:

$$H_{so} = i\lambda_R(k_-^3\sigma_+ - k_+^3\sigma_-), \tag{3.43}$$

where $k_\pm = k_x \pm ik_y$, $\sigma_\pm = 1/2(\sigma_x \pm i\sigma_y)$, and λ_R is the strength of this Rashba interaction. As the name spin-orbit suggests, this interaction couples orbital states with different spins. For the purposes of this Hubbard-like model, it can be parameterized by a spin-orbit vector $\mathbf{t}_{so} = (t_x, t_y, 0)$ that couples $|S_{02}\rangle$ to the polarized (1,1) triplet states $|T_\pm\rangle$ [DN09, MB21b, JMH22]:

$$H_{so} = -\sum_{\pm}(t_x \pm it_y)|T_\pm\rangle\langle S_{02}| + \text{H.c.} \tag{3.44}$$

Combining Eqns. 3.40, 3.41, and 3.44, we arrive at the full Hamiltonian in matrix form in the basis $\{|S_g\rangle, |T_+\rangle, |T_0\rangle, |T_-\rangle\}$ [MB21b, JMH22]:

$$H = \begin{pmatrix} \frac{\epsilon}{2} - \sqrt{\frac{\epsilon^2}{4} + 2t_c^2} & t_{so}\sin\left(\frac{\Omega}{2}\right) - \frac{g_\parallel^- \mu_B B\cos\theta}{2\sqrt{2}}\cos\left(\frac{\Omega}{2}\right) & \frac{g_\perp^- \mu_B B\sin\theta}{2}\cos\left(\frac{\Omega}{2}\right) & t_{so}^*\sin\left(\frac{\Omega}{2}\right) + \frac{g_\parallel^- \mu_B B\cos\theta}{2\sqrt{2}}\cos\left(\frac{\Omega}{2}\right) \\ t_{so}^*\sin\left(\frac{\Omega}{2}\right) - \frac{g_\parallel^- \mu_B B\cos\theta}{2\sqrt{2}}\cos\left(\frac{\Omega}{2}\right) & \frac{g_\perp^+ \mu_B B\sin\theta}{2} & \frac{g_\parallel^+ \mu_B B\cos\theta}{2\sqrt{2}} & 0 \\ \frac{g_\perp^- \mu_B B\sin\theta}{2}\cos\left(\frac{\Omega}{2}\right) & \frac{g_\parallel^+ \mu_B B\cos\theta}{2\sqrt{2}} & 0 & \frac{g_\parallel^+ \mu_B B\cos\theta}{2\sqrt{2}} \\ t_{so}\sin\left(\frac{\Omega}{2}\right) + \frac{g_\parallel^- \mu_B B\cos\theta}{2\sqrt{2}}\cos\left(\frac{\Omega}{2}\right) & 0 & \frac{g_\parallel^+ \mu_B B\cos\theta}{2\sqrt{2}} & -\frac{g_\perp^+ \mu_B B\sin\theta}{2} \end{pmatrix}, \tag{3.45}$$

where $t_{so} = t_y + it_x$ For simplicity, I neglect the excited singlet orbital state $|S_e\rangle$, as it lies high enough in energy to be safely ignored for typical experiments. For brevity, I will also begin removing the subscript for the ground singlet state: $|S_g\rangle \to |S\rangle$. The eigenenergies of these states (including the excited singlet) are plotted as a function of

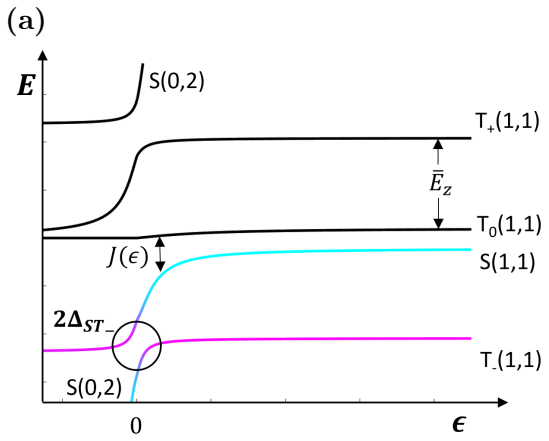

Figure 3.4: **(a)** Eigenenergies for the singlet and triplet states in Eqn. 3.45.

detuning ϵ in Fig. 3.4a.

From this Hamiltonian and dispersion plot, it is clear there are several spin states one must consider when attempting to encode a qubit into two states of this system. To benefit from properties of spin encoding discussed in Section 1.5.2, one needs to utilize the subspace of the singlet state and one of the triplet states. Since $|T_+\rangle$ lies the highest in energy, it is generally difficult to populate this state without significant leakage into the lower states, reducing the choice of triplet state to $|T_0\rangle$ or $|T_-\rangle$. The correct choice depends on which state one can access and perform coherent operations the longest. To complicate the matter further, the answer to this question relies on all of the parameters we have discussed in this section. Changing the orientation of the magnetic field, spin-orbit coupling, or HH-LH splitting through the dot position all have an effect on which states can be used for the most optimal qubit.

For example, looking at the off-diagonal elements in the Hamiltonian connecting $|S\rangle$ and $|T_-\rangle$, one can see the coupling between these states depends on the orientation of the magnetic field. Because of this coupling, these two states form an anticrossing, where the size of this gap is labeled Δ_{ST_-} in Fig. 3.4a. Consequently, it is possible to adjust the size of the $S - T_-$ anticrossing gap by rotating the direction of $\mathbf{B}$. A smaller anticrossing makes it difficult to access the T_- state, but is ideal for $S - T_0$ encodings.

Once again, I would like to stress that although this model does not explicitly justify the origins of the various interactions included, one can still rely on energy band models to explain the behavior of the Hubbard model's parameters. The advantage of using this model is the speed at which one can solve for the eigenenergies and eigenstates, allowing one to easily fit the Hamiltonian parameters using measured probabilities in experiment.

3.6.3 $S - T_-$ subspace

In Chapter 6, I discuss experimental evidence for encoding the qubit using $|S\rangle$ and $|T_-\rangle$. Therefore, I would like to introduce the subspace spanned by these two states (colored blue and magenta in Fig. 3.4a). Projecting Eqn. 3.45 onto this logical basis $\{|S\rangle, |T_-\rangle\}$ results in the effective Hamiltonian [MB21b]:

$$H_{ST_-} = \begin{pmatrix} -J(\epsilon) & \Delta \\ \Delta & -\overline{E}_z \end{pmatrix}. \tag{3.46}$$

I define the exchange energy $J(\epsilon) = -\frac{\epsilon}{2} + \sqrt{\frac{\epsilon^2}{4} + 2t_c^2}$ as the energy difference between $|S\rangle$ and $|T_0\rangle$. The coupling of the $S - T_-$ states (Δ) emerges from two sources: (1) a spin-orbit splitting (Δ_{so}) and (2) an effective Zeeman splitting due to the anisotropy of the g-tensors (g_a) that is only present when B has non-zero in- and out-of-plane components [JMH22, MB21b]:

$$\Delta = \left| \Delta_{so} \sin\left(\frac{\Omega}{2}\right) + g_a \mu_B B \cos\left(\frac{\Omega}{2}\right) \right|, \tag{3.47}$$

$$\Delta_{so} = t_y - i t_x \frac{g_\perp^+ \sin\theta}{\sqrt{(g_\parallel^+ \cos\theta)^2 + (g_\perp^+ \sin\theta)^2}}, \tag{3.48}$$

$$g_a = \frac{1}{4\sqrt{2}} \frac{(g_\parallel^- g_\perp^+ - g_\parallel^+ g_\perp^-) \sin(2\theta)}{\sqrt{(g_\parallel^+ \cos\theta)^2 + (g_\perp^+ \sin\theta)^2}}. \tag{3.49}$$

Additionally, $\overline{E}_z$ is the average Zeeman splitting that separates $|T_-\rangle$ from $|T_0\rangle$, $\overline{E}_z = \overline{g}\mu_B B$, where $\overline{g}$ is the average g-factor of the two dots projected onto the axis of $\mathbf{B}$.

Chapter 6 explores a system where I use this Hamiltonian to describe coherent oscillations between spin states in a Ge quantum dot. Consequently, I will leave explaining the details of using this $S - T_-$ subspace for qubit manipulation until then.

CHAPTER 4

Device Fabrication and Experimental Setup

As introduced in Fig. 1.3, the goals of our devices are to generate a two-dimensional electron or hole gas, deplete this 2d layer in specific patterns to isolate two quantum dots, and manipulate the energy levels of these dots to trap and control two particles for qubit operation. This chapter focuses on the fabrication procedure used to create these devices and the equipment needed to achieve this precise control.

4.1 Fabrication

Fabricating devices for quantum dots is a strenuous yet rewarding journey. Because the resolution and spacing requirements of gate electrodes reaches 50 nm at the device's center, it is paramount that the majority of fabrication steps are executed in a careful and consistent manner. Failure to adhere to guidelines will result in faulty or erratic devices that oftentimes cannot be diagnosed until tested below 4 K.

In the following, I will detail these methods that were built upon previous students in the lab [Sch17, Fre17, Pen20]. The early half of my research focused on trapping electrons in a Si/SiGe heterostructure, while the latter half utilized a Ge-rich Ge/SiGe heterostructure to isolate holes in DQDs. Because the fabrication steps for these two processes are almost identical, I will not separate them; however, I will note where they differ. I would also like to note that Joshua Schoenfield fabricated the device used on the Si wafer, while I made the device for the experiments on the Ge wafer. While the

following does not detail every fabrication parameter, I included a step-by-step guide in Appendix A that goes more in depth.

4.1.1 Germanium wafer structure and characterization

For all experiments regarding holes, measurements were performed on a Ge-rich heterostructure shown in Fig. 4.1b supplied by Giordano Scappucci and Menno Veldhorst from the QuTech and Kavli Institute of Nanoscience at Delft University of Technology. Beginning with a Si(001) base, the heterostructure consists of a 1.6 μm relaxed Ge layer; a 1 μm step graded $Si_{1-x}Ge_x$ layer with a final ratio of $x = 0.8$; a 500 nm relaxed $Si_{0.2}Ge_{0.8}$ buffer; the 16 nm wide compressively strained Ge quantum well; a 55 nm $Si_{0.2}Ge_{0.8}$ spacer layer; and finally a sacrificial Si cap (< 2 nm). The heterostructure is grown in an industrial reactor by reduced-pressure chemical vapor deposition [HLR21, LHL21].

To characterize the wafer, I designed (with helpful guidance from Hong-Wen Jiang) and fabricated a Hall bar on top of the heterostructure (see 4.1c). Ohmic contacts (blue) for the Hall bar were patterned with photolithography and metalized with 60 nm of Pt. A 100 nm Al_2O_3 insulating layer was grown with atomic layer deposition (ALD) before a 100 nm Al top gate (pink) was deposited. The device was then annealed for 1 hour at 420 C to repair oxide defects and draw the Pt into the quantum well. The Hall bar was tested at 4 K, and the transverse (R_{XY}) and longitudinal (R_{XX}) Hall resistances were measured in a magnetic field to calculate the wafer's mobility μ (Fig. 4.1c). R_{XX} was calculated from the resistance between contacts 4 and 5, while R_{XY} was the resistance between contacts 3 and 5. Although Fig. 4.1c demonstrates the onset of the quantum Hall effect through the visibility of Landau levels and Shubnikov-de Haas oscillations, the mobility is calculated within the region of vanishing magnetic field B, where the quantized behavior is not prominent.

The mobility characterizes how quickly charge travels through a semiconductor when pulled by an electric field [Kit05]. Generally, the larger μ is, the less defects and impurities are present in the semiconductor, making it a good measurement to compare the quality

of various substrates. Regarding Hall bar measurements, the mobility can be found from the electrical resistivity at zero magnetic flux ρ and carrier concentration n_{2D}:

$$\mu = \frac{1}{n_{2D}|e|\rho}, \tag{4.1}$$

where e is the charge of the electron. The charge density n_{2D} can be found from R_{XY} and resistivity ρ from R_{XX} for small magnetic fields [MHP15, Lak]:

$$R_{XY} = \frac{B}{n_{2D}|e|} \tag{4.2}$$

$$\rho = R_{XX}\frac{w}{d}. \tag{4.3}$$

Using the data in Fig. 4.1c and Eqns. 4.2 and 4.3, I found $\mu = 1.3 \times 10^5$ cm^2/V·s. I would like to note this is not the wafer's maximum mobility, as I did not measure μ for various top gate voltages. However, a similar wafer's mobility was measured in Ref. [SSH19] to be 5×10^5 cm^2/V·s.

4.1.2 Silicon wafer structure and characterization

All experiments characterizing and operating a qubit using the valley states of Silicon were performed on a wafer grown by Lisa Edge at HRL Laboratories and generously supplied to us by Jason Petta's lab at Princeton. While the details of this wafer's structure are confidential, the relevant characteristics are known and illustrated in Fig. 4.1a. Once again beginning with a Si substrate, a $Si_{1-x}Ge_x$ alloy graded buffer is grown, where the concentration x is varied from 0 up to typically 0.3 [HLL12, LHR13, PLK22]. This SiGe layer is followed by a 10 nm wide, strained Si quantum well, which is sandwiched by an additional $Si_{1-x}Ge_x$ layer. Finally, a thin, sacrificial Si cap completes the heterostructure. This wafer's mobility was characterized by Hong-Wen Jiang and Nick Penthorn through Hall bar measurements and found to be 7×10^5 cm^2/V·s [Pen20].

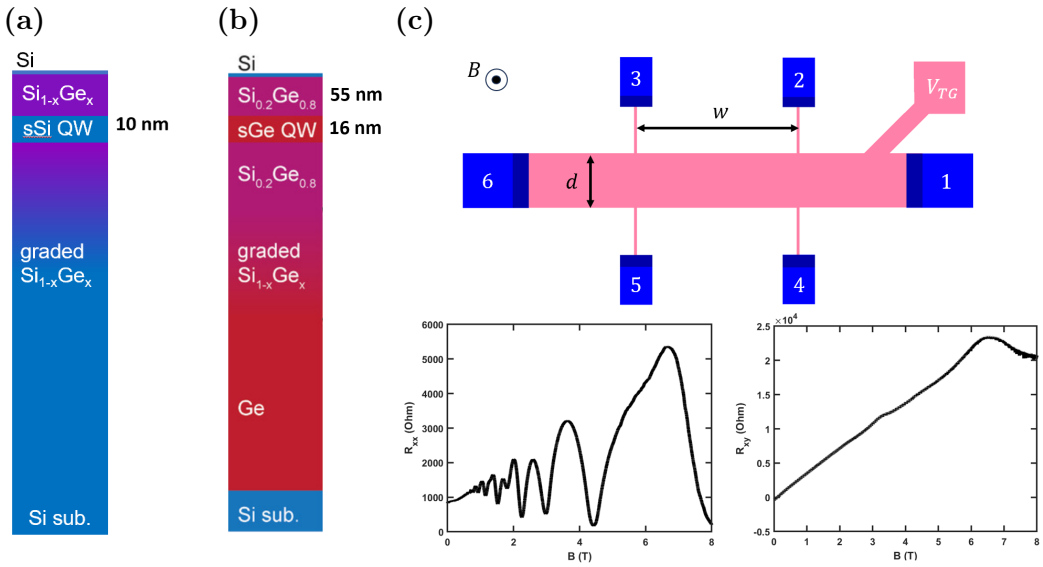

Figure 4.1: **(a)** Si quantum well wafer heterostructure. **(b)** Ge quantum well wafer heterostructure. Image adapted from [SSH19]. **(c)** Hall bar design used to character the heterostructure of (b). The ratio of w/d was 3/1. Longitudinal and transverse Hall resistances (lower panels) were measured to calculate $\mu = 1.3 \times 10^5$ cm^2/V·s.

4.1.3 Global alignment markers

Once the bare wafer is attained, one can begin fabricating the Ohmic contacts and gate electrodes that define the quantum dot device. Because the entire device cannot be fabricated in one step, it is important to first define a set of global markers that each fabrication step will be aligned to.

The pattern of the global alignment markers was first designed in KLayout and developed by Joe Zendejas into a photolithography mask by the UCLA Nanofabrication Laboratory (NanoLab). For all subsequent steps, the photolithography masks were produced in this same manner. A single layer of HMDS and photoresist (AZ 5214-E) was spun onto the wafer and exposed to UV light using this mask. After exposure, the wafer was developed in in a mixture of water and AZ 400K to removed the exposed resist. Finally, a 50 nm thermal evaporation of chrome using our lab's evaporator metalized these alignment markers. The remaining resist is then dissolved by letting the wafer sit

in acetone, leaving the Cr global markers only (Fig. 4.2a).

4.1.4 Ohmic regions

The device's source and drain reservoirs originate from doped regions that are conductive regardless of the top gate voltage. For the Si wafer, these regions are created with the implantation of phosphorous ions. Before being sent out for implanting, the Ohmic regions were first patterned with a double layer of photoresist and photolithography similar to the previous step. The unexposed photoresist serves as a protective shield when the entire wafer is bombarded by ions. The wafer was then sent out for ion implantation, which was performed by Leonard Kroko, Inc. with a beam energy of 25-30 KeV and dosage of 2×10^{15} cm^{-2}. The resist is then stripped off in acetone, and the wafer is placed in a rapid thermal annealer at NanoLab for 15 s at 700 °C. This annealing step repairs the crystal structure that was damaged by the ion beam, ensuring good conductivity.

For the Ge wafer, the Ohmic regions are created in a different manner. Instead of ion implantation after photolithography, I used the CHA e-beam evaporator at NanoLab to deposit 60 nm of Pt. Immediately before evaporation, the wafer was dipped in Buffered Oxide Etch (diluted HF acid) to etch the Si capping layer. This step ensures the deposited Pt will make good contact with the underlying SiGe layer. Once the resist is removed, the wafer was annealed for 1 hour at 420 °C. Similar to before, this annealing step creates the Pt-SiGe alloy that serves as the source of holes. The final result after this step is shown in Fig. 4.2b.

4.1.5 Outer gates

Similar to the global alignment marker step, the outer gate electrodes were patterned with photolithography. After this step, 5/45 nm of Ti/Au was deposited onto the wafer using the CHA e-beam evaporator at NanoLab (see Fig. 4.2c). The first 5 nm of titanium serves as a buffer layer that will bond well to the Si substrate and subsequent gold. Gold is preferred over Ti due to its increased conductivity. Using the e-beam evaporator is

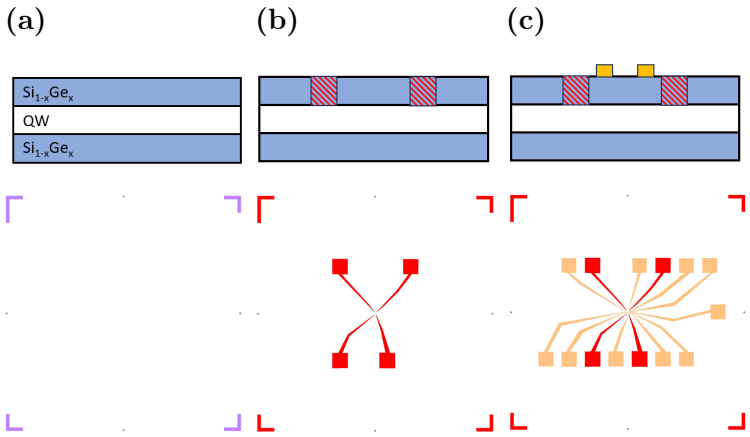

Figure 4.2: Beginning fabrication steps. **(a)** Cr global alignment markers. **(b)** Ohmic regions defined by ion implantation or Pt. **(c)** Outer gate Ti/Au electrodes. Top panels represent wafer cross-sections. Bottom panels illustrate photolithography masks used for patterning.

especially important in this and the following step because of its ability to create a high quality metallic film. This pattern does not extend all the way to the device's center because the resolution requirement of 50 nm is not possible with usual means of photolithography. Consequently, the outer gate pattern terminates when the width of the electrodes reaches ~ 3 μm.

4.1.6 Inner gates

To fabricate the inner leads of the device's depletion gates, electron-beam lithography (EBL) must be used to reach the nm resolution required for quantum dot confinement. Whereas photolithography uses UV light to expose specific patterns of resist, EBL traces out the pattern using a beam of electrons. For the Si wafer, EBL was carried out on our lab's Hitachi scanning electron microscope (SEM) with the Nanometer Pattern Generation System (NPGS) software. This software requires the user to fine-tune the beam parameters and manually find the alignment markers for each device, which leads to a large amount of variation from device to device.

For the Ge wafer, we decided to utilize NanoLab's Vistec EBPG 5000+ES tool, which

automatically calibrates the e-beam and locates alignment markers. With this machine, there is almost no device variation. A second advantage of Vistec is the speed that it can perform the exposure. Because it costs little operating time, I opted to skip the previous step and write both the inner and outer gates simultaneously with Vistec.

After developing the e-beam exposed resist, the pattern is metalized using NanoLab's CHA e-beam evaporator. Again, 5/45 nm of Ti/Au was deposited to form the electrodes. Fig. 4.3a illustrates the result. Combined with the outer gates, these electrodes function to deplete the 2d electron or hole gas into two islands that form the quantum dots.

4.1.7 Atomic layer deposition

Before patterning the top accumulation gate, a 100 nm layer of Al_2O_3 is first grown using our lab's Savannah through a process known as atomic layer deposition (ALD). ALD offers the user a high degree of control over the thickness of the oxide, as 1 Å is grown every cycle of the process. This oxide electrically isolates the gold depletion gates fabricated in the previous two steps with the top gate in the following step.

4.1.8 Top gate

To generate the 2d electron or hole gas, a voltage is applied to a global accumulation gate that overlaps with the device center and Ohmic contacts (pictured in gray in Fig. 4.3b). Because the top gate spans several microns at its point of highest resolution, photolithography is used to define the pattern. Metallization can either be done in a thermal or e-beam evaporator to deposit 100 nm of aluminium, as the top gate's features are large enough that either method works. The aluminium oxide layer with the top gate metallized is depicted in Fig. 4.3b.

4.1.9 Etched contact windows

After the top gate is fabricated, windows are etched into the Al_2O_3 layer to allow electrical contact to the depletion gates and Ohmic regions via wire bonds. Wire bond contact

windows are first defined in photoresist using photolithography. The wafer is then briefly submerged in a phosphoric acid agent (Transetch-N) that selectively attacks aluminium oxide. Once the oxide in the exposed regions is completely etched away (blue squares in Fig. 4.3c), wire bonds can make electrical contact with each gate.

4.1.10 Mounting and electrical contacts

The final fabrication step involves mounting individual devices onto a printed circuit board (PCB) and wire bonding between the PCB and device contacts. Devices are cleaved from the wafer using either a diamond scribe or an LPKF ProtoLaser. For thin wafers, a diamond scribe is sufficient to break off devices. However, for thicker wafers, it is beneficial to instead use a dicing tool. Each device is then either super-glued or attached via silver epoxy to the PCB. Super glue was used for short tests, while silver epoxy ensured the device remained on the PCB for longer experiments and multiple cooldowns. Once the device is mounted onto a PCB, a dab of indium was placed with a low-powered soldering iron onto the Ohmic contacts for the the ion-implanted Si wafer. This indium was needed in order to make good electrical contact between the implanted ions and wire bond. Wire bonds from the PCB to the device are made with a West Bond Model 7400C Wire Bonder, after which the device is ready for low temperature testing.

4.2 Cryogenic setup

All quantum dot qubits of today must be operated at cryogenic temperatures. When thermal fluctuations in the device are comparable to the spacing between the qubit's energy levels, the environment will have a high probability to populate excited states, destroying any qubit coherence. The energy required to place additional charge onto a quantum dot is on the order of 1 meV. This translates to needing an operating temperature well below $T = E/k_B \approx 10$ K to detect charge transitions on and off a dot, where k_B is Boltzmann's constant. This operating point is further limited by the energy spacing between qubit states. For example, for the qubit described in Chapter 5, the

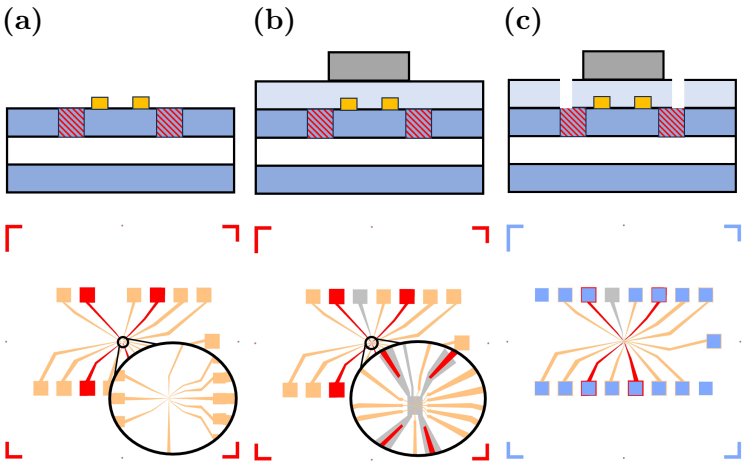

Figure 4.3: Final fabrication steps. **(a)** Inner gate Ti/Au electrodes. **(b)** ALD grown AL_2O_3 and Al top gate. **(c)** Etched contact windows through the oxide. Top panels represent wafer cross-sections. Bottom panels illustrate the EBL pattern (a) or photolithography masks (b and c) used for patterning.

energy difference between $|0\rangle$ and $|1\rangle$ is ~ 20 μeV, which requires a device temperature well below 230 mK. To this end, basic device screening was performed at 4 K, and all qubit experiments were made in a dilution refrigerator with a base temperature of 40 mK.

4.2.1 Device screening at 4 K

Due to the limited capacity and time required to cool down a dilution refrigerator, we often screened devices at liquid helium (LHe) temperature (4.2 K) prior to loading it inside a dilution refrigerator. At 4 K, we can ensure a device is working properly and avoid the time and effort required to cool it down to mK temperatures if it misbehaves.

The device is first placed in a probe that can be lowered into a LHe dewar. Once the probe is submerged in LHe, a voltage is applied to the top gate to generate the 2d electron or hole gas underneath it and a current will develop across two Ohmic contacts. If no current is measured for high top gate voltages, there is a problem with the device's Ohmic regions: either the wire bonds do not have good electrical contact with the Ohmic

regions or the annealing step did not repair the crystal structure or even altered the heterostructure.

Assuming current can be measured between Ohmic contacts at appropriate top gate voltages, the depletion gates can then be tested. This test is done by attempting to deplete the current by applying a voltage to the gate electrodes. In the case of electrons flowing between contacts, this voltage is negative, while pinching off a current of holes requires a positive gate biases. When a single gate has no effect on the 2DEG (or 2DHG), there is likely a break in the electrode resulting in no voltage being applied to the innermost end.

If all depletion gates have some ability to decrease the current induced by the top gate, the device is considered sufficient for mK experiments. The greatest benefit of this screening is that it only takes 1-2 hours compared to the 3-4 days needed for our dilution refrigerator. This screening can also be performed while experiments are ongoing in our dilution refrigerator.

4.2.2 Oxford Triton-200 dry dilution refrigerator

The Triton dilution refrigerator was used for the low temperature experiments discussed in Chapters 5 and 6, where its inner workings are pictured in Fig. 4.4a. Because it is a dry fridge, it does not require a dewar of LHe to cool, as the ^{3}He/^{4}He mixture it relies on is circulated in a closed-loop system. Like all dilution fridges, it exploits a phase transition between ^{3}He and ^{4}He that exists down to 0 K [BT]. At mK temperatures, a ^{3}He/^{4}He mixture will separate into two phases: an almost pure ^{3}He phase (the concentrated phase) and a ^{4}He-rich phase consisting of 6.4% ^{3}He (the dilute phase). Due to its lighter mass, the concentrated phase rests on top of the dilute phase. As ^{3}He is pumped out of the bottom, dilute phase, it is replenished by the ^{3}He atoms in the pure phase resting above. This transition from the concentrated to dilute phase costs energy, which is taken from the environment, and subsequently lowers the temperature of the fridge.

Currently, 104 DC lines and 14 semi-rigid cables for HF signals run from the top

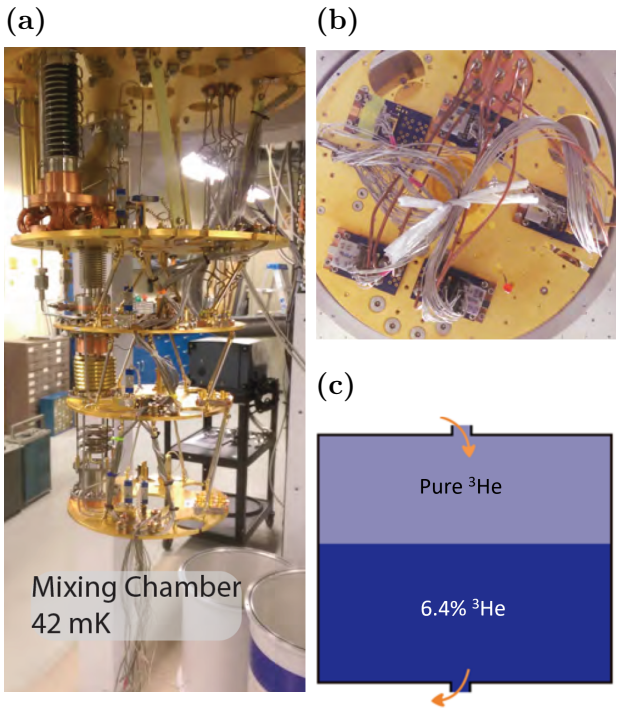

Figure 4.4: **(a)** The inner skeleton that composes the Triton-200 dilution refrigerator. The mixing chamber is located on the lowest plate, which has a base temperature of 40 mK. **(b)** A view from underneath the mixing chamber plate. Several PCBs can be seen mounted. Both images adapted from [Sch17]. **(c)** Dilution process removing atoms of ^{3}He from the diluted phase. As the ^{3}He is replenished from the concentrated phase, energy is taken from the environment. Image adapted from [BT]

of the fridge down to the mixing chamber plate seen in Fig 4.4b, permitting six double quantum dot devices to be tested simultaneously. It typically takes a day to unload and load a new batch into the fridge, and another day to cool the mixing chamber plate down to the fridge's base temperature.

4.2.3 Sample holder

For quick screenings in LHe, we often mounted devices onto a simple 16-pin ceramic chip carrier (see Fig. 4.5b). Although this board does not support high-frequency (HF) signals due to cross-talk and attenuation issues, it allows us to quickly screen devices with

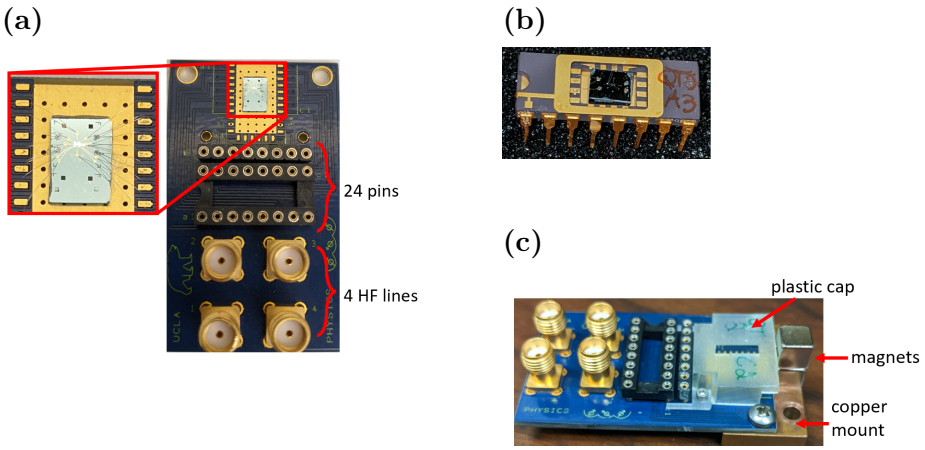

Figure 4.5: Two device carriers used for screening and testing. **(a)** PCB designed by Blake Freeman with a device mounted at the top. There are 24 DC pins and 4 HF lines. Inset: wire bonds connecting the device and PCB pins are visible. **(b)** A 16-pin ceramic device carrier. **(c)** For spin measurements, a block magnet was mounted at the edge of the PCB.

DC voltages. The standard socket makes plugging the carrier into a probe exceptionally easy.

The second type of carrier used was a custom-made PCB developed by Blake Freeman shown in Fig. 4.5a. This PCB consists of four layers: two for 24 DC wires, one for 4 HF lines, and a grounding layer separating the two. The 24 DC pins can be accessed with standard 8-pin sips, while the four HF pins socket into SMA adaptors. The device is mounted onto a rectangular copper pad plated with gold. All wires are routed to the edges of this rectangle to allow for short wire bonding lengths.

Before this PCB is mounted into our dilution refrigerator, a 3d-printed plastic cap is attached to protect the wire bonds underneath (see 4.5c). A copper mount is attached to the bottom of the board to ensure good thermal contact between the mixing chamber plate in the dilution fridge and PCB. For the spin experiments discussed in Chapter 6, two block magnets were mounted onto the copper mount at the edge of the PCB, generating a global field of ~ 4 mT at the device's center.

4.2.4 Electron temperature

While the mixing chamber in our dilution refrigerator may reach 40 mK, this is not the temperature of the charge carriers in the device. The electron (or hole) temperature T_e is both a function of the fridge temperature T_f and additional inelastic processes originating from noise and interference of the measurement environment (which I will call parasitic heat) [MSB13].

Unfortunately, as the temperature of the charge carriers falls, so does their thermal coupling to the phonons in the substrate's lattice, generating a mismatch between the temperature of the charge carriers and the substrate. Consequently, T_e becomes independent of T_f once the fridge is cold enough, as the source of parasitic heat can no longer be overcome by the cooling power delivered to the charge carriers. The main countermeasures against parasitic heat include proper thermal anchoring of wires, the elimination of ground loops, mounting passive electrical components (e.g, bias tees and attenuators) inside the fridge, and microwave filtering [JSP20]. After implementing many of these remedies, our group has measured the electron temperature in our devices to be a few hundred mK [SFJ17, Fre17, PSR19].

4.3 Electrical control

4.3.1 Current measurements

The primary means our lab has of detecting charge flowing into, out of, and between quantum dots is by monitoring the shifts of a nearby source-drain current as the electron or hole occupation on a dot changes. This nearby current channel is operated as a quantum point contact (QPC) or single electron transistor (SET), and its shifts are on the order of several picoamps. For DC measurements, a Stanford Research Systems (SRS) 570 current preamplifier or LCA-20K-200M low-noise current amplifier was used to amplify the current before measurement with a Keithley 2000 series digital multimeter. At the cost of a factor of 5 in gain, the LCA-20K-200M has a greater bandwidth at

20 KHz compared to the SRS 570's 200 Hz, making it the better option for real-time measurements.

Using only the DC current to detect charge transitions in a neighboring quantum dot is often insufficient due to the electrical noise present in our system. Current fluctuations from this noise are often the same order of magnitude as the current response to a single electron or hole moving through the quantum dot. To counteract this noise, we utilize the homodyne measurement performed by an SRS SR830 Lock-in amplifier. The Lock-in generates an output voltage $\Delta V \sin(\omega t)$ at at a reference frequency ω, where we set ΔV to be 1 mV. This signal is superimposed onto the plungers' DC biases using an SRS SIM980 summing amplifier.

We then feed in the QPC/SET current into the Lock-in, where it isolates the portion of the signal oscillating at the same frequency of the Lock-in reference frequency ω. All extraneous contributions to the current, including noise, that do not oscillate at ω are thrown out by the Lock-in. Because the reference signal applied to the device's plungers (which control the charge occupation of the dots) oscillates at ω, charge transitions occur at this frequency, leading these events to be highlighted by Lock-in while the effects of noise are dampened.

4.3.2 DC biases

Every quantum dot gate electrode requires its own DC bias, meaning ~ 11 DC biases are required per double quantum dot device. We supplied these biases using two instruments. The first was with the auxiliary (AUX) outputs of a SR830 Lock-in. Each SR830 comes with four AUX outputs that can be set remotely through a GPIB connection. In addition to the lock-in, DC biases were also controlled with a BS-16 precision voltage source from Stahl Electronics. Each Stahl voltage source hosts 16 outputs with 16-bit resolution, making it an ideal instrument to handle all of the DC biases for a quantum dot device.

A BNC cable connects the voltage output to a breakout box at the top of our dilution refrigerator. From the breakout box's center pins, stainless steel mini coaxial cables from

Cooner Wire travel down the length of the fridge to sips that plug into the device PCB. This wire is anchored to each temperature stage of the fridge to reduce heat exchange. Stainless steel is ideal for this connection due to its poor thermal conductivity, which mitigates the heat traveling from the room temperature lock-in to the mK cooled device.

4.3.3 Arbitrary voltage waveforms

For many qubit experiments, a complicated set of pulses need to be applied to multiple gate electrodes to manipulate the charge on the quantum dots. An arbitrary waveform generator (AWG) has the freedom to create these pulses at the cost of slower rise times and smaller sampling rates. For the experiments in Chapter 6, a Tektronics AWG 520 generated all pulses applied to the device's plunger gates. This AWG has two channels that can be independently programmed with a sampling rate of 1 GHz. The temporal resolution is therefore limited to 1 ns; however, this is not too limiting for singlet-triplet qubits with operation times of 20-100 ns. Another important aspect of the AWG is the ability to output a programmable trigger at any point in the pulse sequence. This trigger was used to externally modulate the lock-in frequency, syncing the Lock-in's current measurement to specific sections of the pulse.

4.3.4 Fast gate pulses

For the qubit experiments in Chapter 5, where operation times between the valley states occur at 4.5 GHz, the 1 GHz sampling rate of the AWG is not sufficient to precisely control evolution. In these situations, we opted to use short square pulses originating from an Agilent 81134A Pulse Pattern generator, which has ps resolution and a rise time as short as 60 ps. This short rise time plays a critical role in Chapter 5, as it induces the non-adiabatic transitions between valley states we rely on for the initialization of a mixed valley state. Although the slowest repetition rate for these pulses was 15 MHz, we often operated the Agilent in its "data mode," where the effective pulse rate is lowered by modifying the binary data string defining pulse cycles. Data mode also permits us to

modulate the repetition rate in a way where the pulse is on for a number of cycles and then off the for the same number of cycles. If the Lock-in's reference frequency is set to this rate, the Lock-in will isolate the pulse generator's effects on the quantum dots and remove any background signals.

CHAPTER 5

Two-axis quantum control of a fast valley qubit in silicon

As discussed in Chapter 2, the low-lying valley states in silicon greatly affect electron physics in silicon-based heterostructures. In the case of Si/SiGe quantum dots, the energy splitting between out-of-plane valley states can be suppressed in the presence of disorder at the Si/SiGe interface [Sch97, FEC06, FCT07, CHD10]. For electron charge- and spin-based qubit implementations, an excited valley state that is nearly degenerate with the ground state presents an unwanted avenue for quantum information loss [GSF07, YRR13, ZLS13].

On the other hand, the valley states have properties that can be exploited to form a qubit basis with several desirable traits. First, such a valley qubit can be electrically manipulated and measured through valley-orbit coupling with no need for a magnetic field gradient [FC10, GEC13, VRY15]. Second, since there exists a broad window of quantum dot gate voltages that do not impact the valley splitting, a valley-encoded qubit would have protection against charge noise, the leading source of decoherence in charge and spin qubits [CSK12, MKP18]. Finally, gate operation times are determined by the valley splitting, which can be on the order of 10 GHz [SFJ17, MPB17].

In 2017, our group demonstrated electrical manipulation and charge-based readout of the valley states in a Si/SiGe heterostructure [SFJ17]. We further advanced this idea in 2019 when we established two-axis control over a qubit defined with these valley states,

allowing us to explore the advantages outlined above [PSR19]. This chapter focuses on this recent work, beginning with mapping out the surface of the Bloch sphere and concluding with a discussion on the fidelities of this qubit.

5.1 Few electron regime

A scanning electron micrograph (SEM) of the device prior to the top gate fabrication is pictured in Fig. 5.1a. The five depletion gates in the lower channel define the two quantum dots (dotted circles). The barrier gates are labeled B_L, M, and B_R and control the tunneling between the dot and reservoirs and between the dots themselves. The interdot coupling is controlled by barrier gate M. The middle gates labeled V_L and V_R are the plungers, which we used to control the left and right dot energy levels respectively. Before operation, the device was cooled inside our dilution refrigerator with a base temperature of 36 mK.

The charge occupation of both dots is measured through monitoring of the nearby current flowing through the upper channel of the device. Defined by the three top electrodes and pictured as a large dotted circle, a large quantum dot is formed that acts as a single electron transistor (SET). Peaks in the transconductance of the current through the SET correspond to electrons hopping in or out of either dot, and the sign of each peak indicates whether or not the charge transition occurred in the left dot (positive) or the right dot (negative).

By applying appropriate voltages to the five lower electrodes, we tune the device into a regime where there are only two electrons present on the double dot. We focused on the (1,1)-(2,1) charge transition as the qubit operation point; in other words, there is one electron in the left dot and a second is allowed to tunnel between dots (Fig. 5.1b). This transition yielded the best operation, although valley oscillations were also seen at the (1,0)-(0,1) transition in earlier work from our lab [SFJ17]. Because we observed oscillations between valley states for both dots (Fig. 5.1c and 5.1d), we determined this stationary electron did not significantly impact the valley physics. With one electron

free to tunnel between the dots, we can apply the theory discussed in Chapter 2. In the following, I will label the ground and excited valley states for the left and right dots as $|L_{v1}\rangle, |L_{v2}\rangle, |R_{v1}\rangle, |R_{v2}\rangle$.

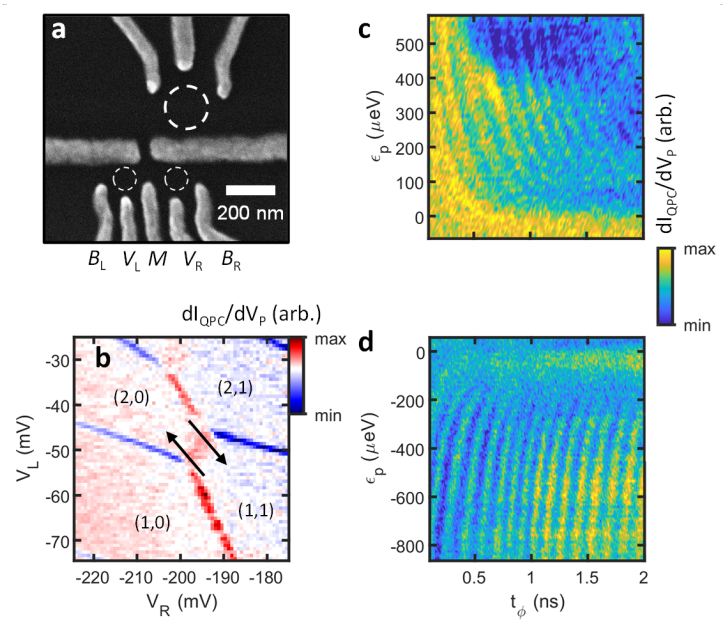

Figure 5.1: Device structure and coherent valley oscillations. **(a)** SEM of the double QD device used in this study, before deposition of the top gate. **(b)** Charge stability diagram as a function of plunger voltages, measured by QPC transconductance, in the operation region. Indices (i,j) indicate electron occupation in the left and right dots. Arrows represent the general starting points and pulse directions used to drive valley precession. **(c)** Oscillations of 5.5 GHz between left dot valley states when pulsing from (1,1) to (2,0). **(d)** Oscillations of 7.8 GHz between right dot valley states when pulsing from (2,0) to (1,1).

5.2 Operation mechanism

To observe coherent valley oscillations in the left dot, the system is initialized in the (1,1) charge configuration corresponding to the right dot ground state $|R_{v1}\rangle$. Then a trapezoidal voltage pulse with ~200 ps rise time is applied simultaneously to V_L and V_R (with opposite polarities) to modify the system detuning $\epsilon = V_R - V_L$, or the relative energy

of the two quantum dots. The ramp rate is slow enough that there are no transitions to excited states for all detunings $\epsilon < 0$. As the detuning is increased to positive values, there is an anticrossing between the lowest two levels at $\epsilon \approx 0$ (see Fig. 2.3b or Fig. 5.2c). Here, the state experiences a Landau-Zener transition into a superposition of all four states, with state coefficients determined by the pulse ramp rate [PLG10].

The transition from the $|R_{v1}\rangle$ ground state to the excited states as the system passes through the anticrossing is governed through the Landau-Zener equation:

$$P_{LZ} = \exp\left(\frac{-2\pi\Delta^2}{2\hbar v}\right), \tag{5.1}$$

where v is the effective speed at which the system passes through the anticrossing at $\epsilon = \epsilon_*$:

$$v = \left|\frac{d(E_2 - E_1)}{dt}\right|_{\epsilon_*} = \left|\frac{d(E_2 - E_1)}{d\epsilon}\right|_{\epsilon_*} \frac{\epsilon_p}{t_{\text{ramp}}}.$$

Here, E_1 and E_2 are the diagonal elements of the Hamiltonian for these two states forming the anticrossing, Δ is the coupling between these two states, and ϵ_p is the ramp height. As we adjust the ramp time or height, we therefore influence the probability P_{LZ} that the initialized $|R_{v1}\rangle$ remains in $|R_{v1}\rangle$ or transitions to one of the states involved at the anticrossing (1-P_{LZ}). If the pulse is sudden enough with respect to Δ, the system will remain in the initialized state $|R_{v1}\rangle$. In the opposite limit for gradual pulses, the $|R_{v1}\rangle$ will adiabatically evolve to $|L_{v1}\rangle$ as the system is pulsed to large positive detunings. In this experiment, we relied on the pulse being between these two regimes to generate a relatively even mixture of the two eigenstates at the anticrossing.

Due to valley-orbit coupling, the state evolves smoothly into a superposition of the two left dot valleys $|\psi\rangle = \frac{1}{\sqrt{2}}\left(|L_{v1}\rangle + e^{i\phi}|L_{v2}\rangle\right)$ as the detuning is further increased. When the pulse reaches its maximum detuning and remains idle, the state undergoes Larmor precession between the left dot valley states with a frequency determined by the left dot valley splitting $E_{VS,L}$. Here is the reason for needing an even mixture of the valley states from the Landau-Zener transition. If the initial state evolved completely into an

eigenstate, there would be no Larmor precession. The more even the final mixed state is, the closer $|\psi\rangle$ is to the equator of the Bloch sphere and the greater the visibility of the precession becomes.

5.3 Readout mechanism

After the state precesses around the Bloch sphere at positive detuning for an operation time t_ϕ, the qubit accumulates a valley state phase difference $\phi = \phi_0 + \frac{E_{VS,L}}{\hbar}t$ determined by the left dot's valley splitting. To read out this phase difference, a method is needed that distinguishes the two valley states $|L_{v1}\rangle$ and $|L_{v2}\rangle$. We accomplished this task by evolving $|\psi\rangle$ once again through a Landau-Zener transition at the anticrossing near $\epsilon = 0$. This transition maps $|L_{v1}\rangle \rightarrow |R\rangle$ and $|L_{v2}\rangle \rightarrow |L\rangle$. After projecting to the charge states, the nearby SET can now determine the valley composition that was present at the end of the operation.

5.4 Coherent valley oscillations

The measured current oscillations as a result of the operation time t_ϕ, averaged over roughly 5×10^6 pulse realizations for each pulse width, reflect a changing ϕ between valley states (Fig. 5.1c). This pulse technique is also used to probe the right dot valley states by initializing in the left dot and pulsing to negative detuning (Fig. 5.1d). The amplitude of these oscillations can be modeled by a decaying sinusoid, as the phase between the valley states is projected to the probability of finding the electron on L or R dot:

$$P(t) = \frac{1}{2}\left[1 + e^{-(t/T_2^*)^\alpha}\cos\left(\frac{E_{VS}}{\hbar}t + \phi_0\right)\right], \tag{5.2}$$

where oscillations decay on the timescale of the inhomogeneous dephasing time T_2^* with exponent α, which is typically taken to be 2 when low-frequency charge noise is the dominant source of noise. For large pulse heights, the maximum T_2^* is found to be over 7 ns for the left dot. We can use a simple model to understand the dephasing time as the

direct effect of the energy fluctuations between the two lowest states [WWP14]:

$$\sqrt{2}\hbar T_2^{*-1} = \sqrt{\langle \delta E^2 \rangle}. \tag{5.3}$$

For a valley qubit operating at large detuning, charge noise disturbing the value of ϵ should not have a significant impact on T_2^*, as $dE/d\epsilon \to 0$ in this regime. Instead, we attribute the dephasing to fluctuations in the interdot valley coupling parameters Δ and a slight shift in the valley splitting energy. To compare with the charge qubit case in the absence of valley states, the the frequency of precession is $f = \epsilon/\hbar$, resulting in a predicted T_2^* of

$$T_2^* = \sqrt{2}\hbar \left| \frac{dE}{d\epsilon} \sigma_\epsilon \right|^{-1} = \frac{\sqrt{2}\hbar}{\sigma_\epsilon} = 0.5 \text{ ns}, \tag{5.4}$$

where the fluctuations in ϵ are given by the magnitude of the charge noise. In similar devices, our lab calculated the average charge noise to be 2 μeV [FSJ16]. From this predicted value, it is evident that while the valley oscillations have much shorter T_2^* times compared to spin qubits ($\sim 1\mu$s), the valley encoding offers a substantial improvement to the coherence time over the pure charge qubit case due to its charge noise protection.

5.5 Ramsey spectroscopy

The full four-state Hamiltonian (consisting of two charge states, each with two valley states) that was discussed in Chapter 2 is shown below again for convenience in the basis $\{|R_{v1}, |R_{v2}, |L_{v1}, |L_{v2}\}$:

$$H = \begin{pmatrix} \epsilon/2 & 0 & \Delta_1 & -\Delta_2 \\ 0 & \epsilon/2 + E_{VS,R} & -\Delta_3 & \Delta_4 \\ \Delta_1 & -\Delta_3 & -\epsilon/2 & 0 \\ -\Delta_2 & \Delta_4 & 0 & -\epsilon/2 + E_{VS,L} \end{pmatrix}. \tag{5.5}$$

The eigenenergies are depicted in 5.2c and can be reconstructed with Ramsey spec-

troscopy using the voltage pulse shown in the inset of Fig. 5.2c [SSW14]. Ramsey spectroscopy offers an advantage over the square pulses used for Figs. 5.1c-d because it allows us to map out the energy splitting between the two lowest states for both positive and negative detunings simultaneously. This is difficult to accomplish with a square pulse because of reliance on a Landau-Zener transition through the anticrossing to mix the two valley states. Following the logic in Section 5.2, a square pulse with ϵ_p set at the anticrossing ($\epsilon_p \approx 0$) is not fast enough to sufficiently populate the first excited state, reducing visibility. When using the Ramsey pulse, the initial state is always ramped to large positive detuning, ensuring an even mixture of the valley states before the system is pulsed to the operation detuning ϵ_p for a variable amount of time t_p. As long as the ramp to ϵ_p is not too abrupt, the system will precess between the two lowest energy states.

For this experiment, the voltage on the right barrier gate B_R was decreased to reduce tunneling from (1,1) to (1,0). Changing the quantum dot tuning inevitably changes the static dot locations in the device as well as the valley splitting, so we expect to see modified valley oscillation frequencies. The voltage pulse begins as before with a ramp to a sufficiently positive detuning point chosen to yield the highest visibility valley oscillations when performing a trapezoidal pulse. As a result of the first pulse stage, the qubit state transforms into $|-y\rangle = (|L_{v1}\rangle - i|L_{v2}\rangle)/\sqrt{2}$.

In the middle stage of the operation, the detuning is brought to an arbitrary point ϵ_p where the state is allowed to precess for time t_p. Finally the state is brought back to the positive detuning point and then to the initialization point ϵ_0 for readout. This pulse scheme allows for high-visibility precession between the two lowest lying energy levels (Fig. 5.2a), and the frequency of precession can be directly converted into an energy gap. All four energy levels can be determined by plotting the energy gap as a function of ϵ_p (Fig. 5.2b). Left- and right-dot valley splittings $E_{VS,L} = 4.55$ GHz and $E_{VS,R} = 15.7$ GHz were extracted with this procedure as well as the four interdot tunnel couplings: $\Delta_1 = 1.8, \Delta_2 = 12.7, \Delta_3 = 15.6$, and $\Delta_4 = 2.0$ GHz. Important for high-coherence quantum control, the two low-energy states have a "sweet spot" at the anticrossing ϵ=20 μeV where the system is first-order insensitive to charge noise, as well as two "extended

sweet spots" at large positive and negative detunings where the valley splittings become largely independent of gate voltage (Fig. 5.2c).

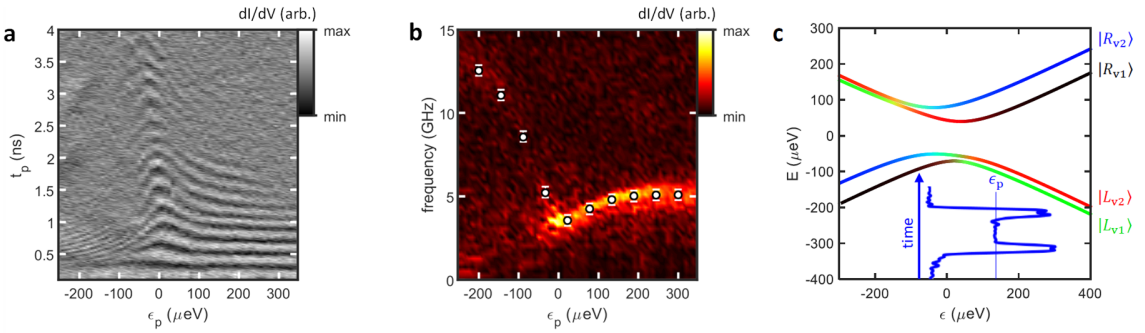

Figure 5.2: Ramsey spectroscopy of the (1,1)-(2,0) transition. **(a)** Precession between the ground and first excited states of the system, induced by a 3-stage Ramsey pulse, as a function of middle-stage pulse width t_p and pulse height ϵ_p. **(b)** Fourier transform of (a) and a fit to a four-state model (overlaid dots). Error bars are obtained from the root mean squared error of the fit. **(c)** Reconstructed energy levels as a function of detuning using the fit from (b). Colors correspond to the four valley states. The calculated Hamiltonian matrix elements are $\Delta_1 = 1.8$ GHz, $\Delta_2 = 12.7$ GHz, $\Delta_3 = 15.6$ GHz, and $\Delta_4 = 2.0$ GHz, as well as valley splittings $E_{VS,L} = 4.55$ GHz and $E_{VS,R}$=15.74 GHz (see Eqn. 5.5 for model Hamiltonian). Inset: the pulse form, measured on an oscilloscope, of a typical Ramsey pulse. Image taken from [Pen20]

5.6 Two-axis control

5.6.1 Control pulse

Two-axis quantum control of the valley qubit was implemented on the left dot valley states using a fast three-stage DC-gated pulse scheme (Fig. 5.3) [KSS14]. After initialization into $|R_{v1}\rangle$ at ϵ_0, the first stage of the pulse brings the detuning to the anticrossing at ϵ_x. The effective two-state Hamiltonian at ϵ_x is $H(\epsilon_x) \approx 2\Delta_1\sigma_x = 2\Delta_1(|R_{v1}\rangle\langle L_{v1}| + |L_{v1}\rangle\langle R_{v1}|$, and the qubit state will precess between the left and right dot charge states for the duration of the pulse stage, t_θ. On the Bloch sphere in the charge basis, this

corresponds to rotations of the qubit state about the x axis with polar angle given by $\theta = 2\Delta_1 t_\theta/\hbar$ in the diabatic limit. Because these two lowest states are mapped to $|L_{v1}\rangle$ and $|L_{v2}\rangle$, this corresponds to a rotation about the x axis of the Bloch sphere in the valley basis shown in blue in Fig. 5.3c.

During the second stage of the pulse, the system is brought to detuning ϵ_z and held for a time t_ϕ, where the effective Hamiltonian becomes $H(\epsilon_z) \approx E_{VS,L}|L_{v2}\rangle\langle L_{v2}|$. This Hamiltonian is orthogonal to $H(\epsilon_x)$ and therefore allows for the second, independent axis of control over the qubit. At this detuning, the qubit rotates around the z axis of the Bloch sphere defined by $|L_{v1}\rangle$ and $|L_{v2}\rangle$, accumulating a total phase $\phi = \frac{E_{VS,L}}{\hbar} t_\phi$. Fig. 5.3c illustrates this azimuthal angle on the Bloch sphere in red.

Not only are the operation detunings chosen so the proper X or Z rotation are completed, but both ϵ_x and ϵ_z are located at "sweetspots" in detuning. The term sweetspot is used here because the system is insensitive to charge noise to first order. This means that at both detunings, fluctuations in ϵ will not lead to drastic changes in operation frequency. Aside from the ramp portion of the pulse, all qubit operations have some protection from charge noise and should display an improved coherence time, which is an important advantage for this qubit.

The last stage of the pulse brings the detuning back to ϵ_x for a time t_θ, equal to that of the first pulse stage. Similar to the first pulse stage, this operation performs x axis rotations and maps the phase ϕ of the valley qubit state to charge states that can be read out at ϵ_0. Since the 200 ps pulse rise time is not fast compared to the state evolution in this stage, the rotations actually occur about an axis that makes an angle $\alpha = \pi/4$ with the x axis in the x-z plane (cyan arrow in Fig. 5.3c).

5.6.2 Mapping the Bloch sphere

By fixing operation points ϵ_x and ϵ_z and varying the time spent at these points during the pulse sequence, the qubit state is swept over the entire surface of the Bloch sphere. Fig. 5.4a shows the measured probability of the final state being in the left dot's excited

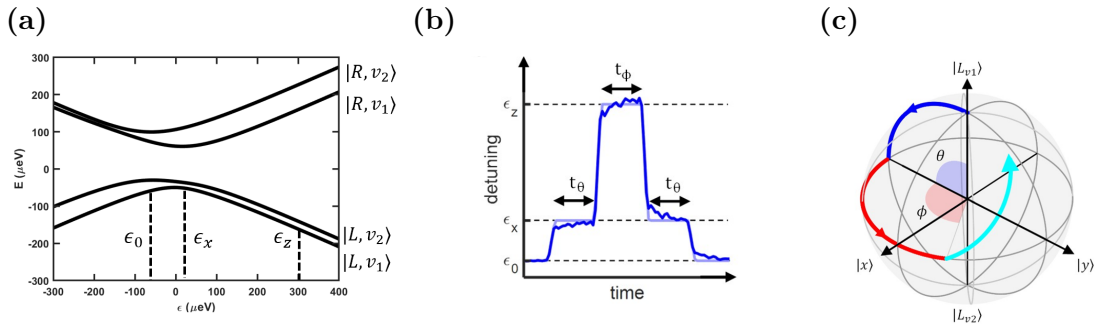

Figure 5.3: Pulse used for two-axis control. **(a)** Four state energy diagram where the detunings for the three pulse stages are labeled. **(b)** Pulse form used for two-axis state rotations. Pulse heights are fixed at ϵ_x and ϵ_z and the pulse widths t_θ and t_ϕ are varied. **(c)** A view of the three pulse stages on the Bloch sphere. In stage 1 (blue), the state is rotated about x by angle θ. In stage 2 (red), the state is rotated about z by angle ϕ, and in stage 3 (cyan) the state is rotated about a tilted axis by angle θ', where $\theta' = \theta$ by design.

valley state $|L_{v2}\rangle$, which we map to the logical $|1\rangle$ of the qubit. The two axes of control are both visible on this plot. Rotations about the z axis are are seen along the t_ϕ axis at a frequency of 4.6 GHz, which equals the valley splitting at ϵ_z. X rotations occur independently along the t_θ axis at a frequency of 2.5 GHz, which equals the energy splitting at ϵ_x.

When the qubit is rotating around the z axis, there will be maximum visibility when this rotation is along the equator of the Bloch sphere. That is, the visibility will be greatest when θ is an odd multiple of $\pi/2$. Whenever the state reaches $|-y\rangle$ in Fig. 5.3c during the middle stage of the pulse, the third stage's X rotation will transform $|-y\rangle$ to $|L_{v2}\rangle = |1\rangle$ (maximum measured probability). When the middle stage ends with $|y\rangle$, the final X rotation transforms this state into $|L_{v1}\rangle = |0\rangle$ (minimum measured probability). Because the qubit is rotating around the z axis at a frequency determined by the left dot's valley splitting $E_{VS,L} = 4.55$ GHz, it is expected for these fringes to have a frequency of 4.6 GHz.

For rotations about the x axis, there should be no oscillations between the two valley states whenever the state vector is pointed along the north or south pole, that is, when θ is a multiple of π. In contrast to the Z rotations, however, the three stage pulse includes not one but two X operations (stage 1 and 3), each rotating the state by an angle θ. This translates to an expected doubling of the frequency at the ϵ_x operation point. We naively should then expect the fringes along t_θ to oscillate at 5 GHz, not 2.5 GHz. This inconsistency is resolved by including rotation errors in the analysis.

As pictured in Fig. 5.3c as the cyan arrow, a 45° tilt in stage 3 of the pulse has already been pointed out. By allowing the first X rotation to have an error of 18° with the x-z plane and the second stage's Z rotation to be tilted by 8° with the x-y plane, we can reliably simulate (Fig. 5.4b) and predict (Fig. 5.4c) the the experimental data. The importance of the tilt α in explaining the 2.5 GHz periodicity is discussed more in the next subsection.

It is important to emphasize that the mapping from the valley to charge configuration in Fig. 5.4a is dependent on t_θ due to the length of the third pulse stage varying. While this complication has little impact on observing the two-axis control, it will become pertinent in Section 5.7. To illustrate this idea, consider the case where t_θ generates a rotation of $\theta = \pi/2$, bringing $|0\rangle$ to $|-y\rangle$ during the first stage of the pulse. Setting $\phi = 0$ (no z rotation) results in the third pulse stage rotating the qubit from $|-y\rangle$ to $|1\rangle$, and a maximum probability will be measured.

Now consider a different t_θ where the initial state is rotated about x by an angle $\theta = 3\pi/2$. Letting the state evolve to $\phi = 0$ will once again leave us with $|-y\rangle$ at the end of the second pulse. However, the third stage will rotate the $|-y\rangle$ by $3\pi/2$ all the way to $|L_{v1}\rangle = |0\rangle$, where the minimum probability is measured. At the end of the second pulse for both cases, $|\psi\rangle = |-y\rangle$, but the measured probability is different. This simple example showcases how the mapping changes with t_θ and must be accounted for when using Fig. 5.4a to map out the state probabilities.

5.6.3 Simulation of the two-axis control

After fitting the Ramsey spectroscopy data in Fig. 5.2 to the energy difference between the two lowest eigenstates of Eqn. 5.5, the extracted parameters were used to simulate the two-axis control in Fig. 5.4a. To include inhomogeneous dephasing into the simulation, the system was evolved using the Lindblad equation:

$$\frac{\partial \rho}{\partial t} = -\frac{i}{\hbar}[H, \rho] + \gamma \left(C\rho C^\dagger - \frac{1}{2}\{C^\dagger C, \rho\} \right), \tag{5.6}$$

where ρ is the density matrix, $\gamma = 1/T_2^*$ is the dephasing rate for the pulse stage, and C is the dephasing operator for the pulse stage. An appropriate dephasing operator for each stage of the pulse is one between ground and excited eigenstates: $C = |g\rangle\langle g| - |e\rangle\langle e|$. The dephasing time the X and Z rotations were extracted from the Ramsey spectroscopy data as well, where $T_{2,x}^* \approx 10$ ns and $T_{2,z}^* = 1.5$ ns. The result of this simulation is shown in Fig. 5.4b, which matches to the data well.

In addition to simulation, we can reproduce this qubit's evolution around the Bloch sphere using $SU(2)$ unitary operators to represent the rotation at each stage of the pulse:

$$U_1(\theta) = \cos\left(\frac{\theta}{2}\right) I - i \sin\left(\frac{\theta}{2}\right) \sigma_x, \tag{5.7}$$

$$U_2(\phi) = \cos\left(\frac{\phi}{2}\right) I - i \sin\left(\frac{\phi}{2}\right) \sigma_z, \tag{5.8}$$

$$U_3(\theta) = \cos\left(\frac{\theta}{2}\right) I - i \sin\left(\frac{\theta}{2}\right) (\sigma_x \cos\alpha + \sigma_z \sin\alpha), \tag{5.9}$$

where the angles θ and ϕ are the polar and azimuthal angles of the Bloch sphere (see Fig. 5.3c), I is the identity operator, and σ_i are the Pauli operators. Here, the $\alpha = 45°$ tilt of the third stage of the pulse is already included in Eqn. 5.9. Using these expressions, the measured projection after the pulse can be written as $\langle L_{v2}|U(\theta,\phi)|L_{v1}\rangle$, where $U(\theta,\phi) = U_3(\theta)U_2(\phi)U_1(\theta)$. The corresponding probability of finding the qubit to be in the excited

valley state is sinusoidal in ϕ, and oscillations vanish when θ is an even multiple of π:

$$|\langle L_{v2}|U(\theta, \phi = 0)|L_{v1}\rangle|^2 = (1 - \cos\theta)\left(1 + \frac{1}{\sqrt{2}}\cos\theta\right). \tag{5.10}$$

By including the rotation error α in $U_3(\theta)$, the 2π periodicity (corresponding to a frequency of 2.5 GHz) seen along the vertical axis in Fig. 5.4a is resolved. Without α, one would observe the naively expected 5 GHz frequency. This model is further improved by adding rotation axis deviations in pulse stages 1 and 2 of 10° and 6° respectively, which is plotted in Fig. 5.4c.

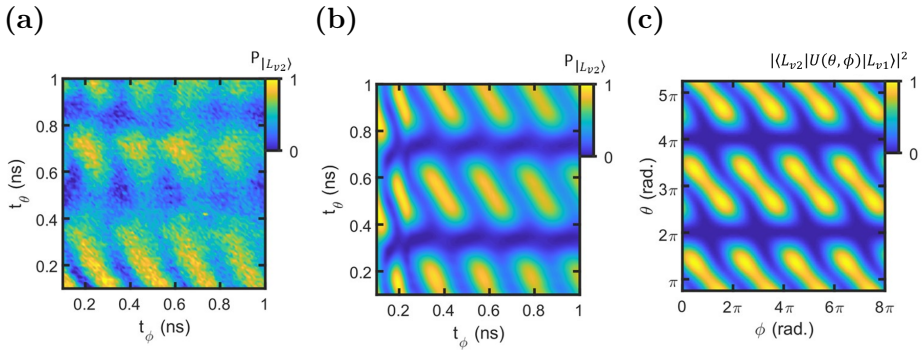

Figure 5.4: Quantum control of the valley qubit. **(a),(b)** Measured and simulated oscillations with a dynamical projection axis determined by t_θ, demonstrating a complete map of the Bloch sphere surface. Independent oscillations as functions of pulse widths are visible with frequencies of 4.6 GHz and 2.5 GHz. A linear background is subtracted from the data. **(c)** Theoretical prediction of the measured probability $|\langle L_{v2}|U(\theta, \phi)|L_{v1}\rangle|^2$ with $U(\theta, \phi)$ given by the product of Eqs. 5.7, 5.8, and 5.9.

5.7 Benchmarking qubit performance

Once two-axis control over a qubit has been established, the next logical step is to characterize how well the operations are being performed. Ideally, this benchmarking allows for the comparison of the qubit to not only similar devices but also to completely different architectures that hosts qubits. The basic question to answer is how similar is

the qubit's operation to the ideal scenario, which can generally be termed as the qubit's fidelity. The greater this similarity, the higher the qubit's fidelity.

As briefly touched upon in Chapter 1, a scalable qubit platform must exhibit operations that meet a $\sim 1\%$ error threshold for current error correction schemes. Put another way, gate operations need to surpass 99% fidelity. To measure a qubit's fidelity, several benchmarking methods have been developed, but the most accepted approach involves generating a sequence of randomly selected gates and comparing the outcome to the expected result [HYC19]. Because this technique requires a stable device and extensive flexibility in developing pulses, we opted to use an alternative fidelity measurement known as quantum process tomography (QPT) [CGT09]. While QPT is too burdensome for systems with more than four qubits and cannot distinguish between different types of errors, it offers a simple pathway to characterize our single qubit device. As one might expect, QPT requires the reconstruction of the qubit state after the application of a gate. The reconstruction is completed through an initial analysis called quantum *state* tomography and is the focus of the next section.

5.7.1 Quantum state tomography

True quantum process tomography for a single qubit would entail initializing into four linearly independent basis states and separately measuring the x, y, and z projections of the final state after a gate operation. Although the information given by our dynamical projection approach does not constitute a complete set of state tomography, a less rigorous calculation of QPT can be obtained by matching the data with the theoretical model in Fig. 5.4c and then reconstructing the qubit state from the measured probabilities accordingly (Fig. 5.5).

Because t_θ spans several periods (see Fig. 5.4c), the states $|0\rangle, |\pm y\rangle$, and $|1\rangle$ were explicitly prepared. Missing from this list are the $|\pm x\rangle$ states, but due to the tilted X rotations, we have access to these two two states when $\theta = 3\pi/2 + 2\pi n$, where the additional Z rotation from the tilted X operation equals $\pi/2$. For instance, at $\theta = \pi/2$

the y projection is being measured while at $\theta = 3\pi/2$ the x projection is probed. Missing components, like the x and y projections of the qubit state when initialized in state $|+z\rangle = |L_{v1}\rangle$, are approximated from traces where oscillations are minimized at $\theta = 2\pi$ and 4π. Due to the heavily suppressed tunneling rate from (1,1) to (2,0), we further assume that electrons do not tunnel out of the dots during qubit operations, which allows us to map the upper and lower limits of the measured transconductance directly to the probability of the qubit to be in state $|-z\rangle = |L_{v2}\rangle$.

Quantum state tomography uses these x, y, and z projections to determined the state of the qubit. Every density matrix ρ can be written as a linear combination of the Pauli matrices and identity matrix [TNW02, Bha14]:

$$\rho = \frac{1}{2}(I + s_x\sigma_x + s_y\sigma_y + s_z\sigma_z), \tag{5.11}$$

where s_i are the normalized Stokes parameters and σ_i are the Pauli matrices. For an ideal qubit, we can simply use three independent projections measured on Fig. 5.4a as the expectation values for these Stokes parameters. However, experimental errors may lead to nonphysical density matrices, so it is generally best to fit each density matrix in such a way that satisfies the typical properties of a density matrix: (1) ρ is Hermitian, (2) the eigenvalues of ρ are zero or greater, and (3) $Tr(\rho) = 1$. To enforce these requirements, ρ can be fit to a T-matrix that has these properties using a least-squares technique [PAJ03]:

$$\rho = \frac{T^\dagger T}{Tr(T^\dagger T)}, \qquad T = \begin{pmatrix} t_1 & 0 \\ t_3 + it_4 & t_2 \end{pmatrix}. \tag{5.12}$$

Due to read-out noise and the sensitivity of quantum process tomography to the calculated density matrices, we elect to first fit the raw projection data to decaying sinusoidal curves as a function of t_ϕ (solid lines in Fig. 5.5). This not only ensures the x, y, and z projections fall within the bounds of [0,1], but also generates a stable data set that will allow for sensible fidelity calculations in the following sections.

After fitting these t parameters, the qubit's state can be plotted on the Bloch sphere (Fig. 5.5). Here, we show the qubit's state as a Z rotation is applied for two different initializations: red corresponds to the initial state $|-y\rangle$ and blue for the initial state $|+z\rangle = |L_{v1}\rangle$.

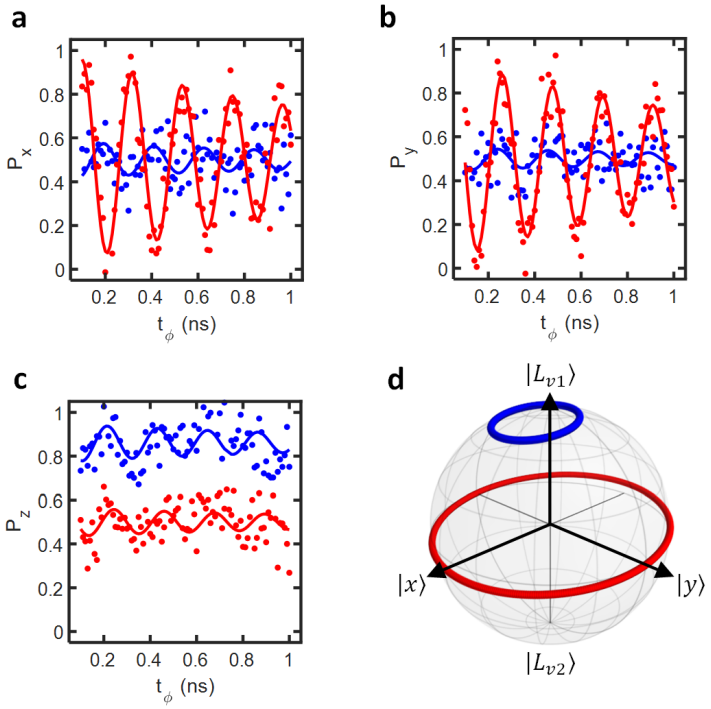

Figure 5.5: State tomography of Z rotations. **(a),(b),(c)** Red dots represent state projections when the qubit is initialized in state $|-y\rangle$ ($\theta = \pi/2$), and blue dots indicate an initial state of $|+z\rangle$ ($\theta = 2\pi$). Data is extracted from Fig. 5.4a and solid traces are fits to a decaying exponential with a 4.6 GHz frequency. **(d)** Normalized trajectories of the qubit state on the Bloch sphere during Z rotations using the fits from state tomography.

5.7.2 Quantum process tomography

Once the density matrix for the qubit before and after an operation is fitted, we can continue with quantum *process* tomography to calculate how close to the output density matrix was to the ideal outcome. QPT measures this difference by finding a transforma-

tion that maps an input density matrix to an output [MRL08, OPG04]:

$$\mathcal{E}(\rho_{in}) = \rho_{out} = \sum_{m,n=0}^{d^2-1} \chi_{mn} A_m \rho_{in} A_n^\dagger. \tag{5.13}$$

Here, the matrix χ is the process matrix that completely describes the map $\mathcal{E}$, A_n are a basis for the operators acting on ρ, and $d = 2^n$ is the dimension of the qubit space. Since we are dealing with a single qubit gate, $n = 1$ and $d = 2$. For these single qubit rotations, a basis that is natural choice are the Pauli matrices $A = \{I, \sigma_x, \sigma_y, \sigma_z\}$ once again. The goal of QPT is to compute χ and compare it to the ideal mapping χ_{ideal} for the operation one is interested in.

To solve for χ, Eqn. 5.13 must be inverted. First, $\mathcal{E}(\rho_k)$ is decomposed into a linear combination of basis states ρ_l: $\mathcal{E}(\rho_k) = \sum_l \lambda_{kl} \rho_l$. We define a similar relation for the right hand side of Eqn. 5.13: $A_m \rho_k A_n^\dagger = \sum_l B_{kl}^{mn} \rho_l$. Combining these two relations with Eqn. 5.13 gives $\sum_{mn} B_{kl}^{mn} \chi_{mn} = \lambda_{kl}$, which can be expressed as the following matrix equation [MRL08]:

$$\mathbf{B}\chi = \lambda, \tag{5.14}$$

Calculating the pseudo-inverse of $\mathbf{B}$ allows us to solve for the $d^2 \times d^2$ process matrix $\chi = \mathbf{B}^{-1}\lambda$. Just as when ρ was fit, we wish to enforce that χ is semi-definite, Hermitian, and has a trace of 1. This is once again done through a suitable T-matrix:

$$\chi = \frac{T^\dagger T}{Tr(T^\dagger T)}, \qquad T = \begin{pmatrix} t_1 & 0 & 0 & 0 \\ t_5 + it_6 & t_2 & 0 & 0 \\ t_{11} + it_{12} & t_7 + it_8 & t_3 & 0 \\ t_{15} + it_{16} & t_{13} + it_{14} & t_9 + it_{10} & t_4 \end{pmatrix}. \tag{5.15}$$

Through another maximum likelihood estimation (MLE), the t parameters are fit to real values and χ is found from the fit that best transforms ρ_{in} to ρ_{out} under the enforced

physical conditions:

$$f(\mathbf{t}) = \sum_{k,l=1}^{2} (\rho_{out,kl} - \mathcal{E}(\rho_{in,kl}, \mathbf{t}))^2. \tag{5.16}$$

Once the experimental process matrix is known, it is used with the ideal process matrix to calculate the operation's fidelity:

$$\mathcal{F} = \mathrm{Tr}[\chi_{\mathrm{ideal}}\chi]. \tag{5.17}$$

5.7.3 Valley qubit fidelities

For the valley qubit, we are interested in the extra protection from charge noise offered by the extended parallel region in detuning where the energy splitting is approximately constant at $E_{VS,L}$ (see right hand side of Fig. 5.2c). At these detunings, the qubit performs Z rotations, which will then be the family of operations we choose to focus our attention on. In particular, we measure the fidelities for Z($\pi/2$), Z(π), and Z(2π) operations. We first choose a starting point at some time t_0 as the initial state. Then we select a future point in time that corresponds to the rotation angle. For instance, the Z($\pi/2$) rotation occurs at a time $t_0 + \delta t$, where $\delta t = 1/4f = \hbar/4E_{VS,L}$. From these two times, the fidelity $\mathcal{F}_{\pi/2}$ is calculated. We can repeat this calculation for a number of starting points to generate the average and standard deviation of $\mathcal{F}_{\pi/2}$.

Because we chose to fit the projection measurements in Fig. 5.5 to curves before the state tomography, we lose some uncertainty due to errors in state preparation and measurement. However, the error in $\mathcal{F}$ is dominated by the uncertainty from the MLE method, permitting a reasonable estimate of the variance. To further address the sensitivity of χ to the initial guess, we use the process matrix corresponding to the median fidelity in a data set as the initial guess for a second iteration of finding $\mathcal{F}$.

The result of these χ measurements for the chosen Z operations are pictured in Fig. 5.6a,c,e, which show good qualitative agreement with the ideal maps in the lower panels for comparison (Fig. 5.6b,d,f). Using these process matrices, we calculate the fidelities

to be $\mathcal{F}_{\pi/2} = 0.85 \pm 0.02, \mathcal{F}_{\pi} = 0.79 \pm 0.02$, and $\mathcal{F}_{2\pi} = 0.93 \pm 0.01$.

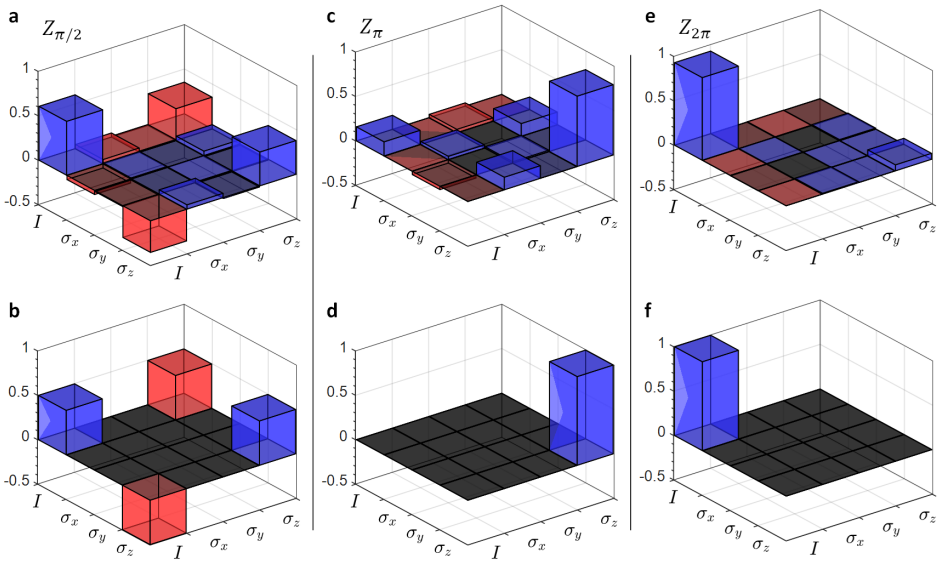

Figure 5.6: Quantum process tomography for valley (Z) rotations. **(a),(c),(e)** Measured process matrices based on a fit of state tomography data. The color of each matrix element bar denotes complex phase: blue is real, red is imaginary. **(b),(d),(f)** Ideal process matrices for comparison. Calculated fidelities $F = \mathrm{Tr}(\chi_{\mathrm{ideal}}\chi)$ are $F_{\pi/2} = 0.85 \pm 0.02$, $F_{\pi} = 0.79 \pm 0.02$, and $F_{2\pi} = 0.93 \pm 0.01$.

The decreases in fidelity of the smaller rotations when compared to the full 2π rotation can be understood by the trajectory of the qubit state. From state tomography, it is clear that the actual rotation axis is tilted away from the z axis by about 10 degrees. The identity (2π) process matrix is insensitive to the choice of rotation axis, whereas the NOT (π) process matrix is maximally sensitive. Since the fidelity of the 2π process is greater than the fidelities of the smaller rotations, this suggests that the fidelity is limited by rotation axis errors and not by decoherence. Attenuation and pulse-shaping considerations may be able to alleviate this effect in future work, although a crucial variable that controls decoherence and rotation axis error is the choice of operation point ϵ_z. Analysis of the energy level diagram suggests that the energy splitting is still slowly converging in the region of ϵ_z, leading to a nonzero first-order sensitivity to charge noise as well as a non-negligible charge coupling that contributes to the undesired

rotation axis tilt. This conclusion is further supported by the measured coherence time during Z rotations of 1.5 ns, smaller than the value of T_2^* obtained from trapezoidal pulse experiments and much smaller than typical valley relaxation times [KSW14]. Pulsing further into the region of detuning-invariant energy splitting would certainly lead to improved gate fidelities and coherence times.

5.8 Principle sources of error

We identify decoherence due to charge noise and rotation errors arising from pulse imperfections as the main sources of error that lead to suboptimal fidelities in our system. Estimates of the expected operation fidelity can be calculated in the cases of (1) perfect rotations in the presence of dephasing and (2) tilted rotations with no dephasing. The dependence of fidelity on dephasing time and off-axis rotation tilt indicates the dominant error source and provides insight into what can be done to further improve the qubit operation. To estimate the fidelity in the first case, Larmor precession in a general two-level system is simulated in the presence of variable dephasing times (Fig. 5.7d). In the second case, unitary transformations corresponding to an X rotation by $\theta = \pi/2$ (Eqn. 5.7) and a Z rotation by ϕ (Eqn. 5.8) are applied to the initial state $|+z\rangle$, with both rotation axes tilted by some amount in the x-z plane (Figs. 5.7a,b,c). Here, we choose a definition of fidelity given by [NC10]

$$\mathcal{F} = \mathrm{Tr}\left(\sqrt{\rho_t}\rho\sqrt{\rho_t}\right), \tag{5.18}$$

where ρ is the "measured" qubit density matrix after the operation and ρ_t is the target density matrix resulting from perfect operation. Although Eq. 5.18 is not independent of choice of the initial state, as the process matrix formalism is, this version is much faster to calculate and provides a fidelity estimate that is sufficiently accurate for the purpose of this analysis.

From dephasing considerations alone, the fidelity is expected to decrease as a function

of dephasing rate $1/T_2^*$ and operation time. For the experimentally determined dephasing time of 1.54 ns, our simple model gives fidelities of 98%, 97% and 94% for Z rotations of $\pi/2, \pi$ and 2π respectively. These values are well above the measured process fidelities for all operations except the 2π rotation, which was found to be 93%.

Considering rotation errors in the absence of dephasing, we see that the 2π rotation about the z axis is minimally sensitive to off-axis tilts, while the π rotation is maximally sensitive. This is qualitatively identical to what is experimentally observed. In fact, for an x axis tilt of 18 degrees and a z axis tilt of 6 degrees, the estimated fidelities based on rotation errors alone are 87%, 84% and 90% for Z rotations of $\pi/2, \pi$ and 2π respectively, quite close to the experimental fidelities. This suggests that the performed qubit rotations are limited in quality by rotation errors rather than dephasing. Such rotation errors likely result from imperfect pulse shaping, for example voltage drift at the X operation point.

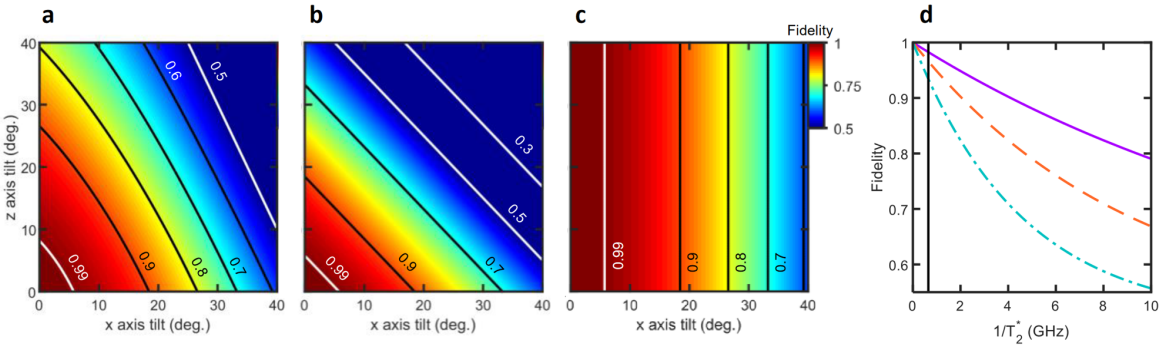

Figure 5.7: Impact of rotation errors on **(a)** a $Z_{\pi/2}$ operation, **(b)** a Z_π operation, and **(c)** a $Z_{2\pi}$ operation. The initial state $|+z\rangle$ is first rotated about the nominal x axis by $\pi/2$ (subject to an x axis tilt). **(d)** Fidelities for $Z_{\pi/2}$ (solid purple), Z_π (dashed orange), and $Z_{2\pi}$ (dashed cyan) operations as a function of dephasing time T_2^*. Vertical black line indicates the experimentally determined $T_2^* = 1.54$ ns.

5.9 Conclusion

In summary, we have shown that a semiconductor qubit formed from valley states in silicon can be electrically controlled to perform independent rotations about two orthogonal axes. Sub-nanosecond operation times, determined by valley splitting, range from 200 ps to 300 ps. Although the performance of this particular valley qubit is inferior to the similarly operated hybrid qubit system in terms of coherence times [KWS15], proper pulse engineering and readout can in principle lead to fidelities greater than 90% at multiple charge configurations. This chapter explored the utility of valley degrees of freedom as alternatives to electron charge and spin for storing and manipulating quantum information in silicon and further investigated methods for limiting charge noise-induced decoherence.

CHAPTER 6

Gate modulation of the hole singlet-triplet qubit frequency in germanium

Chapter 3 detailed the lowermost spin states that define a two hole system of a double quantum dot in strained germanium. As touched on in Chapters 1 and 3, utilizing the spin states of quantum dots is not only an intuitive system for qubits, but is arguably one of most successful encodings in semiconductor quantum dots. In particular, using hole states in strained germanium has become a popular approach and has developed rapidly over the past several years (see the introduction of Chapter 3).

The success of these experiments can be partly attributed to the various advantages of holes for spin qubit encoding [SKZ21]. In stark contrast to the case of electrons described in Chapter 2 and showcased in Chapter 5, the two topmost valence bands in Ge are well separated in energy due to strain and 2D confinement. The light effective mass ($0.054\mathrm{m}_e$ [LHL21]) of holes in this topmost band and the absence of valley degeneracy allows us to easily access the two highest hole states for spin encoding. Furthermore, Ge hole spin coherence times benefit from their weak hyperfine interaction with surrounding nuclear spins. Finally, because of their strong spin-orbit coupling and site-dependent g-tensors, Ge hole quantum dots do not require the fabrication of micromagnets, advancing their potential for scalability and integration into current industrial semiconductor facilities [SKZ21]. Building on this success, this chapter is based on the the successful demonstration of coherent spin manipulation our lab achieved in 2023 [RLS23], and the layout of this chapter closely follows this work.

Most double quantum dot singlet-triplet qubit studies have focused on encodings between the singlet $|S\rangle$ and unpolarized triplet $|T_0\rangle$ states [JHB21, WWP14, PJT05, MBH12]. This chapter will instead detail the dynamics of the $S - T_-$ subspace, which has been less studied thus far [JMH22, WSV22b, WDT23]. Furthermore, we explore the tunability of the hole g-tensors by varying the electrostatic potential generated by the barrier gate bridging the two quantum dots. As quantum computation with Ge hole spins critically depends on the g-tensor, the ability to manipulate the g-tensor becomes a valuable asset for a spin qubit encoded in this system.

6.1 The few-hole regime

A scanning electron microscope image of the device studied is shown in Fig. 6.1a along with the Ge/SiGe heterostructure in Fig. 6.1b. The strained Ge quantum well is 16 nm in width and located 55 nm below the surface. For more details regarding the heterostructure, see [LHL21] and Section 4.1.1. A two-dimensional hole gas is first created in the Ge well by applying a negative voltage to a global top gate situated above the gates pictured in Fig. 6.1a. The double quantum dot (DQD) is then formed underneath plungers P_1 and P_2 by applying appropriate voltages to the neighboring barrier gates, where the middle barrier voltage V_B controls the coupling between the two dots.

Varying the plunger voltages controls the chemical potential of each dot. By applying an increasingly positive voltage to a plunger, the chemical potential for N holes on the dot is raised above the chemical potential of the nearby reservoir. This allows the hole to escape the dot and tunnel to the reservoir. By applying sufficiently positive voltages to both plungers, we can empty the dots until the few-hole regime is reached (Fig. 6.1c), where all experiments were performed at the (1,1)-(0,2) charge configurations (Fig. 6.1d).

The hole occupation of both dots was detected by the nearby single electron transistor (SET) located on the left half of the device labeled in Fig. 6.1a. For convenience in describing this DQD system at the (1,1)-(0,2) anticrossing, we define the relative energy of the two quantum dots as the detuning $\epsilon = \alpha_2 V_{P2} - \alpha_1 V_{P1}$, where α_i converts the

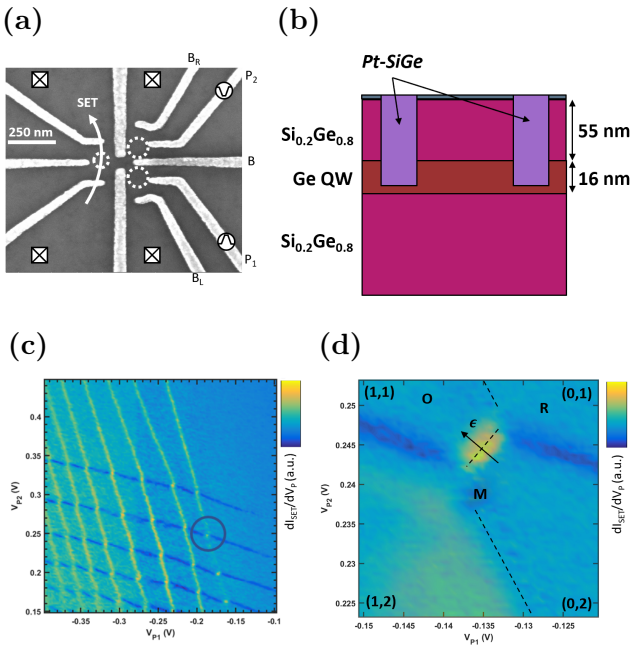

Figure 6.1: **(a)** SEM image of lithographically defined gates identical to the device used in this study. The magnetic field applied was $B_\perp = 1.2$ and $B_\parallel = 4.4$ mT. **(b)** Heterostructure of the device showing the Ge quantum well packed between two Ge rich SiGe layers. **(c)** A typical stability diagram with the circle highlighting the (1,1)-(0,2) anticrossing. **(c)** All experiments were completed at the (1,1)-(0,2) anticrossing, where (n,m) denotes the hole occupation for each dot. Point R was used to reset the DQD, M for measurement and initialization, and O for coherent operation between the singlet and triplet states.

voltage applied to P_i to the change in the energy level of dot i. Fig. 6.1d illustrates the detuning axis on the stability diagram, where $\epsilon = 0$ at the (1,1)-(0,2) boundary (dotted line). The black arrow depicts the direction I have defined as positive detuning.

6.2 Observation of coherent spin oscillations

When the system passes the $\epsilon = 0$ detuning line into the (1,1) charge configuration, Section 3.6 outlined how the (0,2) singlet state hybridizes with the (1,1) singlet due to the tunnel coupling between the quantum dots: $|S\rangle = \sin(\Omega/2)|S_{02}\rangle - \cos(\Omega/2)|S_{11}\rangle$.

Here, $\Omega = \arctan\left(\frac{2\sqrt{2}t_c}{\epsilon}\right)$ is the mixing angle between the two singlet states. In addition to the singlet state, Fig. 6.3c depicts the three triplet states that compose the four lowest energy levels in the (1,1) charge configuration. A simple block magnet situated near the device's PCB provided the field necessary to lift the degeneracy of the three triplet states, generating an estimated fixed global out-of-plane field of 1.2 mT and in-plane field of 4.4 mT measured at the device's position ($|\mathbf{B}| = B = 4.6$ mT points $\theta = 15°$ out of the x-y plane). This tilted field differs from previous qubit experiments on this heterostructure where B was completely in-plane, allowing for a unique perspective into the hole spin states [HLR21, WDT23]. Importantly, the magnetic field splits the polarized triplet $|T_-\rangle$ from $|T_0\rangle$ by the average Zeeman energy of the quantum dots $\overline{E}_z$.

Beginning at M in Fig. 6.1d, the system is first initialized into the (0,2) singlet state by waiting for 0.5 μs for a hole to tunnel onto the dot. A voltage pulse was then applied to P_1 and P_2 to quickly separate the holes, moving the system into the (1,1) charge configuration (point O). Just as in Section 5.2, an admixture between the $|S\rangle$ and $|T_-\rangle$ is generated through a Landau-Zener transition as the system passes through the $S - T_-$ anticrossing, resulting in part of the initialized state remaining as a singlet and the remaining going to $|T_-\rangle$.

Once the holes were separated, the system was pulsed to various operation detunings ϵ_P and allowed to evolve for a time t_E between $|S\rangle$ and $|T_-\rangle$ where the system undergoes Larmor precession (Fig. 6.3a and 6.3c). The qubit frequency (Fig. 6.3b) is given by the energy difference between these two states at the operation detuning: $hf = \Delta E_{ST_-}$, which plateaus to roughly $\overline{E}_z$ for large detunings.

For smaller operation detunings, the energy splitting reaches a minimum at the $S-T_-$ anticrossing, where it approximately equals $2\Delta_{ST_-}$. We define Δ_{ST_-} as the coupling between $|S\rangle$ and $|T_-\rangle$ at the $S - T_-$ anticrossing. The existence of this minimum leads to the observed chevron pattern at 1 meV in Fig. 6.3a, which has been seen in previous $S - T_-$ works and absent from studies coherently manipulating the $S - T_0$ states [JHB21, JMH22, WDT23, WWP14, WSV22b, PJT05, MBH12]. By varying the opera-

tion detuning ϵ_P from 0.5 to 2.5 meV, we sampled the energy splitting between the two lowest states for both of these detuning regimes.

6.2.1 Readout mechanism

To read out the final two-hole state after the qubit operation, the system was left at point M for 20 μs. Point M sits inside what is known as the Pauli spin blockade (PSB) window, which enables spin to charge conversion of the two hole state. While in the PSB region, only the singlet (1,1) state is energetically allowed to tunnel to the singlet (0,2) state. In contrast, all triplet states are prohibited from tunneling to (0,2) due to a large singlet-triplet splitting $E_{ST_{02}}$ in the (0,2) charge configuration. The triplet states also are prevented from tunnelling to the singlet (0,2) state due to the conservation of spin. The top panels of Fig. 6.2 illustrate the singlet state being allowed to tunnel to the (0,2) configuration, while the triplet states are blocked. Once the (0,2) triplet states are low enough in energy, the (1,1) triplet state can also tunnel to the (0,2) configuration (lower panels of Fig. 6.2).

Because spin-selective tunneling to the (0,2) charge configuration exists while in the PSB region, the SET current will either detect a change in the hole configuration to (0,2), signifying the final state as $|S\rangle$, or no change in hole occupation will be seen, indicating the final state as $|T\_\rangle$. The system is then reset at R for 1 μs before repeating the cycle again.

6.2.2 Singlet-triplet splitting in (0,2)

The energy splitting $E_{ST_{02}}$ between the singlet and triplet states in the (0,2) charge configuration was measured by varying the readout position ϵ_r of the Ramsey pulse. As the readout position is further pushed deeper into the (0,2) charge configuration, it will eventually surpass the PSB boundary the SET uses to distinguish the singlet and triplet states. From Fig. 6.2, we measure this cutoff and therefore $E_{ST_{02}}$ to be 0.9 meV. Knowing the orbital energy difference defines the (0,2) singlet-triplet splitting, we can use $E_{ST_{02}}$

to estimate the size of the right dot by approximating the confinement potential to be a 2d box and the dot shape to be a disk:

$$E_{ST_{02}} = \frac{3\hbar^2\pi^2}{2m^*L^2}$$
$$E_{ST_{02}} = \frac{3\hbar^2\pi^2}{2m^*\pi r^2},$$

where $m^* = 0.09m_e$ and r is the radius of the dot. From $E_{ST_{02}} = 0.9$ meV, we calculate the radius of the right dot to be $r = 66$ nm. By comparing the charging energies of the left and right dot and using the fact that $E \sim 1/r^2$, we further estimate the size of the left dot to be $r = 75$ nm.

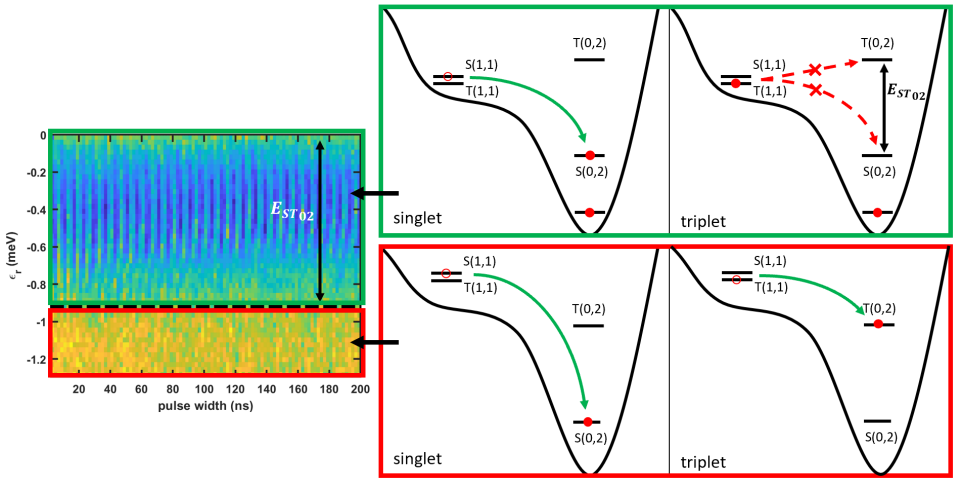

Figure 6.2: By scanning the readout position ϵ_r of the Ramsey pulse, we measured the energy splitting between the singlet and triplet states in the (0,2) charge configuration. As the readout position is moved further into (0,2), PSB is eventually lifted as the (1,1) triplet state is allowed to tunnel to the (0,2) triplet. By detecting the readout position where this transition occurs, we measured $E_{ST_{02}} = 0.9$ meV.

6.2.3 The $S - T_-$ Hamiltonian

To understand these dynamics, we utilize a Hamiltonian describing the $\{|S\rangle, |T_-\rangle\}$ subspace that was derived in Ref. [MB21b] and introduced in Section 3.6.3. To leading

order, it takes the following form:

$$H = \begin{pmatrix} -J(\epsilon) & \Delta \\ \Delta & -\overline{E}_z \end{pmatrix}. \tag{6.1}$$

We define the exchange energy $J(\epsilon) = -\frac{\epsilon}{2} + \sqrt{\frac{\epsilon^2}{4} + 2t_c^2}$ as the energy difference between $|S\rangle$ and $|T_0\rangle$. The coupling of the $S-T_-$ states (Δ) emerges from two sources: (1) a spin-orbit splitting (Δ_{so}) and (2) an effective Zeeman splitting due to the anisotropy of the g-tensors (g_a) that is only present when B has non-zero in- and out-of-plane components: $\Delta = \Delta_{so} \sin\left(\frac{\Omega}{2}\right) + g_a \mu_B B \cos\left(\frac{\Omega}{2}\right)$ [JMH22, MB21b]. The anisotropy between the in- and out-of-plane g-factors of a quantum dot has been previously observed, where the in-plane g-factors ($g_\parallel$) were measured to be a few tens to hundreds of times smaller than their out-of-plane counterparts ($g_\perp$) for holes in Ge/SiGe substrates [JMH22, HMM23]. The $|T_-\rangle$ state splits from $|T_0\rangle$ by the average Zeeman energy, $\overline{E}_z = \overline{g}\mu_B B$, where $\overline{g}$ is the average g-factor of the two dots projected onto the axis of $\mathbf{B}$.

With this Hamiltonian, we can solve for the frequency of the $S - T_-$ evolution: $f = \frac{1}{h}\sqrt{(J - \overline{E}_z)^2 + (2\Delta)^2}$. At the $S - T_-$ anticrossing, $J = \overline{E}_z$, and f is controlled by Δ, where X rotations are performed around the Bloch sphere (red circle in Fig. 6.3d). For large detunings, $J \to 0$, leaving f to be determined by the average Zeeman energy and $S-T_-$ coupling, and the qubit rotates near the z axis (blue circle in Fig. 6.3d). The larger the ratio $\frac{\overline{E}_z}{\Delta}$ becomes, the closer this axis aligns with the z direction. With control over the orientation of the magnetic field, it is possible for $\Delta \to 0$ at specific detunings, resulting in perfect Z rotations [MB21b].

6.3 Dephasing and relaxation measurements

We analyzed the dephasing and relaxation of this qubit by measuring T_2^* and T_1.

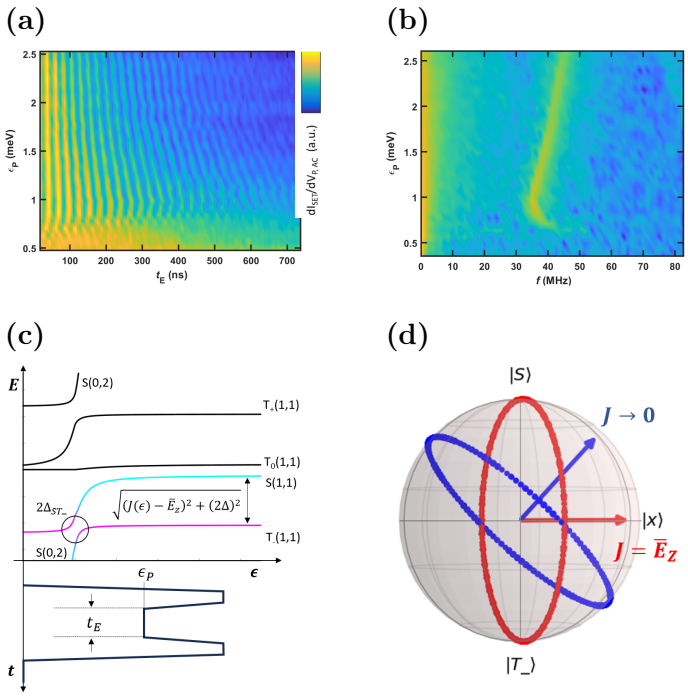

Figure 6.3: **(a)** Coherent oscillations between $|S\rangle$ and $|T_-\rangle$. **(b)** Fourier transform of the coherent oscillations in (a), illustrating the $S - T_-$ energy splitting as a function of detuning. **(c)** Energy levels (not to scale) of the singlet and triplets as a function of detuning. The Ramsey pulse used is shown below as a function of time and detuning. **(d)** Bloch sphere depicting the two rotation axes for the $S - T_-$ subspace. When ϵ_P is at the $S - T_-$ anticrossing, the system undergoes X rotations (red axis). For large detunings, a combination of X and Z rotations are performed (blue).

6.3.1 T_2^* dephasing time

To measure T_2^*, we extracted the decay of oscillations between $|S\rangle$ and $|T_-\rangle$ in Fig. 6.3a. Each linecut along ϵ_P is fit to the equation $P = Ae^{-(t/T_2^*)^2}\cos(\omega t + B) + Ce^{-t/D} + E$, where A, B, C, D, and E are fitting parameters in addition to T_2^*. The angular frequency $\omega = 2\pi f$ is already known from the Fourier transform data. Several example fitted traces are shown in Fig. 6.4, where the background ($Ce^{-t/D} + E$) has been subtracted off.

After extracting T_2^* as a function of ϵ_P (Fig. 6.5a), a clear dependence on the pulse height is seen. This behavior can be understood with a simple model describing the

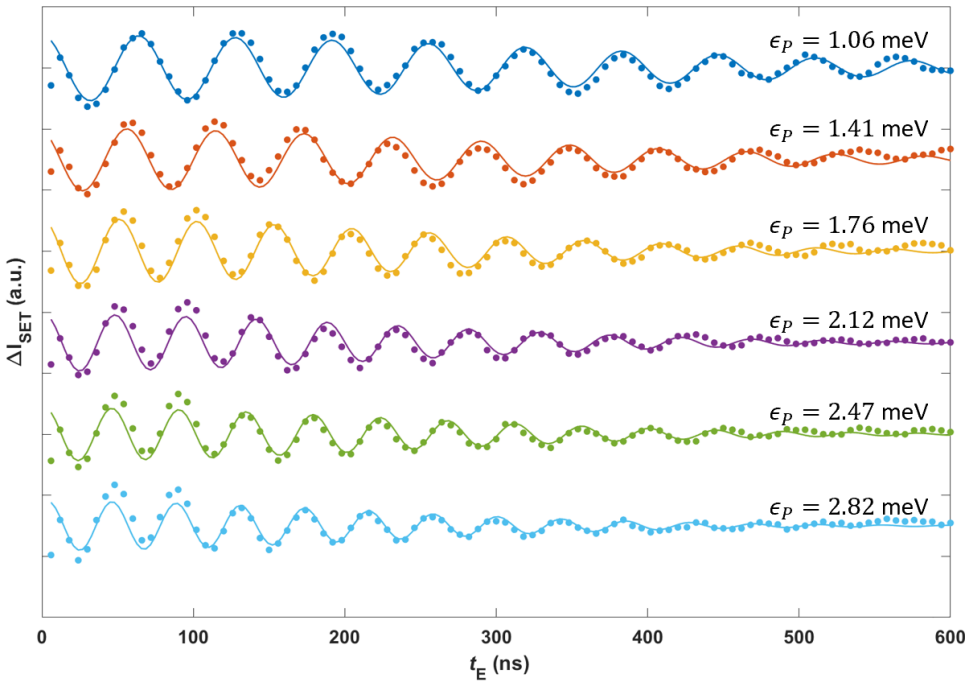

Figure 6.4: Traces taken from Fig. 6.6f for several values of operation detuning ϵ_P. Each trace is fit to a decaying sinusoid with an exponential background and offset. The background is removed before plotting the change in the SET current (ΔI_{SET}) for both the trace and fit (solid line). Each trace is offset along the vertical axis for clarity.

influence of charge and magnetic noise on the fluctuations in the energy difference between the two states [WWP14, JHB21]:

$$\sqrt{2}\hbar T_2^{*-1} = \sqrt{\langle \delta E^2 \rangle}. \tag{6.2}$$

At the $S-T_-$ anticrossing where the qubit frequency reaches a minimum, the system is insensitive to first-order to fluctuations in ϵ due to charge noise. This protection leads to the maximum in T_2^* seen at 1 meV in Fig. 6.5a. However, the qubit is still susceptible to electrical noise affecting the dot g-factors and tunnel coupling as well as magnetic noise afflicting B. We can estimate the magnitude of this noise combination from Eqn. 6.2 using the fact that $J = \overline{E}_z$ at this detuning. Under this condition $\delta E = 2\delta\Delta_{\text{rms}}$,

where we define $\delta\Delta_{\text{rms}}$ to include the noise sources pertinent to t_c, g_a, and B, leading to

$$\delta\Delta_{\text{rms}} \approx \frac{\sqrt{2}\hbar}{2}(T_2^* = 600 \text{ ns})^{-1} = 0.8 \text{ neV}.$$

For large operation detunings, the energy separation between the $S-T_-$ states reaches a parallel regime (Fig. 6.3b), which diminishes the charge noise contribution to δE. In this regime, ΔE_{ST_-} approximately equals $\overline{E}_z$, where the combined electrical and magnetic "Zeeman" noise affecting $\overline{g}$ and B limits T_2^*. We estimate this parameter using Eqn. 6.2 again:

$$\delta E \approx \delta\overline{E}_{z,\text{rms}},$$
$$\delta\overline{E}_{z,\text{rms}} \approx \sqrt{2}\hbar(T_2^* = 317 \text{ ns})^{-1} = 3 \text{ neV}.$$

6.3.2 T_1 relaxation time

The system's T_1 spin relaxation time was measured by varying the wait time at the readout position ϵ_r (Fig. 6.5b). For these measurements, the system was allowed to completely dephase at the operation detuning ϵ_P before being pulsed back to the readout window for a variable amount of time (see inset of Fig. 6.5b). We fit the resulting exponential decaying curve shown in Fig. 6.5b to $P = Ae^{-(t/T_1)} + B$ and find T_1 to be 17.2 ± 3.2 μs, which is comparable to experiments done in single hole [HFS20] and $S - T_0$ qubits [JHB21]. However, this T_1 can still be improved, as single hole spin relaxation times as long as 32 ms with $B = 0.67$ T have been measured using tighter dot confinements and limiting the dot-reservoir coupling [LHR20].

6.4 Gate modulation of the singlet-triplet frequency

We now focus on modulating the coherent evolution of the $S-T_-$ states by adjusting the voltage applied to the barrier separating the two quantum dots. Over a small range of voltage (12 mV), Fig. 6.6 illustrates the dramatic transformation the $S-T_-$ oscillations

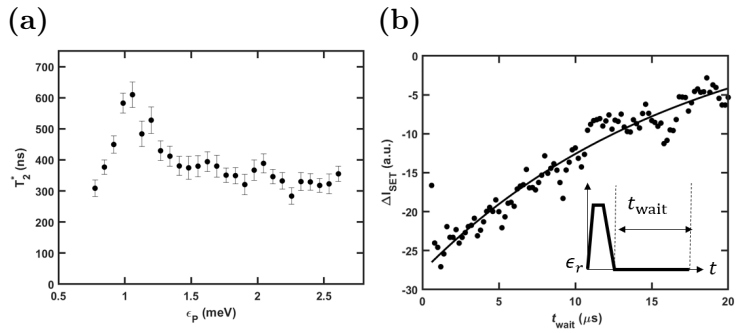

Figure 6.5: Dephasing and relaxation measurements **(a)** T_2^* as a function of detuning. Linecuts in Fig. 6.3a are fit to the curve $P = Ae^{-(t/T_2^*)^2}\cos(\omega t + B) + Ce^{-t/D} + E$, where the dephasing time T_2^* is extracted and plotted in (a). Error bars equal one standard deviation of the uncertainty in T_2^* from this fit. This decoherence can be understood as a contribution from two noise terms with the simple model shown in Eqn. 6.2. From this model, we estimate $\delta\Delta_{\text{rms}} = 0.8$ and $\delta\overline{E}_{z,\text{rms}} = 3$ neV. **(b)** A T_1 measurement where the change in SET current is recorded as a function of wait time at the measurement point M. We extract T_1 from the fit $P = Ae^{(-t/T_1)} + B$ (solid line) and calculate $T_1 = 17.2 \pm 3.2$ μs. Inset: the pulse used to observe this decay.

undergo. As V_B increases, it is clear the frequency of evolution between the two states decreases monotonically. From the Fourier transform of these oscillations, we can isolate two quantities of interest, namely $\overline{g}$ from the frequency at large detuning following $f \sim \overline{E}_z/h$ and Δ_{ST_-} from the minimum frequency near $\epsilon_P = 1$ meV, where $f = 2\Delta_{ST_-}/h$.

We would like to note that the location of the frequency minimum ϵ_* is determined by the tunnel coupling t_c and $\overline{E}_z$ from the condition $J = \overline{E}_z$ [JMH22]:

$$\epsilon_* = \frac{2t_c^2 - \overline{E}_z^2}{\overline{E}_z}, \tag{6.3}$$

Because ϵ_* remains approximately constant throughout this range of V_B, a decrease in t_c must be accompanied by a decrease in $\overline{E}_z$. While it is evident from the sharper rises seen in the FFTs of Fig. 6.6 that t_c decreases with V_B, a similar decline in $\overline{E}_z$, and therefore $\overline{g}$, is necessarily present. From the $S - T_-$ evolution frequency at large ϵ_P in Fig. 6.6, we

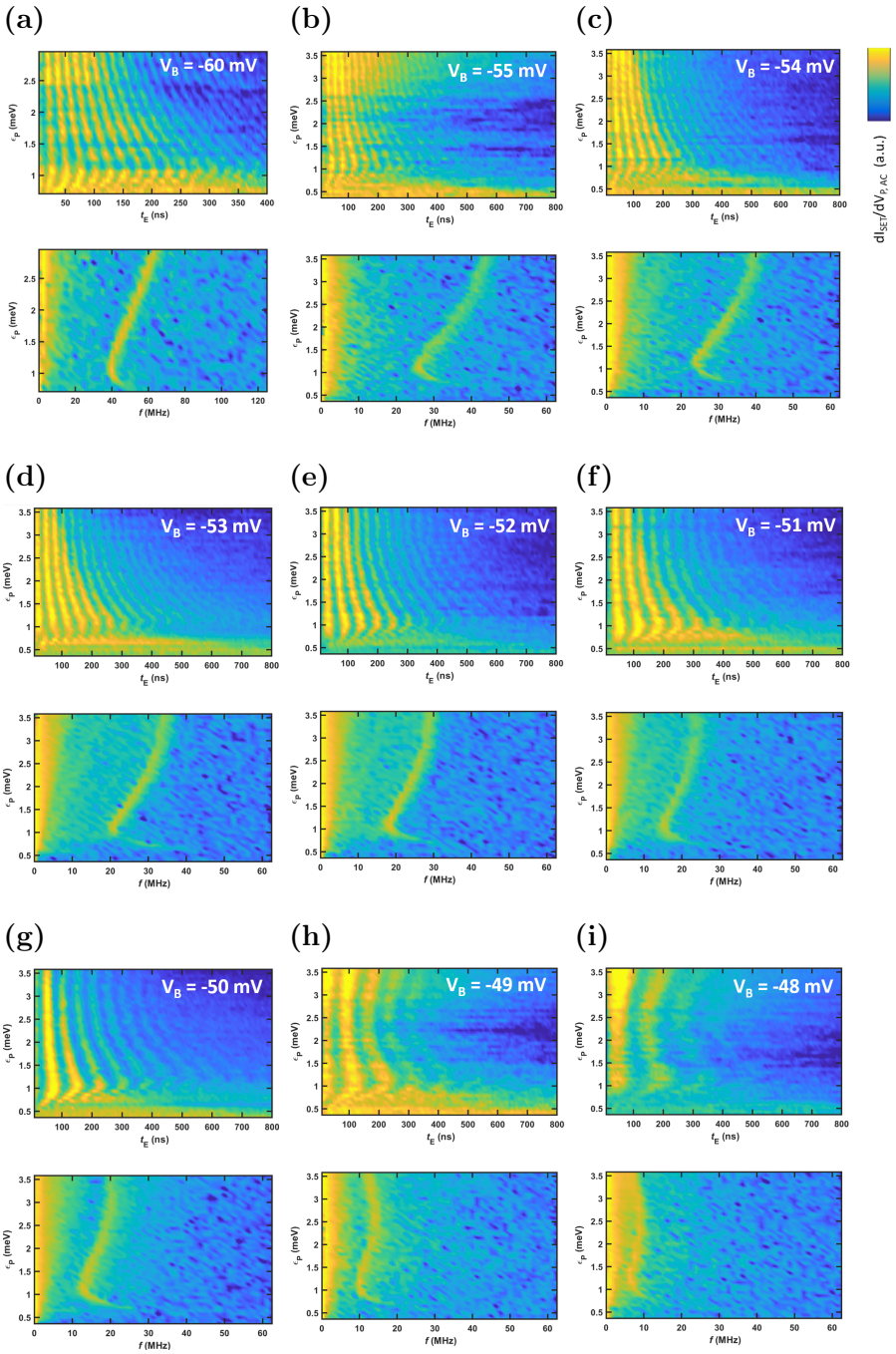

Figure 6.6: (a)-(i) Evolution of the $S - T_-$ oscillations (upper) and their corresponding FFTs (lower) as a function of the middle barrier gate voltage V_B. Applying a more positive barrier gate voltage decreases the frequency of the oscillations throughout the entire detuning range. Both the minimum and maximum frequencies decrease as V_B becomes more positive, indicating a reduction in both Δ_{ST_-} and $\overline{g}$.

can then extract the dependence of $\overline{g}$ on V_B.

Fig. 6.7 demonstrates the linear trend both Δ_{ST_-} and $\overline{g}$ follow with respect to the barrier voltage V_B. Recall the $S - T_-$ coupling is determined by both the spin-orbit coupling and the effect of the anisotropic g-tensors, g_a. We assert it is the latter of these contributions that is affected over the small range of V_B considered here. Consequently, to justify the modulation of the qubit frequency in Fig. 6.7, we seek a mechanism that simultaneously reduces both $\overline{g}$ and g_a as V_B increases. We will argue these changes are accomplished through increasing the admixture of light-hole (LH) states into the predominantly heavy-hole (HH) ground state of the Ge quantum dot.

While it is well known the upper valence bands in Ge/SiGe heterostructures are composed primarily of HH states due to a large HH-LH splitting Δ_{HL} [SKZ21], an accurate understanding of the g-tensor in many Ge materials requires the consideration of the LH bands [DMS14, WKV16, AGK13]. To understand the consequences of this mixing, it is beneficial to first examine the g-factor components of both bands in the case of bulk Ge. As described in Refs. [KKY01, NDZ03, WKV16] and Section 3.6.2, for the pure HH state, the out-of-plane g-factor is $g_\perp = 6\kappa + \frac{27q}{2}$ and the in-plane component is $g_\parallel = 3q$, where $\kappa = 3.41$ and $q = 0.07$ are the magnetic Luttinger parameters. Note this κ and q result in the large anisotropy of the g-tensor: $g_\perp \gg g_\parallel$. Conversely, for pure LH states, $g_\perp = 2\kappa$ and $g_\parallel = 4\kappa$. By comparing these two bands, the LH state has a smaller $g_\perp$ but greater $g_\parallel$ compared to the HH state. Therefore, when increasing the LH admixture in the ground state of the quantum dot, we expect a decrease in $g_\perp$ and an increase in $g_\parallel$, which has been experimentally observed for various mixing mechanisms [NDZ03, AGK13, WKV16, JMH22].

Due to the large anisotropy between $g_\perp$ and $g_\parallel$, $\overline{g}$ is dominated by its out-of-plane component $\overline{g}_\perp$. With an increase in HH-LH mixing, we then expect a decrease in $\overline{g}$ through a reduction in $g_\perp$ for either dot. On the other hand, the in-plane g-factors are the leading order terms defining g_a, where a more similar $g_\parallel$ between the two dots diminishes g_a. Increasing the HH-LH mixing decreases g_a when the in-plane g-factors change in such a way that the difference between $g_\parallel$ for the left and right dot lessens.

Importantly, this mixing mechanism can then explain both downward trends we observe in Fig. 6.7.

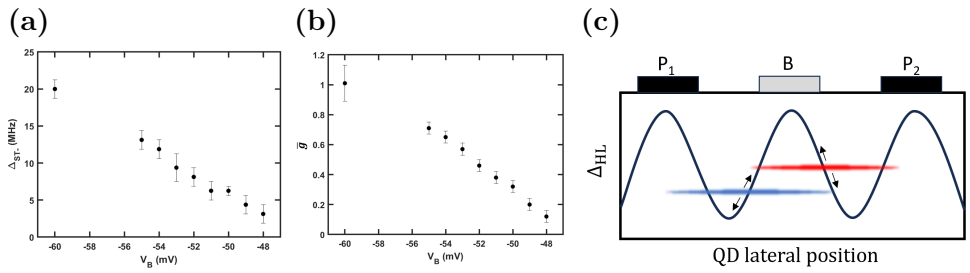

Figure 6.7: **(a)** $\Delta_{ST\_}$ as a function of barrier voltage. Values are extracted from the minimum frequency of the FFTs shown in Fig. 6.6. **(b)** $\overline{g}$ is extracted from frequency at large detunings in Fig. 6.6 and plotted versus the barrier voltage. Both parameters show a strong linear dependence on the barrier gate voltage. This behavior can be explained by the dots moving through a non-uniform strain environment, which directly impacts the g-factors of each dot. Error bars for (a) and (b) are calculated from the linewidth of the Fourier transform data. **(c)** Cartoon depicting the Δ_{HL} profile underneath the confinement gates due to the effects of strain.

Although a complete theoretical description lies outside the scope of this thesis, we will now discuss how a non-uniform strain profile is a viable candidate for this rise in HH-LH mixing as V_B is varied. As discussed in Section 3.5, strain originates from the differences in thermal contraction between the gate electrodes defining the quantum dots and the substrate. This strain can both alter Δ_{HL} and directly mix the HH and LH states, where these effects are greatest along the edges of the confinement gates [NST04, LMM21, CRZ23]. In one case, Corley-Wiciak et al., 2023 measured the strain profile of a gate-defined quantum dot device and simulated that Δ_{HL} can vary as much as 4% [CRZ23]. Although this percentage seems small at first glance, the degree of mixing between the HH and LH states scales as $\left(\frac{1}{\Delta_{HL}}\right)^2$ [LBZ15], where even admixtures of 1% significantly reduce $g_\perp$ [WKV16].

From a rough calculation of the quantum dot positions as a function of V_B (see section 6.6.4) and using the results of Ref. [CRZ23] for a qualitative picture, we estimate

an overall shift of the right dot's position away from the middle barrier leads to a $\sim 3\%$ decrease in Δ_{HL} as the dot moves into a region of increased strain (see Fig. 6.7c). With this change leading to a 9% enhancement in the LH admixture, we can expect a decrease in both $\bar{g}$ and Δ_{ST_-}. We want to stress these values are crude calculations and only serve as a guide to how the hole g-tensor evolves with respect to V_B and explain the trends in Fig. 6.7.

6.5 Conclusion

In summary, we have explored the coherent oscillations in a Ge hole double dot between the singlet, $|S\rangle$, and polarized triplet state, $|T_-\rangle$. The dephasing time of this manipulation strongly depends on the operation detuning with a maximum of $T_2^* = 600$ ns, while the spin relaxation time at the readout point was measured to be $T_1 = 17.2\ \mu$s. The maximum in T_2^* coincides with the minimum in the $S - T_-$ energy splitting, where the system is insensitive to the noise disturbing J and $\overline{E}_z$. Furthermore, we observe the frequency of evolution between these spin states can be modulated through the voltage of the middle barrier separating the two dots. The frequency dependence on V_B points to the changing dot position over a variable strain profile as the reason for adjusting the qubit frequency. These results suggest strain can be exploited to fine-tune qubit frequencies in Ge. Furthermore, if a variable frequency profile is not desired, the sensitivity of the g-tensor to the quantum dot position can be mitigated by reducing strain in the system, such as by defining gate electrodes with palladium instead of gold to closer match the thermal response of Ge [ML22].

6.6 Supplementary Material

6.6.1 Simulating singlet-triplet oscillations

With the estimates of $\delta\Delta_{\text{rms}} = 0.8$ and $\delta\overline{E}_{z,\text{rms}} = 3$ neV, we can simulate the coherent oscillations of Fig. 6.6c while including dephasing. Similar to section 5.6.3, we use the

Lindblad equation (5.6) with the Python program QuTiP to measure the probability of the singlet state after the application of a simple square pulse. Although the square pulse does not follow the path of the Ramsey pulse used in experiment, it still samples the energy difference between the two lowest states, meaning it can still recreate much of what is observed in this experiment.

The Hamiltonian used is Eqn. 6.1, where we estimate the parameters from the data in Fig. 6.7: $t_c = 9.9$ μeV, $g_a = 0.19$, and $\bar{g} = 0.65$. I have ignored the contribution of the spin-orbit coupling when estimating g_a; however, it is not vital for recreating the frequency spectrum in Fig. 6.6c. With the exclusion of Δ_{so}, this value of g_a is overestimated and $\bar{g}$ is slightly underestimated.

Inhomogeneous dephasing was included using Eqn. 6.2 and the estimated parameters $\delta\Delta_{\text{rms}}$ and $\delta\overline{E}_{z,\text{rms}}$. Because dephasing originates from the fluctuations in energy difference between $|S\rangle$ and $|T_-\rangle$, the appropriate dephasing operator takes the form of the Pauli matrix σ_z. However, it is important to recognize that σ_z is only the correct dephasing operator when the eigenstates at the operation detuning ϵ_P are $|S\rangle$ and $|T_-\rangle$. More generally, the dephasing operator needs to be a rotation along the axis of the eigenstates $B = \{|g\rangle, |e\rangle\}$. Therefore, for each ϵ_P, σ_z is transformed into the basis defined by the eigenstates: $\sigma_{\text{dephase}} = B^{-1}\sigma_z B$.

The results are the simulation are shown in Fig. 6.8, where there is good qualitative agreement between the simulated (6.8a) and experimental (6.8c) data. While the singlet-triplet frequency is recreated, the simulation's accuracy can still be improved by including the spin-orbit coupling back into the Hamiltonian. This change is discussed more in Chapter 7.

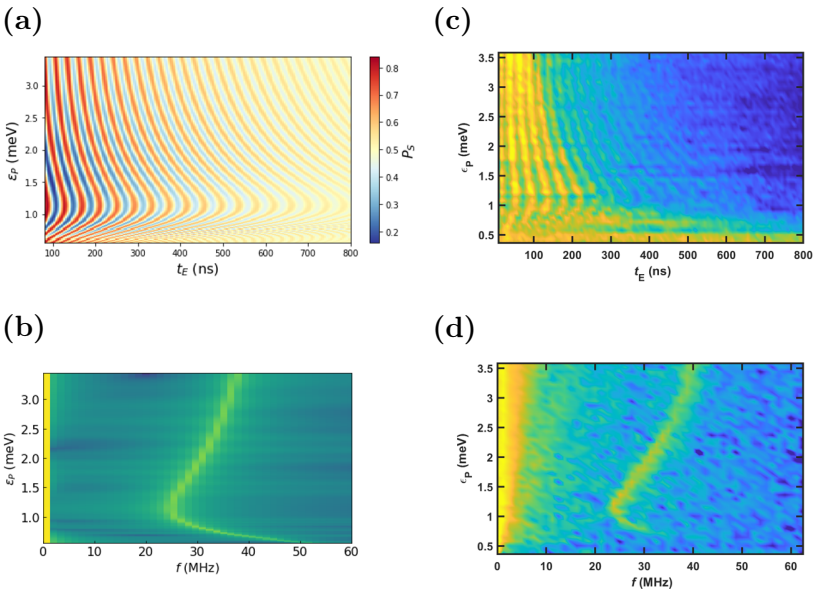

Figure 6.8: **(a)** Simulation of the Hamiltonian in Eqn. 6.1 with dephasing included. **(b)** FFT of the simulation in (a). **(c)** and **(d)** Experimental data from Fig. 6.6c reproduced here for convenience.

6.6.2 Lever arm measurement

When a small bias voltage V_{SD} is applied across the reservoirs of the double quantum dot, conductance regions in the shape of triangles will form at the intersections of charge transitions between the two dots [WFE02]. The dimensions of these triangles are directly related to the energy separation between the source and drain, eV_{SD}, and the chemical potential of each dot being controlled by its respective plunger voltage:

$$\alpha \Delta V_g = |eV_{SD}|,$$

where α is the lever arm relating the plunger voltage to the dot chemical potential. By measuring the lengths of these triangles along each plunger voltage axis (Fig. 6.9), we determined the conversion factor α from the ratio of plunger voltage to energy: $\alpha = eV_{SD}/\Delta V_P$. We find the lever arms for P_1 and P_2 to be $\alpha_1 = 0.12$ and $\alpha_2 = 0.11$ eV/V, which were used to convert the plunger voltages to energies for all calculations in this work.

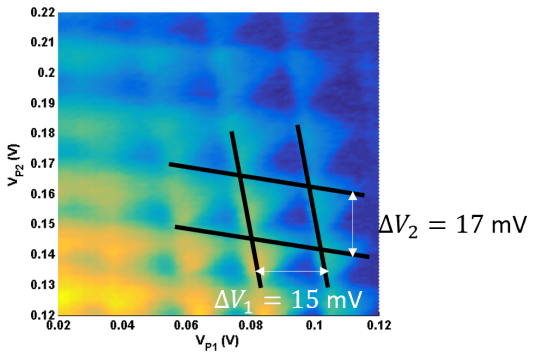

Figure 6.9: Stability diagram illustrating transport through both quantum dots with a bias voltage $V_{SD} = 1$ mV across the source-drain reservoirs. Triangles can be seen where the dot charging lines intersect. The dimensions of these triangles are directly related to the source-drain bias and plunger voltage, which we used to calculate the lever arm of each plunger: $\alpha_1 = 0.12$ and $\alpha_2 = 0.11$ eV/V.

6.6.3 Fast $S - T_-$ oscillations

The fastest oscillations we observed are shown in Fig. 6.10. This scan was taken at a center barrier voltage of $V_B = -180$ mV, and illustrates Δ_{ST_-} reaching 75 MHz and the maximum $S-T_-$ energy splitting surpassing 180 MHz, which corresponds to a maximum $\overline{g} \approx 2.8$. While this $\overline{g}$ is larger than those reported in the main text, we do not expect $\overline{g}$ to grow indefinitely as we decrease the middle barrier voltage. As V_B draws the two dots closer to the middle barrier's edge, the continuous increase in tunnel coupling t_c between the two dots will eventually make system inoperable as a singlet-triplet qubit.

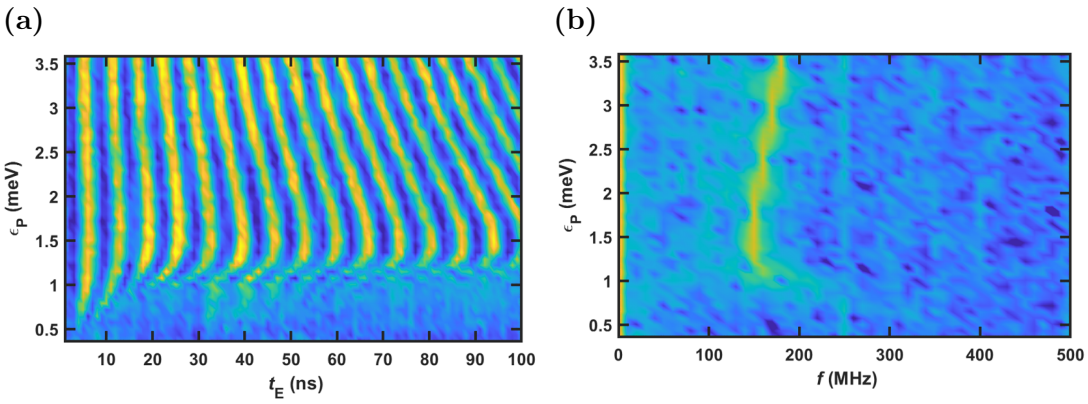

Figure 6.10: **(a)** A scan of the singlet-triplet evolution illustrating the highest frequency oscillations seen from our data set. **(b)** The the FFT of (a). The $S - T_-$ anticrossing gap is $\Delta_{ST_-} = 75$ MHz, while the frequency at large detunings reaches 180 MHz, signifying $\overline{g} = 2.8$.

6.6.4 Estimation of Δ_{HL} from dot positions

We were able to make a crude estimate of the quantum dot positions using capacitance ratios of the quantum dot to the two plungers and barrier gates. The capacitance ratios were found from the slope of the charging lines in the stability diagram. From the relative strength of the effect two gates have on a dot and knowing the gate positions in the x-y plane, we can create what is known as an Apollonian circle. Creating Apollonian circles for two different pairs of gates allowed us to estimate the dot position where these two circles intersect. Repeating this process for various V_B generated the data in Fig. 6.11.

From Fig. 6.11, the left dot moves back and forth around its starting position, whereas the right dot generally moves towards the upper right in the x-y plane. From the right dot's relative shift of ~ 36 nm, we estimated the change to Δ_{HL}. Using the simulated data in Ref. [CRZ23], we note a maximum change of $\sim 4\%$ in the HH-LH splitting. Compared to the device in this study, the quantum well in Ref. [CRZ23] is situated closer to the confinement gates, which greatly increases the effects of strain. Consequently, we only wish to use this 4% change in Δ_{HL} as a guide for understanding the pattern of our data. We expect the modification to Δ_{HL} to be minimized directly underneath an electrode and greatest between two electrodes, which is a distance of 50 nm in our device. Naively assuming a linear dependence of the strain on the dot's position underneath the gates, we can estimate the change in Δ_{HL} from the 36 nm shift in the right dot:

$$\delta\Delta_{HL} \sim \frac{4\%}{50\text{nm}} 36\text{nm} = 3\%.$$

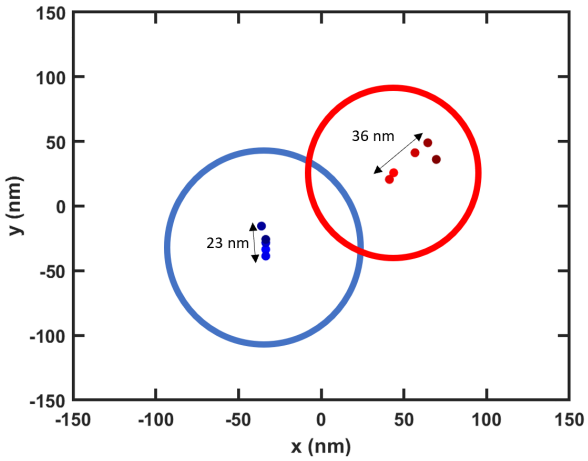

Figure 6.11: The positions of both quantum dots are estimated from their capacitance ratios to the two plungers and center barrier. The coordinate $x = 0$ is where the center barrier is placed. Blue (red) dots correspond to the left (right) dot positions. The darker shades correspond to more positive V_B. It is evident that as V_B increases, the right dot tends to shift away from the center barrier, while the left dot fluctuates around its starting position. The diameters of the two quantum dots are depicted as circles and estimated in section 6.2.2.

CHAPTER 7

Future Directions

7.1 Coupled valley qubits in silicon

A natural step to progress the valley qubit physics described in Chapter 5 is to couple two valley qubits together. While this thesis has focused on single qubit operations, one must combine single qubit gates with two-qubit operations to create a universal set of gates that can perform a generic quantum computation [DiV00]. Coupling any two qubits together requires an interaction between them that is ideally independent of the physics governing the single qubit operations. This would allow one to switch the two-qubit coupling on and off at will.

One possible implementation of two coupled valley qubits has been theoretically discussed in [FMG19], where the charge character of the valley qubit can be coupled to a neighboring qubit. This interaction is a simple capacitive coupling between the two qubits, where the energy dispersion for one qubit shifts depending on the charge state of the partner qubit. For example, consider a valley qubit performing X rotations at detuning ϵ_x. This detuning will shift when the charge state of a neighboring qubit changes, for example, an electron in the partner qubit tunnels from the left to the right dot. By controlling the detuning of the control qubit, one then controls whether the target qubit undergoes X rotations.

Another potential avenue for coupled valley qubits is through exploiting their interaction with the spin states of the quantum dot [YCF20]. This interaction lies outside

the scope of this thesis, but it has been shown that it is possible to couple the spin and valley states of a quantum dot through their mutual interaction with the orbital state of the quantum dot [LON21, CCE23]. This spin-orbit-valley coupling then allows neighboring qubits to interact via the spin exchange interaction J, which has been widely used for two-qubit operations of pure spin qubits [MGG22, NTN22, XRS22, HFS20, HLR21, HYC19, WPK18].

7.2 Magnetic field spectroscopy of the singlet-triplet states in germanium

While using the permanent magnet in the experiments of Chapter 6 was an inexpensive and simple solution to lift the degeneracy of the triplet states, it prevents the investigation of several important magnetic properties of the qubit. One such characteristic is the distinction between the spin-orbit coupling t_{so} and g-factor anisotropy g_a that play the important role of coupling the singlet $|S\rangle$ and polarized triplet $|T_-\rangle$ states. Looking at the coupling between these two states, $\Delta = |t_{so} \sin(\Omega/2) + g_a \mu_B B \cos(\Omega/2)|$, both contributions are affected by the detuning ϵ through Ω. Consequently, one cannot isolate t_{so} from g_a using only electrical control, as it will always be possible to distribute weight between these two factors and arrive at the same predicted experimental outcome.

One solution to this issue is the ability to vary the magnetic field, as only the effective Zeeman term is affected by B. At large detuning, $\sin(\Omega/2) \to 0$, leaving the Zeeman terms in the Hamiltonian to control the singlet-triplet oscillations. If one can vary the angle of B at this detuning, the resulting change in qubit frequency can be fit to determine all Zeeman components [JMH22], including g_a. Knowing g_a, one can solve for t_{so} from the value of Δ_{ST_-} at the $S - T_-$ anticrossing.

Moreover, varying the magnetic field comes with the additional bonus of being able to probe the coupling between the singlet $|S\rangle$ and polarized triplet $|T_-\rangle$ in a reliable manner. varying the magnetic field and quickly pulsing to an operation detuning ϵ results in resonance between the singlet and polarized triplet states when the spin exchange energy

equals the Zeeman splitting: $J(\epsilon) = \pm\bar{g}\mu_B B$ [PJT05, LON21, JHB21, JMH22, CCE23]. The pattern this resonance traces out is a funnel, and observing it reinforces the claim that the coherent oscillations seen in Chapter 6 are indeed between the $|S\rangle$ and $|T_-\rangle$.

7.3 Two-axis control and characterization of the $S - T_-$ qubit

Having observed $S-T_-$ oscillations in Chapter 6, future endeavors should include demonstrating full two-axis control and fidelity calculations similar to that of Chapter 5. A straightforward method to implement the two rotation axes is by utilizing two points in detuning that Chapter 6 already discussed: the $S - T_-$ anticrossing and the large detuning regime. At the anticrossing, the two eigenstates are mixtures of $|S\rangle$ and $|T_-\rangle$, meaning Larmor precession will occur around the x axis. Furthermore, this anticrossing is an ideal location for qubit operation due to its higher resistance to noise. This was exemplified in Fig. 6.5a, where this detuning had the longest T_2^* time.

For the second axis of control, one can operate the qubit at large detunings for Z rotations. As mentioned in Chapter 6, the rotation axis for large ϵ depends on the ratio between the $S-T_-$ coupling at large ϵ and the average Zeeman energy $\bar{E}_z$. While a tilted axis can be supplemented with additional X rotations, an ideal Z rotation is possible if one can vary the magnetic field orientation [MB21b]. Additionally, the energy levels between the singlet and triplet state are nearly parallel in this regime, providing the qubit some protection from charge noise for these operations.

By pulsing the qubit's detuning between the anticrossing and large detunings, one can selectively perform X or Z rotations on demand. However, even with this ability, it is not obvious that a qubit encoded in this $S - T_-$ subspace performs any better than other successful encodings. To help answer this question, one can rely on the fidelity measurements calculated in Section 5.7.3. Furthermore, fidelity calculations can shed light onto which aspects the qubit can be improved further. For example, they can help distinguish whether initialization and measurement errors or decoherence during the operation are the main sources of infidelity.

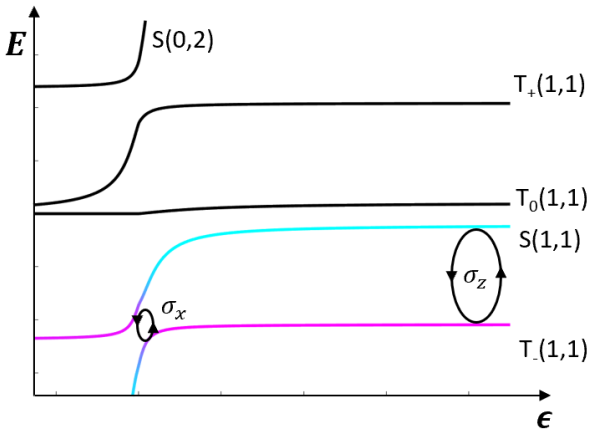

Figure 7.1: Singlet triplet energy levels as a function of detuning. For the $S - T_-$ qubit, X rotations are performed at the $S - T_-$ anticrossing, while Z rotations can be performed at large detunings

7.4 Conclusion

We have demonstrated devices that are capable of hosting single qubits on both silicon and germanium heterostructures. While fidelities of the valley qubit in Si are only $\sim 90\%$, there are many aspects that can still be optimized that were not fully explored this thesis. These include fixing rotation errors, improving state initialization, and enhancing readout fidelity. With the advent of multiple groups showcasing spin-valley mechanics, the possibility to utilize the valley degree of freedom with existing spin qubit methodology is open.

Our work on a Ge hole spin qubit has reinforced the rapid development hole spin qubits have made over the past few years. We have shown that the g-tensors of the quantum dots can be easily tuned through the modulating the electrostatic potentials. As any spin qubit is reliant on the dot g-tensor when determining operation frequencies, this tuning becomes an important knob that can increase operation speeds or move the qubit frequency into an ideal range. However, one must keep in mind that this adaptability comes with the downside of being more susceptible to noise. Moreover, it is exciting that holes qubits no longer must grapple with a variable valley splitting across a

wafer, possibly opening a pathway to the larger qubit arrays in semiconductor quantum dots.

Appendix A

Fabrication Recipe

Here I detail the fabrication recipe used for the double quantum dot devices made on the Ge/SiGe heterostructure. This recipe is almost identical to that of making a device on the Si/SiGe wafer; the pertinent difference lies in how the Ohmic regions are made, as described in Section 4.1.4.

1. **Cleave wafer:** Dice wafer into appropriately sized pieces to work with.
    - Spin on two layers of AZ 5214E photoresist to form a protective layer.
        - Spin at 600 rpm for 6 s, then 3500 rpm for 30 s.
        - Bake for 1 min at 95 C.
        - Spin at 600 rpm for 6 s, then 3500 rpm for 30 s.
        - Bake for 2 min at 95 C.
    - Cleave wafer by scribing desired break points and using a glass slide as a fulcrum.
2. **Clean wafer:** Ensure wafer surface is as clean as possible before moving to the photolithography step.
    - Quick clean: Spray wafer with the following solvents in order to remove the bulk of resist: acetone, isopropanol (IPA), and DI water. Dry the wafer with N_2.

- Long clean:
  - 5 min in acetone
  - While in acetone, use sonicator for 1 min
  - 5 min in IPA
  - 5 min in DI water
  - Dry with N_2
  - 4 min in an O_2 plasma asher
- Inspect wafer under microscope and repeat the long clean until the surface is pristine.

3. **Photolithography (Ohmic contacts and alignment markers):**
   - Apply HMDS. Let wafer sit inside an HMDS tank for 10 min. If an HMDS tank is not available, apply 3 drops of HMDS onto wafer and spin for 6 s at 600 rpm and 50 s at 4500 rpm.
   - Spin AZ 5214E resist for 6 s at 600 rpm and 50 s at 4500 rpm.
   - Bake at 95 C for 90 s.
   - Expose for 9 s using a mask designed for Ohmic contact implant regions.
   - Develop in 1:3 AZ 400K:DI water for 45 s with slight agitation, then 30 s in DI water.
   - Place wafer into an O_2 plasma asher for 30 s to etch away any remaining resist that was not developed.
4. **Buffered Oxide Etch (BOE):** Remove thin, top SiO_2 layer of the wafer.
   - Dip the wafer in BOE for 10 s.
   - Place in DI water for 30 s.
   - Place in a second DI water beaker for 30 s.

- Place in a third DI water beaker while the BOE is properly disposed. Then dry off with N_2.

5. **Metallization (Ohmic contacts and alignment markers):** Using a CHA e-beam evaporator, deposit 60 nm of Platinum (Pt) at 0.5 A/s.

6. **Liftoff:** Remove resist from the wafer.

   - 30 min in one acetone beaker. Use a pipette to blow acetone on the wafer until the majority of resist has lifted off.
   - Transfer the wafer to a clean acetone beaker and place the beaker in the sonicator for 30 s.
   - If any visible unwanted metal remains, use a combination of the pipette and sonicator to remove it.
   - Quickly clean the wafer with IPA and transfer it to a Petri dish filled with IPA. Note that the wafer cannot be allowed to dry during this process, or any unwanted metal will permanently adhere to the wafer.
   - Inspect the wafer under a microscope to ensure the liftoff process has removed all unwanted pieces of metal. If not, transfer the wafer back into the clean acetone beaker and use the sonicator and pipette to remove residual metal.
   - Clean the wafer with DI water and dry off with N_2.

7. **Anneal Pt contacts:** Forming gas anneal for 1 hour at 420 C.

8. **Electron-beam lithography (EBL):**

   - Clean wafer.
   - Spin 1 layer of PMMA A4 for 6 s at 600 rpm then 50 s at 4500 rpm.
   - Bake for 90 s at 180 C.
   - Spin 1 layer of PMMA A2 for 6 s at 600 rpm then 50 s at 4500 rpm.
   - Bake for 90 s at 180 C.

- Write small, inner device leads with a 200 pA current and dosage of 1270 μC/cm^2.
- Write large, outer device feature with a 50 nA current and dosage of 900 μC/cm^2.
- Develop in premixed 1:3 MIBK:IPA for 45 s.
- Place in an IPA stop bath beaker for 45 s.
- Clean wafer with DI water, then dry off with N_2.

9. **Metallization (device leads):** Using a CHA e-beam evaporator, deposit 5 nm of Titanium (Ti) at 0.5 A/s and 45 nm of Gold (Au) at 0.7 A/s.

10. **Liftoff:** This step is almost identical to the previous liftoff with two important differences:
    - Let the wafer sit in the clean acetone beaker overnight.
    - Avoid using the sonicator when possible, as it will destroy the inner device leads. If absolutely needed, dip the acetone beaker into the sonicator for 1-2 s.

11. **Optional: image inner device leads with an SEM**

12. **Savannah Atomic Layer Deposition (ALD):**
    - Clean wafer.
    - Setting the chamber temperatures to 200 C, grow 100 nm of Al_2O_3.

13. **Photolithography (top gate):**
    - Clean wafer.
    - Apply 1 layer of HMDS through either an HMDS tank or spinner (see previous photolithography step).
    - Spin 1 layer of AZ 5214E for 6 s at 600 rpm then 50 s at 4500 rpm.

- Bake for 1 min at 95 C.
- Expose using a top gate mask pattern for 9 s.
- Develop in 1:3 AZ 400K:DI water for 45 s.
- Place in a DI water stop bath for 30 s.
- Rinse with DI water, then dry off with N_2.

14. **Metallization (top gate):** Using a CHA e-beam evaporator, deposit 100 nm of Al at 1 A/s.

15. **Liftoff:** This step is almost identical to the Ohmic contacts and alignment markers liftoff step.

    - Use the sonicator for 1-2 s if necessary, but try to avoid it.

16. **Etch contact windows:**

    - Repeat the photolithography (top gate) step using a mask for contact windows.
    - Dip the wafer for 3 s into a beaker of Transetch-N (Phosphoric acid) heated to 180 C.
    - Quickly dip the wafer into a beaker of DI water and use a pipette for 30 s to remove Transetch-N from the wafer's surface.
    - Place the wafer into a second beaker of DI water and repeat the previous step.
    - Rinse the wafer off with DI water and dry with N_2.
    - Inspect the wafer under a microscope to determine if the Al_2O_3 was etched through completely in exposed contact windows. If not, dip the wafer into Transetch-N again and follow subsequent steps.
    - Clean wafer to remove resist.

17. **Cleave wafer into individual devices:**

    - Spin 1 layer of AZ 5214E photoresist for 6 s at 600 rpm and 30 s at 3500 rpm.

- Bake at 95 C for 1 min.
- Spin 1 layer of AZ 5214E photoresist for 6 s at 600 rpm and 30 s at 3500 rpm.
- Bake at 95 C for 2 min.
- Use a diamond scribe or the LPKF ProtoLaser to cleave off devices. If using the ProtoLaser, set the laser width to 60 μm and repetitions to 25.

References

[AGK13] N. Ares, V. N. Golovach, G. Katsaros, M. Stoffel, F. Fournel, L. I. Glazman, O. G. Schmidt, and S. De Franceschi. "Nature of tunable hole g factors in quantum dots." *Physical Review Letters*, **110**, 1 2013.

[AM76] Neil W. Ashcroft and N. David Mermin. *Solid state physics*. Holt, Rinehart and Winston, New York, 1976.

[Ben80] Paul Benioff. "The computer as a physical system: A microscopic quantum mechanical hamiltonian model of computers as represented by Turing machines." *Journal of Statistical Physics*, **22**(5):563–591, 1980.

[Bha14] Ramesh Bhandari. "On Single Qubit Quantum State Tomography." July 2014. arXiv:1407.6668 [quant-ph].

[BKE03] Timothy B. Boykin, Gerhard Klimeck, M. A. Eriksson, Mark Friesen, S. N. Coppersmith, Paul von Allmen, Fabiano Oyafuso, and Seungwon Lee. "Valley splitting in strained silicon quantum wells." *Applied Physics Letters*, **84**(1):115–117, 12 2003.

[BLN21] Guido Burkard, Thaddeus D. Ladd, John M. Nichol, Andrew Pan, and Jason R. Petta. "Semiconductor Spin Qubits." 12 2021.

[BLP23] Guido Burkard, Thaddeus D. Ladd, Andrew Pan, John M. Nichol, and Jason R. Petta. "Semiconductor spin qubits." *Rev. Mod. Phys.*, **95**:025003, Jun 2023.

[BP74] Gennadii Levikovich Bir and Grigorii Ezekielevich Pikus. *Symmetry and strain-induced effects in semiconductors*. Wiley, New York, 1974.

[BT] Graham Batey and Gustav Teleberg. "Principles of dilution refrigeration.".

[CCE23] Xinxin Cai, Elliot J. Connors, Lisa F. Edge, and John M. Nichol. "Coherent spin–valley oscillations in silicon." *Nature Physics*, **19**(3):386–393, March 2023.

[CD10] Andrew M. Childs and Wim van Dam. "Quantum algorithms for algebraic problems." *Rev. Mod. Phys.*, **82**:1–52, Jan 2010.

[CGT09] J. M. Chow, J. M. Gambetta, L. Tornberg, Jens Koch, Lev S. Bishop, A. A. Houck, B. R. Johnson, L. Frunzio, S. M. Girvin, and R. J. Schoelkopf. "Randomized Benchmarking and Process Tomography for Gate Errors in a Solid-State Qubit." *Phys. Rev. Lett.*, **102**:090502, Mar 2009.

[CHD10] Dimitrie Culcer, Xuedong Hu, and S. Das Sarma. "Interface roughness, valley-orbit coupling, and valley manipulation in quantum dots." *Phys. Rev. B*, **82**:205315, Nov 2010.

[Chu95] Shun Lien Chuang. *Physics of optoelectronic devices.* Wiley series in pure and applied optics. Wiley, New York, 1995.

[CLY16] Gang Cao, Hai-Ou Li, Guo-Dong Yu, Bao-Chuan Wang, Bao-Bao Chen, Xiang-Xiang Song, Ming Xiao, Guang-Can Guo, Hong-Wen Jiang, Xuedong Hu, and Guo-Ping Guo. "Tunable Hybrid Qubit in a GaAs Double Quantum Dot." *Phys. Rev. Lett.*, **116**:086801, Feb 2016.

[CN22] Hugh Collins and Chris Nay. "IBM unveils 400 qubit-plus quantum processor and next-generation IBM Quantum System Two.", Nov 2022.

[CNQ19] Elliot J. Connors, J. J. Nelson, Haifeng Qiao, Lisa F. Edge, and John M. Nichol. "Low-frequency charge noise in Si/SiGe quantum dots." *Physical Review B*, **100**, 10 2019.

[CRZ23] Cedric Corley-Wiciak, Carsten Richter, Marvin H. Zoellner, Ignatii Zaitsev, Costanza L. Manganelli, Edoardo Zatterin, Tobias U. Schülli, Agnieszka A. Corley-Wiciak, Jens Katzer, Felix Reichmann, Wolfgang M. Klesse, Nico W. Hendrickx, Amir Sammak, Menno Veldhorst, Giordano Scappucci, Michele Virgilio, and Giovanni Capellini. "Nanoscale Mapping of the 3D Strain Tensor in a Germanium Quantum Well Hosting a Functional Spin Qubit Device." *ACS Applied Materials & Interfaces*, **15**(2):3119–3130, 2023. PMID: 36598897.

[CSK12] Dimitrie Culcer, A. L. Saraiva, Belita Koiller, Xuedong Hu, and S. Das Sarma. "Valley-Based Noise-Resistant Quantum Computation Using Si Quantum Dots." *Phys. Rev. Lett.*, **108**:126804, Mar 2012.

[Dav98] J. H. Davies. *The physics of low-dimensional semiconductors: an introduction.* Cambridge University Press, Cambridge, U.K.; New York, NY, USA, 1998.

[DEP64] J. P. Dismukes, L. Ekstrom, and R. J. Paff. "Lattice Parameter and Density in Germanium-Silicon Alloys1." *The Journal of Physical Chemistry*, **68**(10):3021–3027, 1964.

[DiV95] David P. DiVincenzo. "Quantum Computation." *Science*, **270**(5234):255–261, 1995.

[DiV00] David P. DiVincenzo. "The physical implementation of quantum computation." *Fortschritte der Physik*, **48**:771–783, 2000.

[DMS14] I. L. Drichko, V. A. Malysh, I. Yu Smirnov, L. E. Golub, S. A. Tarasenko, A. V. Suslov, O. A. Mironov, M. Kummer, and H. Von Känel. "In-plane magnetic field effect on hole cyclotron mass and gz factor in high-mobility SiGe/Ge/SiGe structures." *Physical Review B - Condensed Matter and Materials Physics*, **90**, 9 2014.

[DN09] J. Danon and Yu. V. Nazarov. "Pauli spin blockade in the presence of strong spin-orbit coupling." *Phys. Rev. B*, **80**:041301, Jul 2009.

[EJ96] Artur Ekert and Richard Jozsa. "Quantum computation and Shor's factoring algorithm." *Rev. Mod. Phys.*, **68**:733–753, Jul 1996.

[FC10] Mark Friesen and S. N. Coppersmith. "Theory of valley-orbit coupling in a Si/SiGe quantum dot." *Phys. Rev. B*, **81**:115324, Mar 2010.

[FCH18] M. A. Fogarty, K. W. Chan, B. Hensen, W. Huang, T. Tanttu, C. H. Yang, A. Laucht, M. Veldhorst, F. E. Hudson, K. M. Itoh, D. Culcer, T. D. Ladd, A. Morello, and A. S. Dzurak. "Integrated silicon qubit platform with single-spin addressability, exchange control and single-shot singlet-triplet readout." *Nature Communications*, **9**(1):4370, October 2018.

[FCT07] Mark Friesen, Sucismita Chutia, Charles Tahan, and S. N. Coppersmith. "Valley splitting theory of SiGe/Si/SiGe quantum wells." *Phys. Rev. B*, **75**:115318, Mar 2007.

[FEC06] Mark Friesen, M. A. Eriksson, and S. N. Coppersmith. "Magnetic field dependence of valley splitting in realistic Si\SiGe quantum wells." *Applied Physics Letters*, **89**(20):202106, 11 2006.

[Fey82] Richard P. Feynman. "Simulating physics with computers." *International Journal of Theoretical Physics*, **21**(6–7):467–488, 1982.

[FL96] M. V. Fischetti and S. E. Laux. "Band structure, deformation potentials, and carrier mobility in strained Si, Ge, and SiGe alloys." *Journal of Applied Physics*, **80**(4):2234–2252, 08 1996.

[FMG19] Adam Frees, Sebastian Mehl, John King Gamble, Mark Friesen, and S. N. Coppersmith. "Adiabatic two-qubit gates in capacitively coupled quantum dot hybrid qubits." *npj Quantum Information*, **5**, 12 2019.

[Fre17] Blake Freeman. *Charge Noise and Dephasing in Silicon-Based Lateral Quantum Dots*. PhD thesis, UCLA, 2017.

[FSG09] Austin G. Fowler, Ashley M. Stephens, and Peter Groszkowski. "High-threshold universal quantum computation on the surface code." *Physical Review A*, **80**(5):052312, November 2009.

[FSJ16] Blake M. Freeman, Joshua S. Schoenfield, and Hongwen Jiang. "Comparison of low frequency charge noise in identically patterned Si/SiO2 and Si/SiGe quantum dots." *Applied Physics Letters*, **108**, 6 2016.

[GA20] Tenghua Gao and Kazuya Ando. "Chapter 1 - Spin–orbit torques." volume 29 of *Handbook of Magnetic Materials*, pp. 1–55. Elsevier, 2020.

[GEC13] John King Gamble, M. A. Eriksson, S. N. Coppersmith, and Mark Friesen. "Disorder-induced valley-orbit hybrid states in Si quantum dots." *Phys. Rev. B*, **88**:035310, Jul 2013.

[GHW05] J. Gorman, D. G. Hasko, and D. A. Williams. "Charge-Qubit Operation of an Isolated Double Quantum Dot." *Phys. Rev. Lett.*, **95**:090502, Aug 2005.

[Gre90] Martin A. Green. "Intrinsic concentration, effective densities of states, and effective mass in silicon." *Journal of Applied Physics*, **67**(6):2944–2954, 03 1990.

[GSF07] Srijit Goswami, K. A. Slinker, Mark Friesen, L. M. McGuire, J. L. Truitt, Charles Tahan, L. J. Klein, J. O. Chu, P. M. Mooney, D. W. Van Der Weide, Robert Joynt, S. N. Coppersmith, and Mark A. Eriksson. "Controllable valley splitting in silicon quantum devices." *Nature Physics*, **3**:41–45, 1 2007.

[HDK08] A R Hamilton, R Danneau, O Klochan, W R Clarke, A P Micolich, L H Ho, M Y Simmons, D A Ritchie, M Pepper, K Muraki, and Y Hirayama. "The 0.7 anomaly in one-dimensional hole quantum wires." *Journal of Physics: Condensed Matter*, **20**(16):164205, apr 2008.

[HFC03] T. Hayashi, T. Fujisawa, H. D. Cheong, Y. H. Jeong, and Y. Hirayama. "Coherent Manipulation of Electronic States in a Double Quantum Dot." *Phys. Rev. Lett.*, **91**:226804, Nov 2003.

[HFS18] N. W. Hendrickx, D. P. Franke, A. Sammak, M. Kouwenhoven, D. Sabbagh, L. Yeoh, R. Li, M. L. V. Tagliaferri, M. Virgilio, G. Capellini, G. Scappucci, and M. Veldhorst. "Gate-controlled quantum dots and superconductivity in planar germanium." *Nature Communications*, **9**(1):2835, July 2018.

[HFS20] N. W. Hendrickx, D. P. Franke, A. Sammak, G. Scappucci, and M. Veldhorst. "Fast two-qubit logic with holes in germanium." *Nature*, **577**:487–491, 1 2020.

[HKP07] R. Hanson, L. P. Kouwenhoven, J. R. Petta, S. Tarucha, and L. M.K. Vandersypen. "Spins in few-electron quantum dots." *Reviews of Modern Physics*, **79**:1217–1265, 10 2007.

[HLL12] S.-H. Huang, T.-M. Lu, S.-C. Lu, C.-H. Lee, C. W. Liu, and D. C. Tsui. "Mobility enhancement of strained Si by optimized SiGe/Si/SiGe structures." *Applied Physics Letters*, **101**(4):042111, 07 2012.

[HLR21] Nico W. Hendrickx, William I.L. Lawrie, Maximilian Russ, Floor van Riggelen, Sander L. de Snoo, Raymond N. Schouten, Amir Sammak, Giordano Scappucci, and Menno Veldhorst. "A four-qubit germanium quantum processor." *Nature*, **591**:580–585, 3 2021.

[HMM23] N. W. Hendrickx, L. Massai, M. Mergenthaler, F. Schupp, S. Paredes, S. W. Bedell, G. Salis, and A. Fuhrer. "Sweet-spot operation of a germanium hole spin qubit with highly anisotropic noise sensitivity." 5 2023.

[HYC19] W. Huang, C. H. Yang, K. W. Chan, T. Tanttu, B. Hensen, R. C.C. Leon, M. A. Fogarty, J. C.C. Hwang, F. E. Hudson, K. M. Itoh, A. Morello, A. Laucht, and A. S. Dzurak. "Fidelity benchmarks for two-qubit gates in silicon." *Nature*, **569**:532–536, 5 2019.

[Ihn10] Thomas Ihn. *Semiconductor nanostructures: quantum states and electronic transport.* Oxford University Press, Oxford, 2010.

[Int18] SRI International. "A brief introduction to quantum computing 2018.", Nov 2018.

[JHB21] Daniel Jirovec, Andrea Hofmann, Andrea Ballabio, Philipp M. Mutter, Giulio Tavani, Marc Botifoll, Alessandro Crippa, Josip Kukucka, Oliver Sagi, Frederico Martins, Jaime Saez-Mollejo, Ivan Prieto, Maksim Borovkov, Jordi Arbiol, Daniel Chrastina, Giovanni Isella, and Georgios Katsaros. "A singlet-triplet hole spin qubit in planar Ge." *Nature Materials*, **20**:1106–1112, 8 2021.

[JJH18] Ryan M. Jock, N. Tobias Jacobson, Patrick Harvey-Collard, Andrew M. Mounce, Vanita Srinivasa, Dan R. Ward, John Anderson, Ron Manginell, Joel R. Wendt, Martin Rudolph, Tammy Pluym, John King Gamble, Andrew D. Baczewski, Wayne M. Witzel, and Malcolm S. Carroll. "A silicon metal-oxide-semiconductor electron spin-orbit qubit." *Nature Communications*, **9**, 12 2018.

[JMH22] Daniel Jirovec, Philipp M. Mutter, Andrea Hofmann, Alessandro Crippa, Marek Rychetsky, David L. Craig, Josip Kukucka, Frederico Martins, Andrea Ballabio, Natalia Ares, Daniel Chrastina, Giovanni Isella, Guido Burkard, and Georgios Katsaros. "Dynamics of Hole Singlet-Triplet Qubits with Large g -Factor Differences." *Physical Review Letters*, **128**, 3 2022.

[JN06] Oleg N. Jouravlev and Yuli V. Nazarov. "Electron Transport in a Double Quantum Dot Governed by a Nuclear Magnetic Field." *Phys. Rev. Lett.*, **96**:176804, May 2006.

[Jor] Stephen Jordan.

[JSP20] A. T. Jones, C. P. Scheller, J. R. Prance, Y. B. Kalyoncu, D. M. Zumbühl, and R. P. Haley. "Progress in Cooling Nanoelectronic Devices to Ultra-Low Temperatures." *Journal of Low Temperature Physics*, **201**(5):772–802, 2020.

[Kan56] E.O. Kane. "Energy band structure in p-type germanium and silicon." *Journal of Physics and Chemistry of Solids*, **1**(1):82–99, 1956.

[KGF12] Teck Seng Koh, John King Gamble, Mark Friesen, M. A. Eriksson, and S. N. Coppersmith. "Pulse-Gated Quantum-Dot Hybrid Qubit." *Phys. Rev. Lett.*, **109**:250503, Dec 2012.

[Kit05] Charles Kittel. *Introduction to solid state physics*. Wiley, Hoboken, NJ, 8th ed edition, 2005.

[KKY01] A. A. Kiselev, K. W. Kim, and E. Yablonovitch. "In-plane light-hole (formula presented) factor in strained cubic heterostructures." *Physical Review B - Condensed Matter and Materials Physics*, **64**, 2001.

[KSS14] Dohun Kim, Zhan Shi, C. B. Simmons, D. R. Ward, J. R. Prance, Teck Seng Koh, John King Gamble, D. E. Savage, M. G. Lagally, Mark Friesen, S. N. Coppersmith, and Mark A. Eriksson. "Quantum control and process tomography of a semiconductor quantum dot hybrid qubit." *Nature*, **511**:70–74, 2014.

[KSW14] E. Kawakami, P. Scarlino, D. R. Ward, F. R. Braakman, D. E. Savage, M. G. Lagally, Mark Friesen, S. N. Coppersmith, M. A. Eriksson, and L. M.K. Vandersypen. "Electrical control of a long-lived spin qubit in a Si/SiGe quantum dot." *Nature Nanotechnology*, **9**:666–670, 2014.

[KWS15] Dohun Kim, Daniel R. Ward, Christie B. Simmons, Don E. Savage, Max G. Lagally, Mark Friesen, Susan N. Coppersmith, and Mark A. Eriksson. "High-fidelity resonant gating of a silicon-based quantum dot hybrid qubit." *npj Quantum Information*, **1**, 2015.

[Lak]

[LBZ15] Jun Wei Luo, Gabriel Bester, and Alex Zunger. "Supercoupling between heavy-hole and light-hole states in nanostructures." *Physical Review B - Condensed Matter and Materials Physics*, **92**, 10 2015.

[LD98] Daniel Loss and David P. DiVincenzo. "Quantum computation with quantum dots." *Phys. Rev. A*, **57**:120–126, Jan 1998.

[LHL21] Mario Lodari, Nico W Hendrickx, William I L Lawrie, Tzu-Kan Hsiao, Lieven M K Vandersypen, Amir Sammak, Menno Veldhorst, and Giordano Scappucci. "Low percolation density and charge noise with holes in germanium." *Materials for Quantum Technology*, **1**(1):011002, jan 2021.

[LHR13] Jiun-Yun Li, Chiao-Ti Huang, Leonid P. Rokhinson, and James C. Sturm. "Extremely high electron mobility in isotopically-enriched 28Si two-dimensional electron gases grown by chemical vapor deposition." *Applied Physics Letters*, **103**(16):162105, 10 2013.

[LHR20] W. I. L. Lawrie, N. W. Hendrickx, F. van Riggelen, M. Russ, L. Petit, A. Sammak, G. Scappucci, and M. Veldhorst. "Spin Relaxation Benchmarks and Individual Qubit Addressability for Holes in Quantum Dots." *Nano Letters*, **20**(10):7237–7242, 2020. PMID: 32833455.

[LMM21] S. D. Liles, F. Martins, D. S. Miserev, A. A. Kiselev, I. D. Thorvaldson, M. J. Rendell, I. K. Jin, F. E. Hudson, M. Veldhorst, K. M. Itoh, O. P. Sushkov, T. D. Ladd, A. S. Dzurak, and A. R. Hamilton. "Electrical control of the g tensor of the first hole in a silicon MOS quantum dot." *Physical Review B*, **104**, 12 2021.

[LON21] Y.-Y. Liu, L.A. Orona, Samuel F. Neyens, E.R. MacQuarrie, M.A. Eriksson, and A. Yacoby. "Magnetic-Gradient-Free Two-Axis Control of a Valley Spin Qubit in Si_xGe_{1-x}." *Phys. Rev. Appl.*, **16**:024029, Aug 2021.

[MB21a] Philipp M. Mutter and Guido Burkard. "All-electrical control of hole singlet-triplet spin qubits at low-leakage points." *Physical Review B*, **104**, 11 2021.

[MB21b] Philipp M. Mutter and Guido Burkard. "Natural heavy-hole flopping mode qubit in germanium." *Phys. Rev. Res.*, **3**:013194, Feb 2021.

[MBH12] B. M. Maune, M. G. Borselli, B. Huang, T. D. Ladd, P. W. Deelman, K. S. Holabird, A. A. Kiselev, I. Alvarado-Rodriguez, R. S. Ross, A. E. Schmitz, M. Sokolich, C. A. Watson, M. F. Gyure, and A. T. Hunter. "Coherent singlet-triplet oscillations in a silicon-based double quantum dot." *Nature*, **481**:344–347, 1 2012.

[MGG22] Adam R Mills, Charles R Guinn, Michael J Gullans, Anthony J Sigillito, Mayer M Feldman, Erik Nielsen, and Jason R Petta. "Two-qubit silicon quantum processor with operation fidelity exceeding 99

[MHP15] X. Mi, T. M. Hazard, C. Payette, K. Wang, D. M. Zajac, J. V. Cady, and J. R. Petta. "Magnetotransport studies of mobility limiting mechanisms in undoped Si/SiGe heterostructures." *Phys. Rev. B*, **92**:035304, Jul 2015.

[MKP18] X. Mi, S. Kohler, and J. R. Petta. "Landau-Zener interferometry of valley-orbit states in Si/SiGe double quantum dots." *Phys. Rev. B*, **98**:161404, Oct 2018.

[ML22] Brian Chi Ho Mooy and Nai Shyan Lai. "Strain Effects in a Double Dot Quantum Dot System." In *2022 International Conference on Edge Computing and Applications (ICECAA)*, pp. 1635–1640, 2022.

[Mon16] Ashley Montanaro. "Quantum Algorithms: An overview." *npj Quantum Information*, **2**(1), 2016.

[MPB17] X. Mi, Csaba G. Péterfalvi, Guido Burkard, and J. R. Petta. "High-Resolution Valley Spectroscopy of Si Quantum Dots." *Phys. Rev. Lett.*, **119**:176803, Oct 2017.

[MRL08] M. Mohseni, A. T. Rezakhani, and D. A. Lidar. "Quantum-process tomography: Resource analysis of different strategies." *Phys. Rev. A*, **77**:032322, Mar 2008.

[MS17] D. S. Miserev and O. P. Sushkov. "Dimensional reduction of the Luttinger Hamiltonian and g-factors of holes in symmetric two-dimensional semiconductor heterostructures." *Phys. Rev. B*, **95**:085431, Feb 2017.

[MSB13] Filipp Mueller, Raymond N. Schouten, Matthias Brauns, Tian Gang, Wee Han Lim, Nai Shyan Lai, Andrew S. Dzurak, Wilfred G. van der Wiel, and Floris A. Zwanenburg. "Printed circuit board metal powder filters for low electron temperatures." *Review of Scientific Instruments*, **84**(4):044706, 04 2013.

[MSH14] Rai Moriya, Kentarou Sawano, Yusuke Hoshi, Satoru Masubuchi, Yasuhiro Shiraki, Andreas Wild, Christian Neumann, Gerhard Abstreiter, Dominique Bougeard, Takaaki Koga, and Tomoki Machida. "Cubic Rashba Spin-Orbit Interaction of a Two-Dimensional Hole Gas in a Strained-Ge/SiGe Quantum Well." *Phys. Rev. Lett.*, **113**:086601, Aug 2014.

[NC10] Michael A. Nielsen and Isaac L. Chuang. *Quantum Computation and Quantum Information: 10th Anniversary Edition*. Cambridge University Press, 2010.

[NDZ03] A. V. Nenashev, A. V. Dvurechenskii, and A. F. Zinovieva. "Wave functions and g factor of holes in Ge/Si quantum dots." *Physical Review B - Condensed Matter and Materials Physics*, **67**, 5 2003.

[NKK12] H. Nakamura, T. Koga, and T. Kimura. "Experimental Evidence of Cubic Rashba Effect in an Inversion-Symmetric Oxide." *Phys. Rev. Lett.*, **108**:206601, May 2012.

[NSM] NSM. "Band structure and carrier concentration of Germanium (Ge).".

[NST04] T. Nakaoka, T. Saito, J. Tatebayashi, and Y. Arakawa. "Size, shape, and strain dependence of the g factor in self-assembled In(Ga)As quantum dots." *Phys. Rev. B*, **70**:235337, Dec 2004.

[NTN22] Akito Noiri, Kenta Takeda, Takashi Nakajima, Takashi Kobayashi, Amir Sammak, Giordano Scappucci, and Seigo Tarucha. "Fast universal quantum gate above the fault-tolerance threshold in silicon." *Nature*, **601**:338–342, 1 2022.

[OPG04] J. L. O'Brien, G. J. Pryde, A. Gilchrist, D. F. V. James, N. K. Langford, T. C. Ralph, and A. G. White. "Quantum Process Tomography of a Controlled-NOT Gate." *Phys. Rev. Lett.*, **93**:080502, Aug 2004.

[PAJ03] Nicholas Peters, Joseph Altepeter, Evan Jeffrey, David Branning, and Paul Kwiat. "Precise Creation, Characterization, and Manipulation of Single Optical Qubits." *Quantum Info. Comput.*, **3**(7):503–517, oct 2003.

[Pen20] Nicholas Penthorn. *Investigating Valley States and their Interactions in Silicon/Silicon-Germanium Quantum Dots*. PhD thesis, UCLA, 2020.

[Per10] Asher Peres. *Quantum theory: concepts and methods*. Fundamental theories of physics. Kluwer Acad. Publ, Dordrecht, nachdr. edition, 2010.

[PJT05] J. R. Petta, A. C. Johnson, J. M. Taylor, E. A. Laird, A. Yacoby, M. D. Lukin, C. M. Marcus, M. P. Hanson, and A. C. Gossard. "Coherent Manipulation of Coupled Electron Spins in Semiconductor Quantum Dots." *Science*, **309**(5744):2180–2184, 2005.

[PLG10] J. R. Petta, H. Lu, and A. C. Gossard. "A Coherent Beam Splitter for Electronic Spin States." *Science*, **327**(5966):669–672, 2010.

[PLK22] Brian Paquelet Wuetz, Merritt P. Losert, Sebastian Koelling, Lucas E. A. Stehouwer, Anne-Marije J. Zwerver, Stephan G. J. Philips, Mateusz T. Madzik, Xiao Xue, Guoji Zheng, Mario Lodari, Sergey V. Amitonov, Nodar Samkharadze, Amir Sammak, Lieven M. K. Vandersypen, Rajib Rahman, Susan N. Coppersmith, Oussama Moutanabbir, Mark Friesen, and Giordano Scappucci. "Atomic fluctuations lifting the energy degeneracy in Si/SiGe quantum dots." *Nature Communications*, **13**(1):7730, December 2022.

[Pre18] John Preskill. "Quantum Computing in the NISQ era and beyond." *Quantum*, **2**:79, August 2018.

[PSR19] Nicholas E. Penthorn, Joshua S. Schoenfield, John D. Rooney, Lisa F. Edge, and Hong Wen Jiang. "Two-axis quantum control of a fast valley qubit in silicon." *npj Quantum Information*, **5**, 12 2019.

[QCA20] Google AI Quantum, Collaborators*†, Frank Arute, Kunal Arya, Ryan Babbush, Dave Bacon, Joseph C. Bardin, Rami Barends, Sergio Boixo, Michael Broughton, Bob B. Buckley, David A. Buell, Brian Burkett, Nicholas Bushnell, Yu Chen, Zijun Chen, Benjamin Chiaro, Roberto Collins, William Courtney, Sean Demura, Andrew Dunsworth, Edward Farhi, Austin Fowler, Brooks Foxen, Craig Gidney, Marissa Giustina, Rob Graff, Steve Habegger, Matthew P. Harrigan, Alan Ho, Sabrina Hong, Trent Huang, William J. Huggins, Lev Ioffe, Sergei V. Isakov, Evan Jeffrey, Zhang Jiang, Cody Jones, Dvir Kafri, Kostyantyn Kechedzhi, Julian Kelly, Seon Kim, Paul V. Klimov, Alexander Korotkov, Fedor Kostritsa, David Landhuis, Pavel Laptev, Mike Lindmark, Erik Lucero, Orion Martin, John M. Martinis, Jarrod R. McClean, Matt McEwen, Anthony Megrant, Xiao Mi, Masoud Mohseni, Wojciech Mruczkiewicz, Josh Mutus, Ofer Naaman, Matthew Neeley, Charles Neill, Hartmut Neven, Murphy Yuezhen Niu, Thomas E. O'Brien, Eric Ostby, Andre Petukhov, Harald Putterman, Chris Quintana, Pedram Roushan, Nicholas C. Rubin, Daniel Sank, Kevin J. Satzinger, Vadim Smelyanskiy, Doug Strain, Kevin J. Sung, Marco Szalay, Tyler Y. Takeshita, Amit Vainsencher, Theodore White, Nathan Wiebe, Z. Jamie Yao, Ping Yeh, and

Adam Zalcman. "Hartree-Fock on a superconducting qubit quantum computer." *Science*, **369**(6507):1084–1089, 2020.

[RLS23] John Rooney, Zhentao Luo, Lucas E. A. Stehouwer, Giordano Scappucci, Menno Veldhorst, and Hong-Wen Jiang. "Gate modulation of the hole singlet-triplet qubit frequency in germanium." (arXiv:2311.10188), November 2023. arXiv:2311.10188 null.

[Sch97] Friedrich Schäffler. "High-mobility Si and Ge structures." *Semiconductor Science and Technology*, **12**(12):1515, dec 1997.

[SCH09] A. L. Saraiva, M. J. Calderón, Xuedong Hu, S. Das Sarma, and Belita Koiller. "Physical mechanisms of interface-mediated intervalley coupling in Si." *Phys. Rev. B*, **80**:081305, Aug 2009.

[Sch17] Joshua Steven Schoenfield. *Coherent Control and Spectroscopy of Valley States of Individual Electrons in Silicon Quantum Dots*. PhD thesis, UCLA, 2017.

[SCJ07] Shiue-yuan Shiau, Sucismita Chutia, and Robert Joynt. "Valley Kondo effect in silicon quantum dots." *Phys. Rev. B*, **75**:195345, May 2007.

[SFJ17] Joshua S. Schoenfield, Blake M. Freeman, and Hong Wen Jiang. "Coherent manipulation of valley states at multiple charge configurations of a silicon quantum dot device." *Nature Communications*, **8**, 12 2017.

[Sho96] P.W. Shor. "Fault-tolerant quantum computation." In *Proceedings of 37th Conference on Foundations of Computer Science*, pp. 56–65, Oct 1996.

[Sho97] Peter W. Shor. "Polynomial-Time Algorithms for Prime Factorization and Discrete Logarithms on a Quantum Computer." *SIAM Journal on Computing*, **26**(5):1484–1509, 1997.

[SKZ21] Giordano Scappucci, Christoph Kloeffel, Floris A. Zwanenburg, Daniel Loss, Maksym Myronov, Jian Jun Zhang, Silvano De Franceschi, Georgios Katsaros, and Menno Veldhorst. "The germanium quantum information route.", 10 2021.

[SSH19] Amir Sammak, Diego Sabbagh, Nico W. Hendrickx, Mario Lodari, Brian Paquelet Wuetz, Alberto Tosato, LaReine Yeoh, Monica Bollani, Michele Virgilio, Markus Andreas Schubert, Peter Zaumseil, Giovanni Capellini, Menno Veldhorst, and Giordano Scappucci. "Shallow and Undoped Germanium Quantum Wells: A Playground for Spin and Hybrid Quantum Technology." *Advanced Functional Materials*, **29**(14):1807613, 2019.

[SSW14] Zhan Shi, C. B. Simmons, Daniel R. Ward, J. R. Prance, Xian Wu, Teck Seng Koh, John King Gamble, D. E. Savage, M. G. Lagally, Mark Friesen, S. N.

Coppersmith, and M. A. Eriksson. "Fast coherent manipulation of three-electron states in a double quantum dot." *Nature Communications*, **5**, 1 2014.

[TH19] Bilal Tariq and Xuedong Hu. "Effects of interface steps on the valley-orbit coupling in a Si/SiGe quantum dot." *Phys. Rev. B*, **100**:125309, Sep 2019.

[TMW21] L. A. Terrazos, E. Marcellina, Zhanning Wang, S. N. Coppersmith, Mark Friesen, A. R. Hamilton, Xuedong Hu, Belita Koiller, A. L. Saraiva, Dimitrie Culcer, and Rodrigo B. Capaz. "Theory of hole-spin qubits in strained germanium quantum dots." *Phys. Rev. B*, **103**:125201, Mar 2021.

[TNW02] R. T. Thew, K. Nemoto, A. G. White, and W. J. Munro. "Qudit quantum-state tomography." *Phys. Rev. A*, **66**:012303, Jul 2002.

[TTM12] Alexei M. Tyryshkin, Shinichi Tojo, John J. L. Morton, Helge Riemann, Nikolai V. Abrosimov, Peter Becker, Hans-Joachim Pohl, Thomas Schenkel, Michael L. W. Thewalt, Kohei M. Itoh, and S. A. Lyon. "Electron spin coherence exceeding seconds in high-purity silicon." *Nature Materials*, **11**(2):143–147, February 2012.

[TZ15] Ted Thorbeck and Neil M. Zimmerman. "Formation of strain-induced quantum dots in gated semiconductor nanostructures." *AIP Advances*, **5**(8):087107, 08 2015.

[VHY14] M. Veldhorst, J. C.C. Hwang, C. H. Yang, A. W. Leenstra, B. De Ronde, J. P. Dehollain, J. T. Muhonen, F. E. Hudson, K. M. Itoh, A. Morello, and A. S. Dzurak. "An addressable quantum dot qubit with fault-tolerant control-fidelity." *Nature Nanotechnology*, **9**:981–985, 1 2014.

[VRY15] M. Veldhorst, R. Ruskov, C. H. Yang, J. C. C. Hwang, F. E. Hudson, M. E. Flatté, C. Tahan, K. M. Itoh, A. Morello, and A. S. Dzurak. "Spin-orbit coupling and operation of multivalley spin qubits." *Phys. Rev. B*, **92**:201401, Nov 2015.

[WCP08] R Winkler, Dimitrie Culcer, S J Papadakis, B Habib, and M Shayegan. "Spin orientation of holes in quantum wells." *Semiconductor Science and Technology*, **23**(11):114017, oct 2008.

[WDT23] Chien-An Wang, Corentin Déprez, Hanifa Tidjani, William I. L. Lawrie, Nico W. Hendrickx, Amir Sammak, Giordano Scappucci, and Menno Veldhorst. "Probing resonating valence bonds on a programmable germanium quantum simulator." *npj Quantum Information*, **9**(1):1–8, June 2023.

[WEC15] Clement H. Wong, M. A. Eriksson, S. N. Coppersmith, and Mark Friesen. "High-fidelity singlet-triplet $S{-}T_{-}$ qubits in inhomogeneous magnetic fields." *Phys. Rev. B*, **92**:045403, Jul 2015.

[WFE] W G Van Der Wiel, S De Franceschi, J M Elzerman, T Fujisawa, S Tarucha, and L P Kouwenhoven. "Electron transport through double quantum dots.".

[WFE02] W G Van Der Wiel, S De Franceschi, J M Elzerman, T Fujisawa, S Tarucha, and L P Kouwenhoven. "Electron transport through double quantum dots." *Rev. Mod. Phys.*, **75**:1–22, Dec 2002.

[Win03] Roland Winkler. *Spin-orbit coupling effects in two-dimensional electron and hole systems*. Springer tracts in modern physics. Springer, Berlin; New York, 2003.

[WKV16] Hannes Watzinger, Christoph Kloeffel, Lada Vukušić, Marta D. Rossell, Violetta Sessi, Josip Kukučka, Raimund Kirchschlager, Elisabeth Lausecker, Alisha Truhlar, Martin Glaser, Armando Rastelli, Andreas Fuhrer, Daniel Loss, and Georgios Katsaros. "Heavy-Hole States in Germanium Hut Wires." *Nano Letters*, **16**:6879–6885, 11 2016.

[WPK18] T. F. Watson, S. G.J. Philips, E. Kawakami, D. R. Ward, P. Scarlino, M. Veldhorst, D. E. Savage, M. G. Lagally, Mark Friesen, S. N. Coppersmith, M. A. Eriksson, and L. M.K. Vandersypen. "A programmable two-qubit quantum processor in silicon." *Nature*, **555**:633–637, 3 2018.

[WRJ23] Aaron J. Weinstein, Matthew D. Reed, Aaron M. Jones, Reed W. Andrews, David Barnes, Jacob Z. Blumoff, Larken E. Euliss, Kevin Eng, Bryan H. Fong, Sieu D. Ha, Daniel R. Hulbert, Clayton A.C. Jackson, Michael Jura, Tyler E. Keating, Joseph Kerckhoff, Andrey A. Kiselev, Justine Matten, Golam Sabbir, Aaron Smith, Jeffrey Wright, Matthew T. Rakher, Thaddeus D. Ladd, and Matthew G. Borselli. "Universal logic with encoded spin qubits in silicon." *Nature*, **615**:817–822, 3 2023.

[WSV22a] Chien-An Wang, Giordano Scappucci, Menno Veldhorst, and Maximilian Russ. "Modelling of planar germanium hole qubits in electric and magnetic fields." 8 2022.

[WSV22b] Chien-An Wang, Giordano Scappucci, Menno Veldhorst, and Maximilian Russ. "Modelling of planar germanium hole qubits in electric and magnetic fields." ", 8 2022.

[WWP14] Xian Wu, D. R. Ward, J. R. Prance, Dohun Kim, John King Gamble, R. T. Mohr, Zhan Shi, D. E. Savage, M. G. Lagally, Mark Friesen, S. N. Coppersmith, and M. A. Eriksson. "Two-axis control of a singlet–triplet qubit with an integrated micromagnet." *PNAS*, **111**:11938–11942, 8 2014.

[XRS22] Xiao Xue, Maximilian Russ, Nodar Samkharadze, Brennan Undseth, Amir Sammak, Giordano Scappucci, and Lieven M.K. Vandersypen. "Quantum logic with spin qubits crossing the surface code threshold." *Nature*, **601**:343–347, 1 2022.

[YCF20] Yuan Chi Yang, S. N. Coppersmith, and Mark Friesen. "High-fidelity entangling gates for quantum-dot hybrid qubits based on exchange interactions." *Physical Review A*, **101**, 1 2020.

[YRR13] C. H. Yang, A. Rossi, R. Ruskov, N. S. Lai, F. A. Mohiyaddin, S. Lee, C. Tahan, G. Klimeck, A. Morello, and A. S. Dzurak. "Spin-valley lifetimes in a silicon quantum dot with tunable valley splitting." *Nature Communications*, **4**, 6 2013.

[ZDM12] Floris A. Zwanenburg, Andrew S. Dzurak, Andrea Morello, Michelle Y. Simmons, Lloyd C. L. Hollenberg, Gerhard Klimeck, Sven Rogge, Susan N. Coppersmith, and Mark A. Eriksson. "Silicon Quantum Electronics." 6 2012.

[ZDR18] Junkai Zeng, Xiu-Hao Deng, Antonio Russo, and Edwin Barnes. "General solution to inhomogeneous dephasing and smooth pulse dynamical decoupling." *New Journal of Physics*, **20**(3):033011, mar 2018.

[ZHC17] Neil M. Zimmerman, Peihao Huang, and Dimitrie Culcer. "Valley Phase and Voltage Control of Coherent Manipulation in Si Quantum Dots." *Nano Letters*, **17**(7):4461–4465, 2017. PMID: 28657758.

[ZKW22] A. M.J. Zwerver, T. Krähenmann, T. F. Watson, L. Lampert, H. C. George, R. Pillarisetty, S. A. Bojarski, P. Amin, S. V. Amitonov, J. M. Boter, R. Caudillo, D. Corras-Serrano, J. P. Dehollain, G. Droulers, E. M. Henry, R. Kotlyar, M. Lodari, F. Lüthi, D. J. Michalak, B. K. Mueller, S. Neyens, J. Roberts, N. Samkharadze, G. Zheng, O. K. Zietz, G. Scappucci, M. Veldhorst, L. M.K. Vandersypen, and J. S. Clarke. "Qubits made by advanced semiconductor manufacturing." *Nature Electronics*, **5**:184–190, 3 2022.

[ZLS13] Lijun Zhang, Jun Wei Luo, Andre Saraiva, Belita Koiller, and Alex Zunger. "Genetic design of enhanced valley splitting towards a spin qubit in silicon." *Nature Communications*, **4**, 2013.